In-flight Air Supply System for PEM Fuel Cells

Dr.-Ing. Lukas Barchewitz

2008

In-flight Air Supply System for PEM Fuel Cells

Von der Fakultät für Maschinenbau

der Gottfried Wilhelm Leibniz Universität Hannover

zur Erlangung des akademischen Grades

Doktor-Ingenieur

genehmigte Dissertation

von

Dipl.-Ing. Lukas Barchewitz

geboren am 09. Oktober 1975 in Kattowitz

2008

Stichworte

PEM-Brennstoffzelle, Fluganwendung, Luftversorgung, Turbomaschinenauslegung, Auslegungsoptimierung, Regelung

Keywords:

PEM fuel cell, flight application, air supply, turbomachinery design, design optimisation, in-flight controls

Prüfungskommission:

Vorsitz:	Prof. Dr.-Ing. B.-A. Behrens
1. Prüfer	Prof. Dr.-Ing. J. Seume
2. Prüfer	Prof. Dr.-Ing. A. Luke

Tag der Promotion: 11. Dezember 2007

Abstract

With on-going development of fuel cells and operational experience, fuel cells are also considered for continuous power generation in the exigent flight application. Here, low power specific weight and high electric efficiency are primary requirements.

The air supply system represents a core interface of the FC to the ambient, which has impact on the operational range, stability and controllability of the FC system. Radial turbomachinery is found to be most promising for the in-flight integration with PEM-FC. The air supply system resembles a turbocharger, which is electrically supported. A dedicated turbomachinery design is essential for an optimised operating strategy regarding mass flow range, power demand, and system response.

Safe and quick transients of the air supply in combination with stack dynamic operation are achievable. Application a decoupled controller improves the controller performance and eliminates critical operating conditions for the compressor. The controlled air supply system covers the entire operational range based on a reference flight envelope and also handles extreme operating scenarios.

Kurzfassung

Aufgrund des fortschreitenden Entwicklungsstands und zunehmender Betriebserfahrungen wird die Einsetzbarkeit von PEM-Brennstoffzellen in der anspruchsvollen Fluganwendung untersucht. Bei der Anwendung zur kontinuierlichen Bordenergieversorgung kommen einem geringen leistungsspezifischen Gewicht und einem hohen elektrischen Wirkungsgrad eine besondere Bedeutung zu.

Das System zur Luftversorgung stellt das wichtigste Verbindungsglied mit der Umgebung dar und beeinflusst Systemeigenschaften der Leistungseinheit wie Betriebsbereich und Regelbarkeit. Radiale Turbomaschinen werden den Anforderungen in dieser Anwendung gerecht, müssen jedoch für einen optimierten Betrieb hinsichtlich des Betriebsbereichs, der Leistungsaufnahme und der Systemdynamik gezielt ausgelegt werden. Die Anordnung der Turbomaschinen ist der Turboladeranwendung entlehnt.

Unter Berücksichtigung der dynamischen Eigenschaften des Stacks kann das Luftversorgungssystem schnell und zuverlässig geregelt werden. Eine Entkoppelung erhöht die Regelgüte und umgeht kritische Betriebszustände im Verdichter. Der Regler zeigt gutes Verhalten im ganzen Betriebsbereich einer Flugmission und deckt auch extreme Lastwechsel ab.

Preface

This work is based on research carried out between 2003 and 2007 during my appointment as research assistant at the Institute of Turbomachinery and Fluid Dynamics at the University of Hannover, Germany. It was embedded in a development strategy for the successful integration of PEM-FC technology into the civil aircraft environment. Uwe Wollrab, Airbus Deutschland GmbH, and Peter Schumann, DLR Stuttgart, are gratefully acknowledged for their support in flight-specific and PEM-FC topics, respectively.

I am highly grateful to my supervisor Professor Jörg Seume for his guidance and help throughout my time at the institute and the necessary support in initiating such a promising research topic. Through him, I have learned how a structured co-operation between research and industry can accelerate the development of new technologies. My senior engineer Roman Pietrasch proved, along the way, to be an excellent strategic advisor and has taught me not to forget the global goal of my work.

Thanks go to Tom Steglich, who was not just a good advisor on difficult topics on radial compressors but more besides and to Katharina Fischer for the exchange of ideas between us concerning fuel cell themes. Improvements of my work came from many discussions with André Hildebrandt with whom I share a passion in turbomachinery and their challenging combination with fuel cells. I would like to thank Bastian Schreyer, Sebastian Kanzer, David Müller, Alexander Beil, and all my colleagues who changed the institute from a working into a living place. Thanks go to Katrin Erdmann for reviewing the script.

I want to thank Carsten Remmert who has stayed advisor and best friend.

I am deeply grateful to those who are most important in my life: My father and my mother for the love and support in all my decisions. My wife, Céline, who stood behind me during both the good and bad times of my thesis. And to my children, Lea and Anna, for simply being.

Ad Maiorem Dei Gloriam

Hannover, September 2008

Lukas Barchewitz

Contents

Abstract ..... **I**

Kurzfassung ..... **I**

Preface ..... **III**

Contents ..... **IV**

Nomenclature ..... **VI**

1 Introduction **1**

- 1.1 Background and Motivation 1
- 1.2 Objectives 3
- 1.3 Methodology 3
- 1.4 Overview 4

2 Conceptual Analysis of the Air Supply System **6**

- 2.1 Requirements and Boundary Conditions in the In-flight FC Application 6
- 2.2 Application of Radial Compressors 10
- 2.3 Application of the Turbocharger Architecture 12
- 2.4 Integration of the Reformer Compressor 13
- 2.5 Flight Operation at Varying Altitudes 15
- 2.6 Operating Restrictions due to Extreme Ambient Conditions 17
- 2.7 Operating Restrictions due to Aerodynamic Boundary Conditions 19
- 2.8 Increasing Operational Flexibility by Advanced System Design 21
  - 2.8.1 Application of a Compressor Blow-off Valve 21
  - 2.8.2 Application of Compressor Inlet Guide Vanes 21
  - 2.8.3 Application of a Post-combustor 21
  - 2.8.4 Cathode Pressure Strategy 22
- 2.9 Concept Choice and Further Approach 23

3 Radial Compressor Design and Optimisation **24**

- 3.1 Design Strategy Considerations 24
- 3.2 Basic Aerodynamic Relationships and Non-dimensional Parameters 25
- 3.3 Inducer Design 29
- 3.4 Discharge Design 30
- 3.5 Diffuser and Volute Design 31
- 3.6 Design Procedure 33
- 3.7 Design Optimisation 35
  - 3.7.1 Definition of Design Specifications 35
  - 3.7.2 Optimisation Limits 36
  - 3.7.3 Decrease of Input Variables for the Design Procedure 38
  - 3.7.4 Multi-objective Optimisation 39
  - 3.7.5 Optimum Pressure Ratio Split for the Two-stage Compression 40
  - 3.7.6 Comparison between the Single-stage and Two-stage Compression 40

4 Process Modelling **43**

- 4.1 Radial Compressor 43
  - 4.1.1 Slip Factor 43
  - 4.1.2 Aerodynamic Loss Models 45
- 4.2 Radial Turbine 45
- 4.3 Pressure Loss 46

4.4 Further Components 46
4.5 Dynamic Process Modelling 47
4.5.1 Radial Compressor 47
4.5.2 Shaft Dynamics 48
4.5.3 Plena 49
4.5.4 Compressor Stability Aspects and Surge Modelling 50
5 Steady-state Air Supply System Analysis 54
5.1 Improvement of the Drive Power for Constant Cathode Mass Flows 55
5.1.1 Cathode Pressure Function 57
5.1.2 Influence of the Cathode Pressure Loss 61
5.1.3 Influence of the Turbomachinery Design 62
5.1.4 Influence of Co-firing with Additional Kerosene 64
5.2 Improvement of the Mass Flow Range 65
5.2.1 Influence of the Cathode Pressure on the Mass Flow Range 67
5.2.2 Influence of the Cathode Pressure Loss on the Mass Flow Range 68
5.2.3 Influence of the Turbine Design on the Mass Flow Range 69
5.2.4 Influence of Co-firing on the Mass Flow Range 70
6 Controls Optimisation Using a Simplified PEM-FC Model 72
6.1 Open-loop Analysis 73
6.2 Controller Requirements and Controller Architecture 76
6.3 Input-Output Pairing 77
6.4 Coupled and Decoupled Single-Input-Single-Output (SISO) Control Approach 79
6.5 Validity of the Decoupled SISO Controller for the Entire Altitude Range 83
6.6 Multiple-Input-Multiple-Output, Linear-Quadratic-Gaussian Control Approach 84
6.7 Validation of the Control Architecture and Tuning with an Advanced PEM Model 87
7 Response Analysis Using an Advanced PEM-FC Model 89
7.1 System Behaviour during PEM-FC Step Load Scenarios 89
7.2 System Behaviour during PEM-FC and Reformer Step Load Scenarios 90
7.3 Extended Operational Flexibility by Advanced Cathode Pressure Function and Turbine Design 90
7.4 System Behaviour during Typical On-board Load Scenarios 91
8 Conclusions 94
9 Outlook 96
Bibliography 98
List of Figures 104
List of Tables 107
Appendix 109
A Concept Analysis 109
B Aerodynamic Design of an Radial Compressor Impeller 111
C Turbomachinery Loss Modelling 119
D Steady-state System Analysis 125
E Transient System Analysis with an Advanced PEM-FC model 128

Nomenclature

Latin symbols

A	m^2	area
	-	state matrix
a	m/s	sound velocity
B	-	B-parameter
	-	input Matrix
b	m	width
C	-	output matrix
c	m/s	absolute velocity
c_{dis}	-	dissipation coefficient
$c_{d,T}$	-	turbine discharge coefficient
c_f	-	friction coefficient
c_p	KJ/(kg K)	isobaric heat capacity
	-	pressure recovery coefficient
c_s	m/s	spouting velocity
D	m	diameter
	-	decoupling matrix
	-	feedthrough matrix
deH	-	diffusion ratio
F	-	correction factor
G	-	process transfer matrix
g	m/s2	gravitational acceleration
h	m	altitude
	J/kg	enthalpy
J	kgm^2	moment of inertia
	-	cost function
K	-	constant
	-	feedback gain
L	m	length
	K/m	temperature lapse rate
L_{imp}	m	impeller passage length
Ma	-	Mach number
Mu	-	non-dimensional speed
$\dot{m}$	kg/s	mass flow
n	1/s	shaft speed
P	kW	power
p	Pa / bar	pressure
R	J/(kg K)	gas constant

r	m	radius
Re	-	Reynolds number
T	K	temperature
u	m/s	circumferential velocity
	-	output vector
V	m^3	volume
$\dot{V}$	m^3/s	volume flow
W	m^2/s^2	loss work
W_{nd}	-	power coefficient
$\dot{W}$	kW	power
w	m/s	relative velocity
x	-	state vector
z	-	blade number

Greek symbols

α	°	flow angle
β	°	blade angle
Δ		difference
η	-	efficiency
Φ	-	flow number
κ	-	specific heat ratio
λ	-	work factor
λ	-	gain factor
μ	-	slip factor
ν	-	radius ratio
	m^2/s	kinematic viscosity
ν_H	-	hub to shroud ratio of the radial compressor
ν_{Diff}	-	diffuser radius ratio of the radial compressor
π	-	pressure ratio
ρ	kg/m^3	density
τ	Nm	torque
ω	-	circumferential velocity
ξ	-	loss coefficient
Ψ	-	head coefficient

Subscripts

0	standard condition
1	compressor impeller inlet
2	compressor impeller outlet / compressor diffuser inlet
3	compressor diffuser outlet / compressor volute inlet

4	compressor volute exit cone inlet
5	compressor volute exit cone outlet / compressor outlet
6	turbine inlet
8	turbine rotor outlet
ad	adiabatic
amb	ambient
b	blade
c	compressor
cl	clearance
crit	critical
Diff	diffuser
diff	diffusion
eff	effective
exh	exhaust
fri	friction
H	hub at compressor impeller inlet or Helmholtz
h	hydraulic
imp	impeller
inc	incidence
is	isentropic
m	motor meridional
max	maximum
mech	mechanic
opt	optimum
p	plenum
pass	passage
pre	pressure side
red	reduced
ref	reference state
rel	relative
rot	rotor
S	shroud at compressor impeller inlet
s	static
suc	suction side
T	turbine
TP	tropopause
t	total
turb	turbine
u	circumferential
vol	volute

Abbreviations

AEA	All electric aircraft
APU	Auxiliary power unit
ATR	Auto-thermal reforming
BoP	Balance-of-Plant
FC	Fuel cell
GT	Gas turbine
IGV	Inlet guide vanes
ISA	International standard atmosphere
MEA	More electric aircraft
PEM-FC	Proton exchange membrane fuel cell
POX	Partial oxidisation
RGA	Relative Gain Array
SOFC	Solid oxide fuel cell
TIT	Turbine inlet temperature
TC	Turbocharger
VTG	Variable turbine geometry

1 Introduction

1.1 Background and Motivation

In order to meet the increasing demand of on-board electrical power in civil aircraft and for the further reduction of emissions, the conventional auxiliary power unit (APU) shall be replaced by a fuel cell system. Proton exchange membrane fuel cells (PEM-FC) are favoured because of their currently advanced development level.

During each stage of a flight, electric, pneumatic, and hydraulic power is required and is supplied by the main engines. For on-ground power supply, the gas turbine auxiliary power unit (APU) generates the power and is situated in the tail cone of the plane. It is also used for starting the main engines and as an emergency back-up in case of damage to one engine or in case of electric system damage during flight. State-of-the-art APUs are extremely robust and have a low specific weight and low specific volume in regard to power. However, they are noisy and exhibit low efficiency (Adamson, K-A. (2005), Daggett, D. (2003)).

Due to decreasing allowable emission levels at airports, airlines will be steadily forced to either improve this technology or to purchase the expensive ground energy service provided at the airport. Fuel cells exhibit a technically clean exhaust gas with the stack operating noiseless. The stack can operate in a wide power range at considerably higher efficiency and could therefore contribute to a decrease in CO_2 emissions at airports. A second important reason for considering fuel cells for on-board power conversion is the increasing electric power demand in the cabin throughout the entire flight envelope, which is answered by the new aircraft development strategy of a “more electric” or even “all electric” aircraft (MEA/AEA). Hydraulic and pneumatic systems are then gradually replaced by electric actuators. This suggests the conceptual design of a continuously operating power unit, meeting all power demands throughout an aircraft’s operating year (Daggett, D. (2005), Rothammer, W. (2005)). Unlike in present aircraft, the main engines would then be completely decoupled from electrical power generation and used for thrust only.

Based on these requirements, fuel cell systems seem to meet future demands regarding emissions and efficiency. A further synergetic advantage arises of the chemically pure water which is available in the exhaust gas as a result from the chemical reaction at the membrane. Due to the low membrane temperature of 80°C, it is already in the liquid phase and can be separated without great technical effort. If used as service water, the aircraft take-off weight can be decreased significantly.

Both the PEM-FC and Solid Oxide Fuel Cell (SOFC) offer advantages for this application but impose also technological challenges on aircraft manufacturers. Boeing, e.g., favours SOFC-systems for further integration in the flight environment due to the low requirements for anode gas when compared to all other FC types (Bundschuh, N. (2005), Eelman, S. (2003), Freeh, J. (2005)). The reasons for considering PEM-FC on-board can be explained with a much lower power specific weight and volume when compared to SOFC. PEM-FC technology is more mature due to a longer development history and has gained more accumulated operating hours. Furthermore, PEM-FC's are more robust regarding mechanical shocks and temperature fluctuations, which are crucial requirements for the flight application. However, generating sufficiently pure H_2-gas from kerosene and the required fuel flexibility have to be named as the most important challenges for integrating PEM-FC into the flight environment. Here, the development and application of high-temperature PEM-FC might reduce the integration efforts as they show a much greater tolerance to CO impurities, which decreases the operational requirements for the gas processing path.

Without any dependence on the fuel cell type, FC systems must be supplied with air both for reaction and cooling purposes. The air supply system is the interface between the FC and the ambient and provides air according to the power output demand of the PEM-FC. In the flight application, the inlet conditions of the air supply system undergo extreme changes throughout the flight envelope. Failure of air supply components would lead to a shut down of the FC unit, which affects the power supply on-board. This demonstrates the importance of its overall reliability. The impact of the air supply architecture, the choice of its components, and their design on operating range and stability are subject of the present work.

An important boundary condition for the air supply design is the cathode pressure. Operation at near standard atmospheric conditions throughout the entire flight envelope has an important advantage as it allows the application of state-of-the-art stacks. Furthermore, the power specific weight and volume not only of the stack but of the entire gas processing path can be decreased (Bundschuh, N. (2005), Pratt, J. (2003)) significantly. As ambient pressure at cruising flight is at around 0.2 bar, the air has to be compressed considerably and conditioned before entering the cathode. Considering this boundary condition, this can be regarded as pressurisation of the system, which is already known from automotive PEM-FC applications and SOFC-gas turbine systems.

At present, no demonstrator system or experimental experience of an air supply system are available in the here discussed configuration, while only little analytical work is found addressing the specific air supply and turbomachinery design. No scientific publication exists on the dynamic analysis of the interactions between the air supply system and the PEM stack.

For automotive applications, different air supply architectures have already been suggested which consider also possible control strategies (Lang, O. (2004), Kulp, G. (2001), Rodatz, P. (2005)). However, as operational requirements, e.g. pressure ratio range, ambient conditions, and life-time differ strongly, synergies with the present discussion are limited. Unlike in these papers, this work considers the expansion of the burnt stack off-gases for running the compression process, which significantly changes system dynamics and controls. It will be shown that only a thermo-mechanical drive of the compression process is an acceptable concept regarding the internal energy flow and system efficiency.

1.2 Objectives

This thesis aims at establishing comprehension of the steady-state and transient interaction between the air supply system and the PEM-FC in the flight application.

In detail, the primary interests of this work are to define how the air supply system and namely the turbomachinery characteristics have to be chosen (a) to allow a stable operation for a “more electric” flight envelope, (b) to improve operational flexibility regarding mass flow range and system response, and (c) to increase overall system efficiency by minimisation its power demand.

Viewing the little analytical work on this topic, this work has also guideline character for supporting the integration of turbomachinery into the PEM-FC flight environment. It shall contribute in-flight FC to become a reliable, robust and commonly accepted technology on-board of civil aircraft.

1.3 Methodology

In order to attain the objectives stated above, this work comprises the analysis of (a) the optimum conceptual design, (b) the turbomachinery design and optimisation, and (c) the steady-state and transient system characteristics of the entire power unit. A core concern of this work is to not leave these three analysis steps independent. Neither should they be regarded as sequential steps. Their interdependencies are found by a systematic approach and used in a synergetic way. It will be shown that this methodology initiates a superior optimisation process and is more effective than if the analysis steps are applied in a sequential way.

Mathematical models and tools cannot be the same for each analytical step as these have different sub-tasks. During the conceptual design for example, simple assumptions of the design output and fairly accurate part-load characteristics are applied. These are based on the basic physical understanding of the components and allow a quick assessment of a whole set of numerous concept variations. They will, however, not suffice for detecting the minimum or maximum mass flow of a suitable compressor. In this case, they have to be replaced by more suitable (aerodynamic) models. They have to be sufficiently accurate to guarantee a reliable performance prediction, on the one hand, but have to keep calculation time at a reasonable level when integrated into optimisation procedures or time resolved transient models, on the other hand. Modelling depth, calculation procedures, and evaluation criteria are therefore adjusted for each analysis step and weighed by the accuracy requirements of the actual physical or mathematical problem.

While the conceptual analysis can be done with a simple calculation software such as Excel, the turbomachinery design and optimisation as well as the steady-state analyses are carried out with the programming environment Matlab® (Version 7.01, R14, Service Pack 1). It offers a remarkable library of mathematical functions for problems occurring in applied sciences including the optimisation functions used here. The dynamic analyses are carried out with Simulink®, which is directly designed for the simulation and evaluation of dynamic and controlled systems. It offers by itself a broad function library with classical and modern evaluation tools. It is designed for Matlab® and its programming structure and is therefore widely used both in academic and commercial circles.

1.4 Overview

The following section gives an outline for understanding the content and the structure of this work.

Based on a description of the operating boundary conditions of a FC power unit and a catalogue of design requirements, Chapter 2 presents suitable compression and expansion technologies and outlines their operating limits. A systematic approach reveals the basic arrangement of the air supply components which adequately satisfies the requirements catalogue. Possible operating restrictions are analysed which may occur from varying ambient conditions. Finally, a short overview is given, how the operational flexibility can be increased by conceptual means.

After a general introduction into core aerodynamic parameters of radial compressors in Chapter 3, the here used design strategy and procedure for radial turbomachinery is developed on the basis of dimensionless numbers. Assumptions and limitations of each compressor section are discussed and integrated into one design algorithm. The turbomachinery design appears to be a highly complex task with numerous free variables as inputs. The interested reader is referred to the Appendix B where the interdependencies between aerodynamic and dynamical parameters are outlined. In a subsequent step, the design algorithm is embedded into an optimisation algorithm which follows in-flight PEM-FC specific requirements and which is finally extended to a multi-objective optimisation procedure. The newly developed tool allows addressing questions about the appropriate turbomachinery design such as single-stage or two-stage compression and the corresponding optimum pressure ratio split. The procedure is designed to integrate additional fuel cell or flight specific boundary conditions and requirements in order to evaluate their sensitivity on overall performance and to identify aero-thermodynamic restrictions.

Chapter 4 presents the thermodynamic, aerodynamic and transient models which are applied in this work. The turbomachinery description is based on a highly detailed model which has been validated against a whole set of suitable turbocharger compressors and turbines. The pneumatic description of the system is based on a classical approach but extended for the sequential arrangement of pneumatically lumped volumes with specific pressure loss characteristics.

Chapter 5 gives an overview of sensitive parameters for optimum air supply design and their influence on operation range, addressing PEM-FC characteristics, turbomachinery design issues, and conceptual choices such as the application of a post-combustor. The importance of the adaptation of the cathode pressure to the operating altitude is detected early and applied in the further analyses. While this chapter reveals clearly which key issues are important during air supply design, the additional co-firing with kerosene remains an option with counteracting tendencies for the overall benefit.

Chapter 6 enters into the transient system analysis of the entire system. An open-loop analysis gives insight into the general dynamic character of the system. Proposing a simple but reliable controller architecture for the air supply system, the appropriate input-output pairing and tuning of the controller is carried out with classical design tools. Its validity for the entire flight envelope range is proven. A modern control approach, the Linear Quadratic Gaussian controller, is applied to demonstrate the potential to increase controlling performance and minimising controlling action. The results in this chapter are obtained with a simple, quasi-steady PEM-FC model to accelerate the controller design procedure but finally validated successfully against a highly resolved PEM-FC model.

Chapter 7 considers the influence of the additional free parameters occurring from the advanced PEM-FC model such as different load and reformer transients. All considerations deduced in this work are superposed to demonstrate their effectiveness and are applied successfully to an extreme operating scenario for the power unit. Finally, the controlled system is calculated for the entire flight envelope based on a more electric aircraft power demand, where it proves stable and safe operation.

2 Conceptual Analysis of the Air Supply System

The analysis presented in this chapter identifies possible system configurations and detects the most suitable compression and expansion techniques. In order to give chance to introduce a completely new concept, a systematic top-down approach is applied. The model description for this section remains at the black-box level defining only the necessary values at the unit interfaces. Once the system architecture is defined, the simplified assumptions will be replaced by highly detailed aerodynamic and fully transient models.

2.1 Requirements and Boundary Conditions in the In-flight FC Application

The design requirements for the air supply are defined by (a) system level specifications demanded from the entire FC-power unit, such as design power output, operating range and system response, (b) by the integration with a FC stack and thus its operating conditions, e.g. cathode inlet temperature and pressure, and by (c) the interface characteristic of the air supply system to the ambient and thus the changing ambient conditions, which are specified by the envelope of a standard flight, comprising different sections of an entire flight mission. The result is a highly evolved requirement specification.

From system level, the design requirements for the air supply are, basically, valid for the entire envelope and can be summarised with a descending priority as follows:

- Low system weight and volume
- High availability
- Low cost
- Low power consumption
- Autonomous operation and start-up
- Least number of devices
- Good controllability as well as quick and safe system response
- Low noise emissions
- Based on state-of-the-art technology

There can be no doubt, that not all of the stated requirements can be fully achieved with one technically feasible solution. The task of the analysis presented in this section is therefore to reveal the optimum concept and to detect air supply components which cover the catalogue of requirements as completely as possible.

At this point, it shall be outlined further why autonomous operation is required. The strategy to use cabin air would clearly facilitate the system design. It would even lead to excess power if the stack exhaust gases are expanded to the ambient at high altitudes but has a crucial disadvantage. In case of decompression of the cabin during emergency, the cathode pressure and thus power output of the stack would consequently decline, which might even evoke a breakdown (when the membrane is cooled down by the ambient air beneath 0°C) of the electric power supply in the most critical moment. This is believed to be an exclusion criterion for the certification.

The design requirements directly imposed by the combination with a PEM-FC are:

- Constant cathode inlet conditions
- Low pressure fluctuations at cathode inlet
- Operational flexibility regarding mass flow and pressure at cathode inlet

and must be fulfilled throughout the entire envelope. The ambient conditions, which are the inlet conditions for the compression device as function of the altitude, are defined by the International Standard Atmosphere (ISA), which defines the ambient temperature in the troposphere (h<11000 m) by

$$T = T_0 - L \cdot h \qquad \text{Eq. 2-1}$$

with the standard sea level temperature T_0=288.15 K, the lapse rate L=0.0065 K/m and the altitude above sea level h. The ambient pressure is

$$p = p_0 \cdot \left(\frac{T}{T_0} \right)^{\frac{g}{L \cdot R}} \qquad \text{Eq. 2-2}$$

with the standard sea pressure p_0=101,325 Pa, the gravitational acceleration g=9.81 m/s^2, and the gas constant for air R=287.04 J/(kg K).

Civil aircraft reach their cruising altitude for long-distance flights at a maximum of 12500 m, which is in the stratosphere and situated above the so called tropopause at 11000 m. It can be well approximated that the ambient temperature in the troposphere remains constant at 216.65 K resulting in the pressure definition

$$p = p_{TP} \cdot e^{\left(\frac{g \cdot (h_{TP} - h)}{R \cdot T_{TP}} \right)}, \qquad \text{Eq. 2-3}$$

where TP indicates the ambient conditions in the tropopause. The ambient temperature and pressure as function of altitude are plotted in Fig. 1.

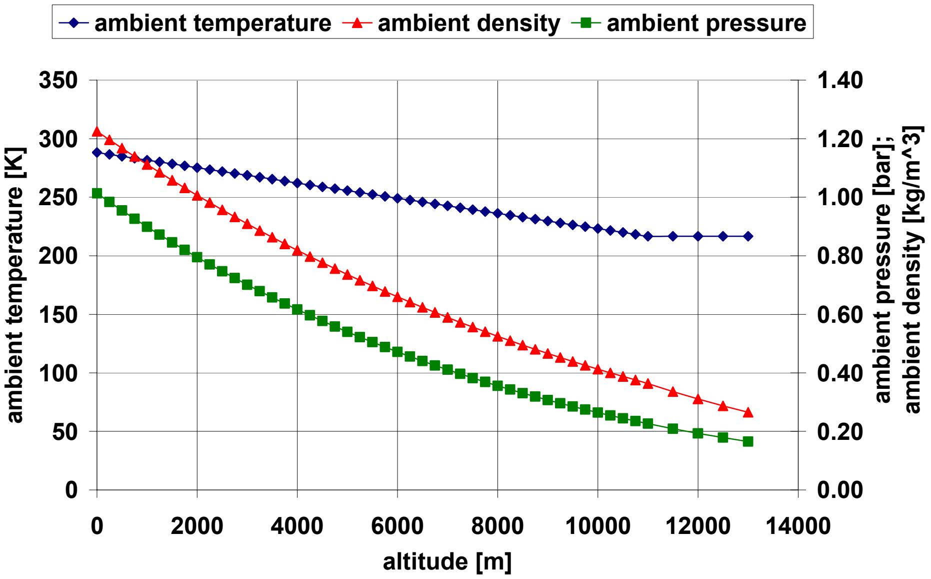

Fig. 1 Ambient conditions in the stratosphere and troposphere vs. altitude

Consequently, the ambient pressure at cruising altitude of 12500 m falls to 0.179 bar and a constant mass flow soaked up for compression increases its volume flow by the factor of 4, which will be of great importance for the subsequent considerations. The typical operating range for commercial APU in civil aircraft (Fig. 2) must be covered by future FC-system and will be therefore used as a starting ground for the present analysis. Unlike for gas turbine auxiliary power units (GT-APUs), there will be no distinction between the operating mode for bleed air and shaft power or shaft power generation only, as the FC will generate solely electric power. A starting limit with batteries or re-starting limit with bleed air from the main engines is not of importance for the present system, while breakdown scenarios of the FC will not be considered here.

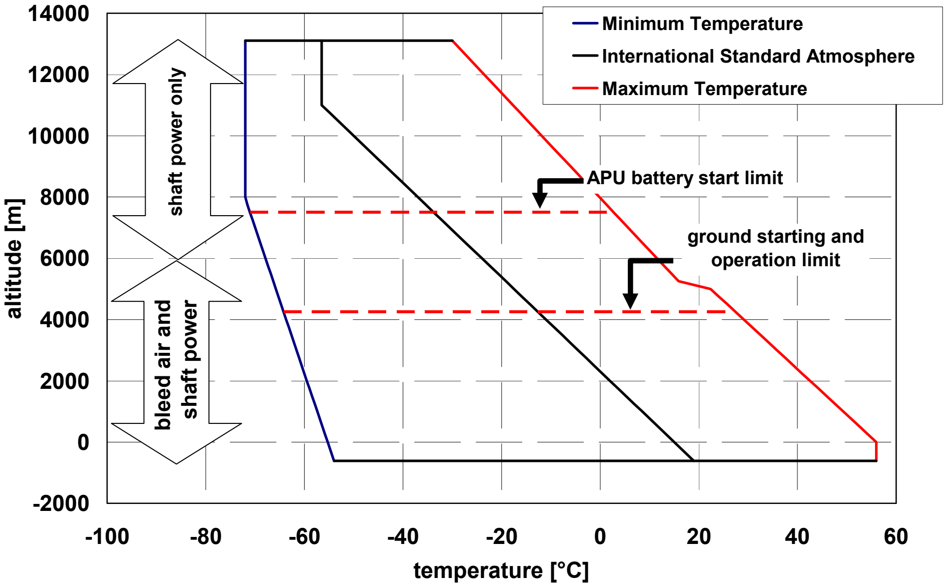

Fig. 2 Operating range of a commercial APU

The middle line represents the correlation between altitude and temperature following the ISA standard. Temperature deviations to lower and higher values may occur at every altitude. If operating restrictions exist due to temperature deviations at altitudes beneath 4450 m (Fig. 2) will be discussed in Section 2.6, p.17.

The typical flight envelope of civil aircraft, the electric demand, and the corresponding operating altitude are shown in Fig. 3. After a start-up and taxi-out period, the climb phase is finished after 23 min with a short manoeuvre climb pause at approximately 3000 m. The cruising phase takes 160 min followed by the descent phase with a duration of 29 min.

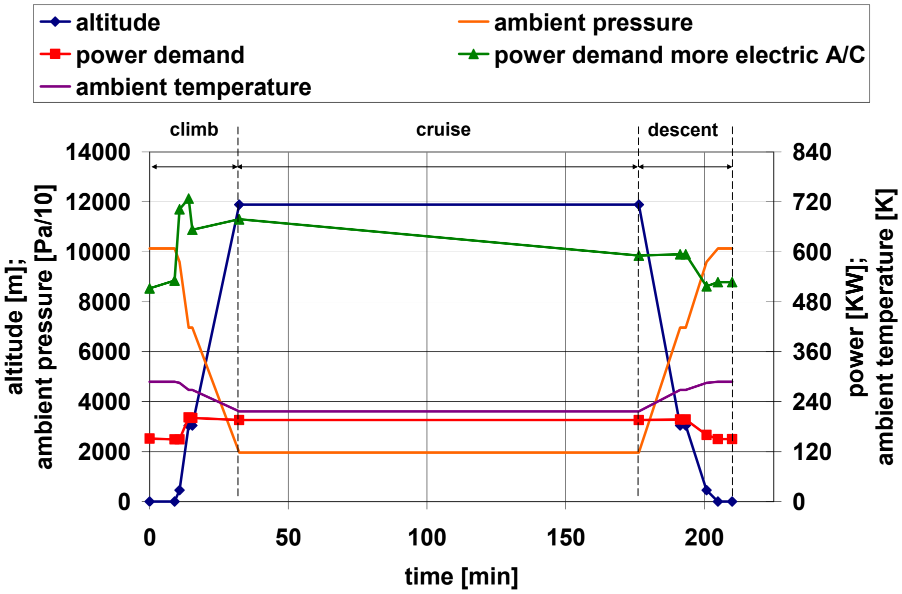

Fig. 3 Flight envelope parameters and boundary conditions

The electric load demand throughout the envelope (Fig. 3) is increasing until cruising altitude is reached and remains almost constant until the descent phase is started. The more electric concept, however, shows a significantly higher power demand and is characterised by more load changes which occur even abruptly.

In order to understand the issues related to the combination with a PEM-FC, the fuel cell system and its components shall be briefly described. In our case, the FC system consists of the stack itself, the power control device and a kerosene reformer with an auto-thermal reactor (ATR), a low-shift reactor, and a partial oxidisation (POX) reactor, see Fig. 4. Air is needed in the stack cathode, the ATR and the POX reactor, but at different pressure levels and mass flows, which has to be covered by the air supply system. Water can be removed directly at the cathode. A portion will be recycled to the reforming process, while the excess water might be used for service water.

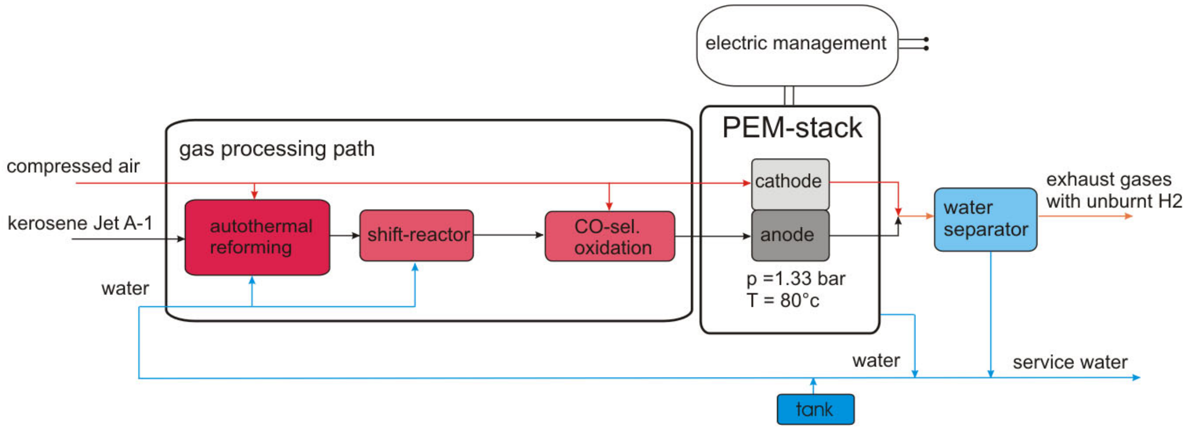

Fig. 4 Schematic flow sheet of the PEM-FC

In our system, the cathode inlet pressure is set to 1.33 bar which is derived from an assumed pressure loss of 0.25 bar and 0.05 bar across the cathode and the humidifier, respectively, resulting in an effective outlet pressure of 1.03 bar. This is above the standard ambient pressure at 0 m and eliminates back flow into the cathode at ground operation. The cathode pressure is also within the pressure range of state-of-the-art PEM-stacks and is held constant for the entire operating altitude range. It will be shown later in Chapter 5, p.54, that an adapted cathode pressure throughout the envelope shows significant advantages for both overall system efficiency and mass flow operating range. The inlet pressures for the ATR and POX with 2.66 bar may be somewhat high but offer a margin for necessary controls. The outlet temperature of the cathode off-gases is 80°C and the relative humidity of the stream is 100%, which is typical for state-of-the-art PEM-FC, while the rest of water is in liquid phase and not entering the expansion device. Regarding the cruising altitude of 12500 m, one can calculate that the air has to be compressed from 0.179 bar to 1.33 bar resulting in a pressure ratio of around 7.5 for the cathode air and 15 for the reformer air. An overview of the boundary conditions and assumptions valid for the entire work is given in Tab. A-1, p. 109.

2.2 Application of Radial Compressors

For the needed compression process, only two compressor technologies can meet the requirements: Screw compressors and radial compressors. The advantages of screw compressors are their extremely broad operating range without stall or surge at small mass flows. They can be controlled by shaft speed control and throttle valve displacement up- and downstream of the compressor. Their main disadvantages are their relative high specific weight and volume, a low isentropic efficiency of regularly less than 60%, the necessity of oil injection at compression ratios above 4.5 for cooling purpose and relatively small shaft speeds of 3000 to 10000 rpm, which implies the need of an electric drive or a gear box. Screw compressors are extremely noisy (more than 100 dB when not sound-proofed) and produce a highly pulsating outlet pressure amplitude, which can only be reduced by the installation of a large-volume compensating reservoir (Groth, K (1985), Fister, W. (1984)). Only little experience exists with screw expanders. Automotive applications e.g. superchargers are light but generally do not exceed pressure ratios of 2 and a life time of more than 5000 h. To the author's knowledge, no screw compressors are installed in state-of-the-art civil aircraft.

The advantages of radial compressors are their extremely low specific weight and volume and an achievable isentropic efficiency of 65% to 75%. They can be controlled by shaft speed, throttle valve displacement up- and downstream of the compressor, inlet guide vanes and diffusers with variable vanes. Radial compressors do not require cooling while reaching high pressure ratios of up to 8 in one single stage. Space saving multi-stage compression is possible by arranging the stages on one shaft. The outlet pressure shows very low amplitudes and can be recognised as non-pulsating. A major disadvantage is the so-called surge when un-stable operation occurs low mass flows and concurrently high pressure ratios. Maximum mass flows are obtained when distinct sections (impeller inlet, diffuser or volute) in the compressor reach choked flow. Radial compressors are used in state-of-the-art GT-APUs in the power and bleed air section of the APU and are therefore already certified for civil aircraft.

As the specific weight and volume are criteria of primary significance for optimum air supply design, radial compressors seem to be the favoured technology. The following consideration may further tip the scales in favour of radial compressors.

With a typical isentropic efficiency of 60% for screw compressors, disregarding the further compression of reformer air and assuming an ideal electric motor, the mechanical power demand for the compression of 0.18 kg/s is approximately 49 kW when applying the following expression

$$W_{mech,comp} = \dot{m} \cdot \frac{\kappa}{\kappa - 1} \cdot \frac{R_{air} \cdot T_{1t}}{\eta_{is}} \cdot \left(\pi^{\frac{\kappa - 1}{\kappa}} - 1 \right) . \qquad \text{Eq. 2-4}$$

With a radial compressor of 75% efficiency the power demand would decrease to 40 kW. Assuming a total power output of the corresponding FC of 80 kW, an electro-mechanically driven air supply would consume approximately 50% of the generated power, which is not acceptable.

With this rough calculation two important air supply design requirements can be stated. Firstly, the application of highly efficient compressor technique is of great importance for optimum overall performance. Secondly, it is crucial for optimum system efficiency to further decrease the parasitic air supply power demand. This can be achieved by the exergetic use of the FC exhaust gases and brings up the concept of a thermo-mechanical drive.

2.3 Application of the Turbocharger Architecture

Design alternatives for a thermo-mechanical drive are the coupling of a screw compressor and a screw expander or a combination of a screw compressor and a turbine. While the first combination results in an extremely heavy system when considering the compensating reservoir, the latter requires a heavy and expensive gear box of high transmission ratios due to the differing shaft speeds. A combination of a radial compressor and a radial turbine yields a turbocharger, which is a well-known, robust technology in stationary and mobile applications. The major advantage of radial turbines is their compactness and the possibility to apply variable turbine geometry (VTG), which allows the control of the shaft speed and thus the mass flow or pressure ratio. Even though turbochargers do not exist with the here required design specifications, the maturity of turbocharger technology gives reason to assume a feasible adaptation to the in-flight PEM-FC environment.

Firstly, we can assume an isentropic efficiency of 60% and a turbine inlet temperature of 80°C, which is identical with the stack outlet temperature. According to Eq. 2-5, the mechanical power from a radial turbine is 26 kW.

$$W_{mech,turb} = \dot{m} \cdot \frac{\kappa}{\kappa - 1} \cdot R_{exhaustgas} \cdot \eta_{is,turb} \cdot T_4 \cdot \left(1 - \pi^{\frac{1-\kappa}{\kappa}} \right) \qquad \text{Eq. 2-5}$$

It can be also seen that the power output is proportional to the inlet temperature, which makes a temperature increase desirable. This can be accomplished by the combustion of the unused hydrogen in the exhaust gas of the stack. Incidentally, the use of a post-combustor becomes necessary as unused hydrogen must not be released to the ambient due to airport safety and emission standards.

Based on the assumptions made in Tab. A-1, p.109, the remaining thermal power in the stack off-gases can be calculated with 50 kW. With a corresponding temperature increase by about 180 K and an improved turbine isentropic efficiency of 70%, the turbine provides then 45 kW. This represents a power excess of 5 kW when compared to the compressor power demand calculated above. The power excess balances the reformer air power demand, which has not been considered in the power balance yet. This concept is electrically self-sufficient and inherently fulfils the aforementioned system requirement of least power consumption.

At this step in concept analysis, some preliminary considerations about the suitable compressor configuration can be made. The here demanded high pressure ratio can be achieved with a radial compressor consisting of one single stage: It offers a compact arrangement, which is close to state-of-the-art turbocharger design. This requires, however, a vaned diffuser which is known to cause a steep and narrow compressor map and which again counteracts with the aforementioned requirement of a broad operating range. A two-stage compressor, on the other hand, facilitates the compressor design omitting a trans-sonic inducer section. It broadens the compressor map but might lead to a heavier compression system. As these alternatives diverge significantly in design targets, a trade-off between these alternatives is carried out in Chapter 3, p.24 and completed by a detailed aerodynamic analysis.

One possibility to reduce the design pressure ratio for both compression concepts is the use of a ram air intake. It recuperates a portion of the kinetic energy of the inlet flow caused by the forward motion of the aircraft into static pressure, see Eq. 2-6.

$$\frac{p_{0t}}{p_0} = \left(1 + \frac{\kappa - 1}{2} \cdot Ma^2\right)^{\frac{\kappa}{\kappa - 1}} \qquad \text{Eq. 2-6}$$

With an assumed maximum cruise Mach number of 0.8 and a recovery coefficient of 0.4, the maximum pressure ratio could be reduced to 6.2 and 12.4 (disregarding any pressure losses) for the cathode and reformer air, respectively. Though this option is not considered for the present analysis, it might help to decrease design efforts in future configurations.

2.4 Integration of the Reformer Compressor

Once the turbocharger architecture for the cathode mass flow is fixed, the reformer air path has to be addressed. It is of great advantage, when the entire air flow is compressed in one device, here the turbocharger compressor, before it is split into the reformer and cathode fraction. This avoids two high-pressure-ratio compressors, tends to result in an efficiency increase for the first compressor due to an increased mass flow, and provides a convenient decoupling of the reformer air compressor from the ambient and thus avoids strong deviations from off-design operation. As thermal power excess is available at the stack output, there exist several options to run the reformer air compressor. These are:

- On the shaft of the turbocharger (concept A, Fig. 5)
- With a separate radial turbine (concept B, Fig. 6)
- With a separate electric motor (concept C, Fig. 7)

As a power mismatch can be expected between the compressor and the turbine, a starter-motor-generator is introduced, which assures autonomous start-up and controllability of the entire air supply system. The electric motor can be arranged between compressor and turbine, which is known as “ebooster” in the automobile industry. Otherwise, a high-speed motor can be situated on the compressor side of the turbocharger. An obvious disadvantage of concept A is the decrease in controllability of the reformer air compressor as the shaft speed for both compressors is identical.

A second smaller turbine can be used for running the reformer air compressor while expanding the exhaust gases to the ambient (Fig. 6). The second turbocharger would be very small in weight and volume but represents an additional device and requires a three-way valve for high temperatures.

The most promising arrangement is concept C (Fig. 7) as maximum flexibility in controls of the reformer air and pressure can be expected due to a separate electric motor. This also leads to a possible arrangement for prototype applications, where emphasis is placed not on efficiency but feasibility demonstration. A final evaluation of the concepts is carried out in Section 2.9, p. 23

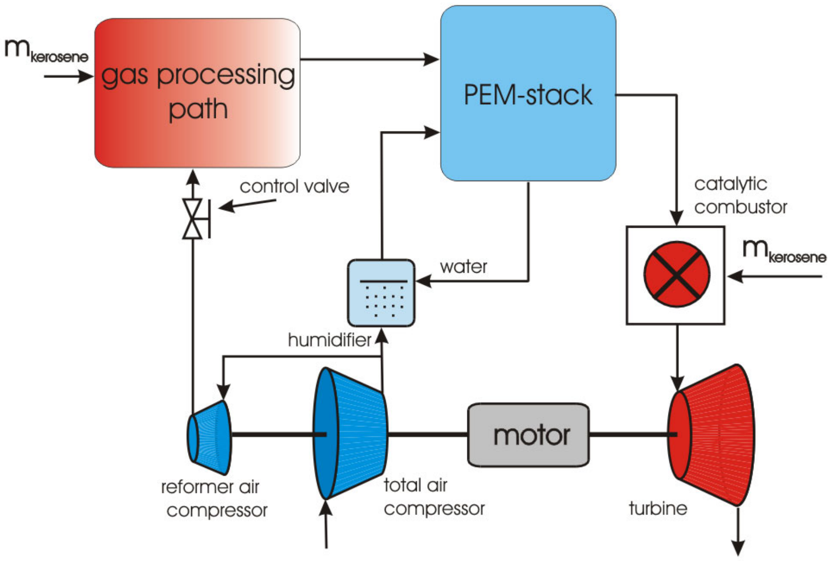
$m_{kerosene}$
gas processing path
PEM-stack
control valve
catalytic combustor
$m_{kerosene}$
water
humidifier
motor
reformer air compressor
total air compressor
turbine

Fig. 5 Concept A for the air supply system

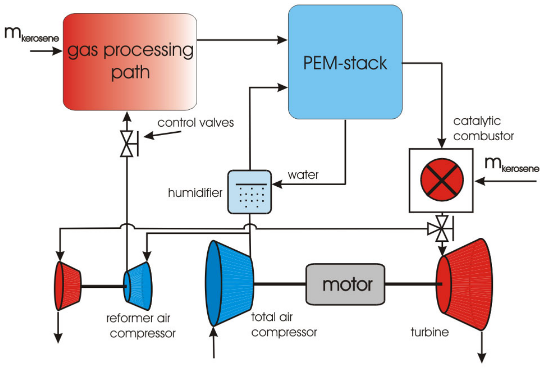
$m_{kerosene}$
gas processing path
PEM-stack
control valves
catalytic combustor
$m_{kerosene}$
water
humidifier
motor
reformer air compressor
total air compressor
turbine

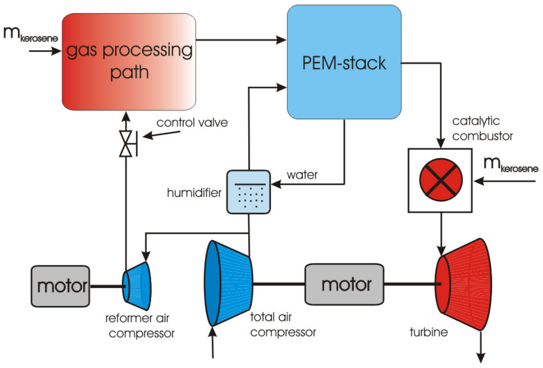
$m_{kerosene}$
gas processing path
PEM-stack
control valve
catalytic combustor
$m_{kerosene}$
water
humidifier
motor
reformer air compressor
motor
total air compressor
turbine

Fig. 6 Concept B for the air supply system with two turbochargers

Fig. 7 Concept C for the air supply system with electric drive for reformer compressor

2.5 Flight Operation at Varying Altitudes

As can be seen from the flight envelope in Fig. 3, the power demand is a maximum at the beginning of the cruising flight section. It is therefore set as design power output. For the present analysis, the power output of the FC and all inlet conditions at the gas processing path and the stack are held constant for every operating altitude.

This strategy allows extracting the impact of changing ambient conditions on the operating range of the air supply system. The corresponding design point assumptions during cruising flight are given in Tab. 1. As inlet conditions do not differ, the stack cannot “distinguish” at which altitude it works. This simplified approach will lead to extreme off-design operation for the compression system and give an essential basis for further analyses.

Tab. 1 Design point assumptions for the air supply system components

parameter	**value**	**unit**
$\pi_{\text{total air comp}}$	7.30	-
$\pi_{\text{reformer air comp}}$	1.69	-
π_{turbine}	5.89	-
$\eta_{\text{total air comp}}$	0.75	-
$\eta_{\text{reformer air comp}}$	0.70	-
η_{turbine}	0.70	-

The mechanical power demand of the total air compressor is shown in Fig. 8. A simple correlation for the efficiency of the compression process has been applied to account for part-load operation when pressure ratio and ambient conditions are changing with altitude. The reformer air compressor operates at constant pressure ratio (Fig. A-1, p.110), which was intended by the compressor arrangement. The only changing value is its inlet temperature, as pressure ratio of the total air compressor increases with altitude. Therefore the power demand increases with altitude from 2.2 kW to 3.1 kW. For simplicity, the isentropic efficiency of the reformer air compressor is assumed to remain constant.

The reformer air compressor power is not lost from an energetic and exergetic point of view. It increases the heat input to the reformer and allows thus a smaller amount of kerosene to be burnt for the reforming process.

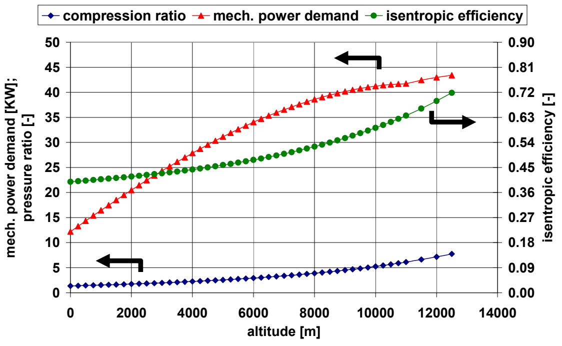

Fig. 8 Performance overview of the total air compressor

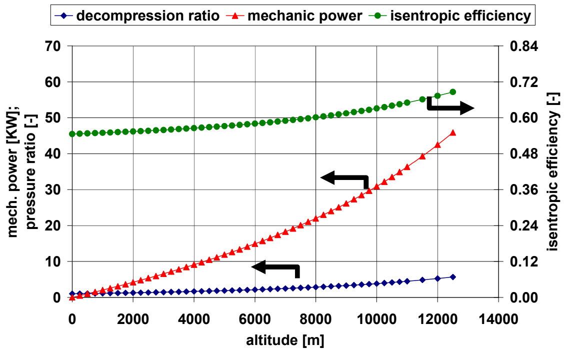

Fig. 9 Performance overview of the turbine

The turbine power output rises with altitude due to the increasing expansion ratio. The efficiency curve is highly simplified as the turbine model does not take into account the dependency of TIT and shaft speed. To outweigh this uncertainty, the turbine efficiency has been assumed conservatively with 70%.

Based on the component energy balances, an air supply energy balance can be depicted, see Fig. 10. The turbine inlet temperature of 530 K is obtained with the combustion of the unused hydrogen from the off-gases. It can be seen that the air supply does not consume any electric power from the FC at cruising flight conditions as has been deduced in the preceding section. At intermediate and lower operating altitudes, a power gap occurs between compression power demand and turbine output power and makes electric support necessary.

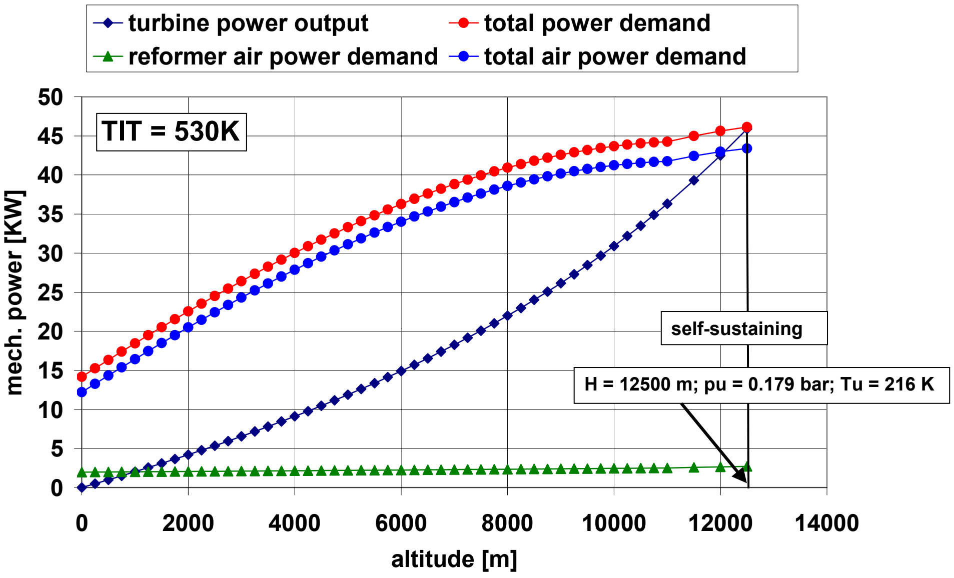

Fig. 10 Energy balance of the air supply system at TIT = 530K

An increase in TIT up to 1250 K can move operation without external electric power down to altitudes around 6000 m. However, it does not omit further demand for electric power for air supply operation below this altitude (see Fig. 11).

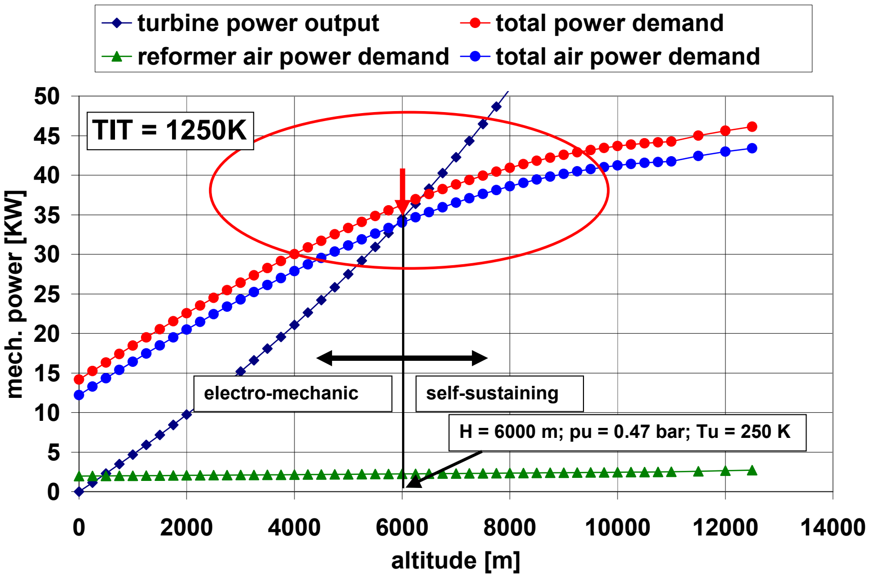

Fig. 11 Energy balance of the air supply system at TIT = 1250K

The assumption of a TIT of 1250 K represents a maximum value for uncooled turbine blades which can be designed with robust and cheap alloys and which limits the cooling efforts to a reasonable level.

2.6 Operating Restrictions due to Extreme Ambient Conditions

Extreme ambient conditions on the ground may impose operating restrictions. Therefore a brief assessment will be carried out. As can be seen from Fig. 1, p.8, great changes of the ambient conditions may occur at altitudes beneath 4380 m which must be covered by the FC-APU.

Tab. 2 Extreme scenarios for on-ground operation

location	T_{amb} [°C]	p_{amb} [bar]	rel. humidity [%]
snow desert	-54	1.013	50
desert	+56	1.013	30
high altitude	+28	0.558	50
Tropics	+40	1.013	100

Four on-ground operating scenarios at locations with extreme ambient conditions (Tab. 2) are picked out from the figure to verify if operation is possible and safe in principle. An important indicator to be evaluated is the temperature at the total air compressor outlet which is dependent on the compressor inlet temperature and the pressure ratio. The temperature of the cathode air, again, is a critical system parameter and has to be maintained at 80°C to ensure safe operation of the stack membrane.

All scenarios lead to off-design operation for the air supply system but are deduced to be feasible when based on the following considerations. Decrease of the ambient temperature leads to a decrease of the reduced mass flow moving the operating point towards the surge margin and vice versa. The corresponding changes for the reduced mass flow are in the range of 15%, which can be covered by the radial compressor. If compressor outlet temperature is beneath 80°C, subsequent heating of the air is optional as the stack can operate at lower temperatures. A trespassing of 80°C for the cathode inlet, on the other hand, has to be avoided to prevent the membrane from irreversible damage and represents therefore a possible bottleneck for operation afar from ISA ambient conditions. The scenario “tropics” might be critical for the stack due to the high ambient and therefore high total air compressor outlet temperature. Indeed, the compressor outlet temperature is too high at altitudes above approx. 4500 m even during operation at ISA conditions as can be seen from Fig. 12. A subsequent cooling of the compressor air is therefore obligatory.

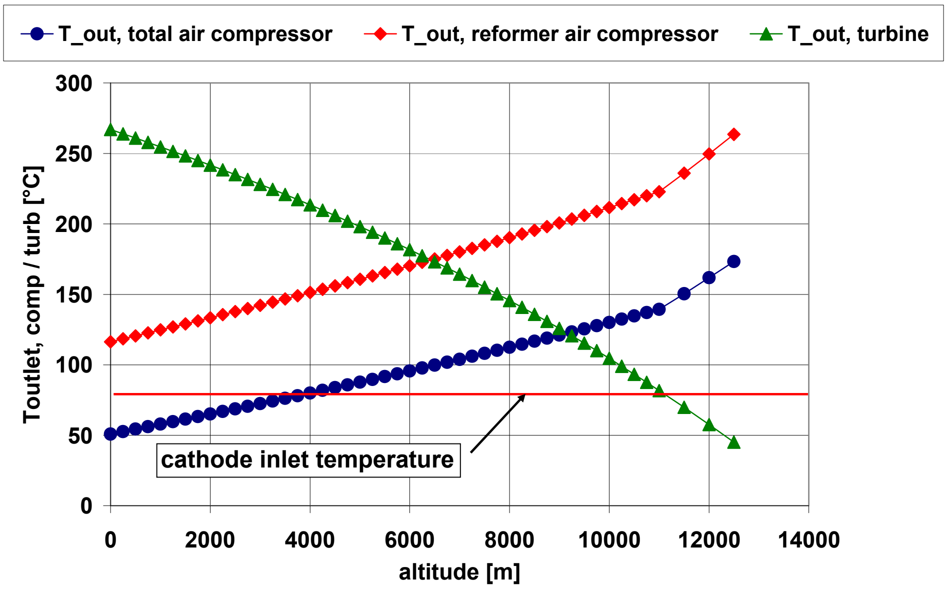

Fig. 12 Important temperature values of the air supply system

The question is inherently resolved by the humidification of the cathode air and omits the application of an additional heat exchanger. The most disadvantageous scenario for evaporation cooling is found in the scenario “tropics”. Fortunately, vapour pressure increases by 0.04 MPa between 40°C and 80°C and offers a sufficient heat sink to cool down the compressed air to 80°C.The humidification of dry air at cruising flight is sufficient to even cool it down from a theoretical value of 740°C to the required 80°C. The corresponding compressor outlet temperature of approximately 190°C (Fig. 12) can be therefore handled by the humidification device. As a consequence, only a fraction of the water to be evaporated is used to control the cathode air temperature, while the other fraction might be heated up electrically or by heat transfer from the reformer and then mixed in form of vapour with the pre-humidified air. An interesting result of this evaluation is the curve of the turbine outlet temperature, which is an indicator of how much water will condense in the turbine exhaust gases. As can be seen in Fig. 12 the turbine outlet temperature remains at every altitude above 0°C without the risk of ice formation in the turbine section.

2.7 Operating Restrictions due to Aerodynamic Boundary Conditions

It will now be verified whether the required design cathode mass flow can be covered with the total air compressor without reaching aerodynamic constraints, such as surge or choke. The operation at altitude dependent ambient conditions and the requirement of a constant compressor outlet pressure and compressor mass flow reveals to be an advantage. In order to supply a constant cathode and thus compressor mass flow with increasing operating altitude, both the volume flow and the pressure ratio have to be increased simultaneously. These boundary operating conditions allow the operation close to the design flow and head coefficient (Eq. 3-13 and Eq. 3-14) of the compressor over a wide range of the operating altitude. According to these similarity parameters, the velocity diagram at the impeller inlet and the force conditions across the impeller are close to the design conditions, which points to an operation not only afar from the stated aerodynamic constraints but also at highest efficiency possible. This consideration is confirmed by the detailed analysis presented in Chapter 5, p.54, and makes the radial compressor a favourable compression technology for this application.

In order to illustrate the operating distance from the surge and choke line, a compressor map for a two-stage compressor is shown in Fig. 13. The straight line represents the constant cathode mass flow throughout the flight envelope matching the stack design point requirements at every altitude. The pressure ratio is plotted versus the reduced mass flow and shaft speed, which makes it possible to compare compressor performance mapped at different ambient conditions. These variables are defined by

$$\dot{m}_{red} = \dot{m}_{real} \cdot \frac{p_{t,ref}}{p_{amb}} \cdot \sqrt{\frac{T_{amb}}{T_{t,ref}}} \qquad \text{Eq. 2-7}$$

and

$$n_{red} = n_{real} \cdot \sqrt{\frac{T_{t,ref}}{T_{amb}}} \qquad \text{Eq. 2-8}$$

where $T_{t,ref}$ and $p_{t,ref}$ are standard conditions.

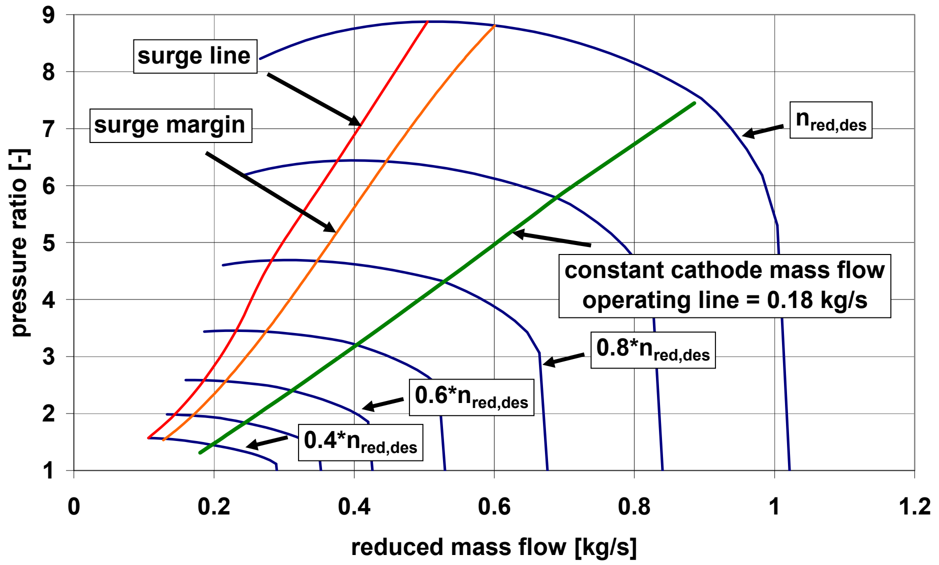

Fig. 13 Constant cathode pressure and mass flow operation in the reduced compressor map

Starting at the design operating altitude, the reduced mass flow and the pressure ratio are steadily decreasing, which illustrates the constant-volumetric-flow characteristic of the compressor. For system integration and the stack developer, on the other hand, this representation is not useful as solely the real mass flow is of importance. The compressor map has been therefore arranged in such a way that each constant speed line is recalculated with the corresponding ambient conditions. The result is shown in Fig. 14 and is unfamiliar to turbomachinery readers but depicts the operation afar from aerodynamic constraints and the possible mass flow variation at each altitude.

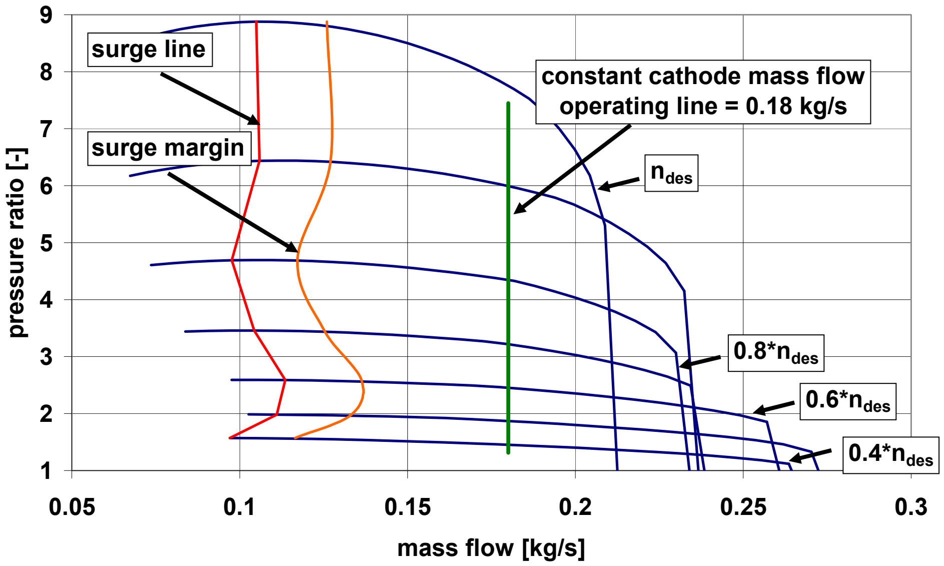

Fig. 14 Constant cathode pressure and mass flow operation in the rearranged compress. map

An improved representation is used in Chapter 5, p.54, where the interaction between turbomachinery design and operating range is addressed specifically.

2.8 Increasing Operational Flexibility by Advanced System Design

It is of major interest how operational flexibility is improved by conceptual means, which might be an extension or modification of the proposed arrangements. Here, operational flexibility is characterised by a wide cathode pressure and mass flow range and the ability to overcome transients in a quick and safe way.

2.8.1 Application of a Compressor Blow-off Valve

Decreasing the mass flow represents a critical scenario to the compressor moving the operating points towards surge and thus to critical system operation. The installation of a bleed valve at compressor outlet is a simple device to decrease the cathode mass flow but causes dissipation of the compressor work. This scenario cannot be recommended for long-term operation as the excess air does not provide benefit to any other component but this scenario may be considered for prototype demonstration. However, a bleed valve will be necessary even for a commercial system to serve as a robust anti-surge device e.g. during start-up or fast transients.

2.8.2 Application of Compressor Inlet Guide Vanes

The broadening of the compressor map towards lower and greater mass flows can be achieved by the application of inlet guide vanes (IGV). IGVs initiate a pre-swirl e.g. in direction of the impeller’s rotation reducing incidence losses and thus allowing operation at lower mass flows than without IGV. A pre-swirl against the rotation decreases the relative inlet velocity at the impeller inlet. The relative inlet velocity again dominates the choking characteristic of the compressor, which is shifted to higher mass flows. This allows off-design operation without additional dissipation and an efficient work transfer to the fluid. On the other hand, IGVs increase the weight and volume of the air supply system and, more importantly, raise system complexity. A malfunction of the IGVs can impose significant restrictions for overall performance or lead even to a system shut down which has to be taken into account during availability considerations. The potential to enlarge the compressor map by application of IGVs is remarkable and is illustrated in Fig. A-2, p.110. The position of 70° represents maximum pre-swirl in the direction of rotation. The model for the IGV is taken from Hagelstein, D. (2001). The mass flow is decreased by half at a guide vane position of 50° and increased by more than 30% at a guide vane position of -20°.

2.8.3 Application of a Post-combustor

The possible benefits of a post-combustor have been addressed in Section 2.5, p.15, as its use might avoid or minimise the electric power demand for compression. Temperature can be increased up to 1000 K (a typical temperature range for turbocharger turbines) by additional burning of kerosene in the post-combustor. This brings up a whole set of possible operating scenarios. Short duration kerosene injection may help to overcome too slow shaft speed transients during fast cathode fast mass increase. Continuous co-firing may help to support short-term high power output demands from the APU or to increase overall system efficiency at cruising altitude when the turbine section offers sufficient power output.

$$\eta_{co-firing} = \frac{\dot{m}_{exh} \cdot c_{p,exh} \cdot \eta_{is,turb} \cdot \left(1 - \pi^{\frac{1-\kappa}{\kappa}}\right) \cdot \left(T_{4,co-firing} - T_4\right)}{\dot{m}_{exh} \cdot c_{p,exh} \cdot \left(T_{4,co-firing} - T_4\right)} = \eta_{is,turb} \cdot \left(1 - \pi^{\frac{1-\kappa}{\kappa}}\right) \qquad \text{Eq. 2-9}$$

The additional output power of the turbine due to co-firing can be related to the kerosene amount necessary for increasing the temperature, which yields the thermodynamic efficiency of the co-firing. It can be roughly calculated by Eq. 2-9 and is solely a function of the turbine isentropic efficiency and the expansion ratio when neglecting changes in mass flow and gas properties during co-firing.

At cruising altitude, the efficiency of the co-firing process is approximately 25%, which is in the range of the overall system efficiency without co-firing. For operation at lower altitudes, the ratio increases and co-firing becomes disadvantageous from a system efficiency point of view but might remain an option as this operating period is relatively short. An increase in turbine efficiency, on the other hand, would enhance the system efficiency even without co-firing, which underlines the importance of a careful turbine design. Co-firing is a possible mean to overcome load peaks during transients at every altitude. It allows designing the stack output below the maximum peak load and thus decreasing the stack and gas processing reactor size representing the largest weight and volume fraction within the FC power module.

2.8.4 Cathode Pressure Strategy

An important potential for improving the operational flexibility is the choice of the cathode pressure which may be varied at each operating altitude to find optimum system operating conditions. To find the optimum system pressure as a function of altitude is part of the operating strategy and has a significant impact on turbomachinery design, stack performance, and mass flow range. Basically, it can be stated that the maximum mass flow is defined by the choking characteristic of the turbine at any operating altitude. An increase of the turbine inlet pressure causes therefore not only a higher turbine power output but also an extended mass flow to higher values. At the same time, the compressor power demand rises and the fuel cell stack output and efficiency increase due to the higher Nernst potential at the membrane shifting the entire power management to a new equilibrium. A cathode pressure increase will be limited by the aerodynamic compressor constraints such as surge, especially when the compressor mass flow is chosen to remain constant. Nevertheless, cathode pressure optimisation is an interesting option as it does not impose additional devices and thus does not increase the system weight and volume. Special attention will be therefore paid to the analysis of the cathode pressure in Chapter 5, p.54.

2.9 Concept Choice and Further Approach

For optimum air supply system for an in-flight PEM-FC, the design criteria system of low weight and volume, low system complexity, best controllability and least electric power consumption have been pursued. Radial compressors and turbines meet these crucial requirements and offer, through their integration into turbocharger architecture, a compact and proven technology. Based on simple assumptions for the compressor and turbine models, it has been shown that the air supply system is applicable for the entire envelope and requires moderate power support from the FC stack. Operation under extremely hot and humid ground ambient conditions is possible as the increasing vapour pressure leaves enough cooling margin. The aerodynamic characteristics of radial compressor maps inherently match the requirement of a constant cathode mass flow over the entire flight envelope.

Tab. 3 Decision matrix for the concept choice

requirement	**evaluation: 2=very good, 1= fair, 0=bad**		
	concept A	**concept B**	**concept C**
low system weight and volume	2	1	0
high availability	1	0	1
low power consumption	2	1	0
least number of devices	2	0	1
good controllability	0	1	2
based on state-of-the-art technology	0	1	2
sum	7	4	6

A decisions matrix (Tab. 3) is created to select the best concept following the most important design requirements of the air supply system. With an evaluation range from zero to two, denoting very poor to very good fulfilment of the requirement, respectively, concept A should be favoured, while closely followed by concept C.

Despite concept A seeming to achieve the stated requirements in a best way, it is believed that at the present development level the coupling of the reformer air compressor to the turbocharger shaft unnecessarily increases integration effort and burdens system dynamics and controls. Concept C resolves this problem without dropping too low in the decision matrix. It is therefore favoured for the subsequent analysis (see Fig. 7, p.14). As can be seen, the reformer air compressor is driven by a separate electric motor which imposes a power demand of approximately 5 kW throughout the entire envelope. This is reasonably low when compared to the design output of 80 kW from the fuel cell stack.

3 Radial Compressor Design and Optimisation

3.1 Design Strategy Considerations

Radial compressors have been chosen to be optimum for the combination with the in-flight PEM-FC. To the author's knowledge, radial compressors designed for or applied to this task do not exist at this point of time. Therefore, it is believed that a new radial compressor has to be developed or a similar, already existent, design has to be adapted to the present boundary conditions. This brings up the necessity of a radial compressor design procedure, which sets guidelines for a new design or allows the evaluation of the development gap for a successful integration, respectively. In this regard, two important questions arise:

- How has a radial compressor to be designed to fit the in-flight requirements?
- How can the design be modified to improve overall performance?

The design of radial compressors is a highly complex task comprising aero-dynamic, stress analysis and system integration issues based on experimental and operational experience. Various authors (Aungier, R. H. (2000), Eckert, B.; Schnell, E. (1980), Rautenberg, M. (1984), Balje, O.E. (1981), and Whitfield, A (1990)) propose strategies for the radial compressor design differing in application of empirical and semi-empirical correlations which are combined with basic aerodynamic laws. These different strategies may be called "philosophies" of design procedures as they are based on the authors' experience emphasising different aspects of loss mechanisms or algorithm logics as sufficiently accurate or effective.

In this work, a design algorithm has been developed to obtain important geometric relations of the impeller, the diffuser and the volute, which is also known as preliminary design. The geometry set allows the calculation of a complete performance map of the designed radial compressor and thus an evaluation in a subsequent steady-state and transient analysis. Based on these results, the design procedure can be adjusted to application specific operating targets, here the use with an in-flight PEM-FC.

Special attention has been paid to the impeller design which has been started from the basic relations published in Whitfield, A (1990). This strategy is favourable for the current work as it is based on the most general aerodynamic laws and non-dimensional similarity parameters followed by a one-dimensional meridian streamline approach. The streamline approach itself on the one hand offers sufficient accuracy for performance prediction and on the other hand requires only low calculation time when compared to Computational Fluid Design calculations. The design procedure is carried out with non-dimensional similarity parameters to obtain independency from geometry and to compare and evaluate aerodynamically similar conditions at the inlet and outlet of the designed section. The application of similarity parameters for the preliminary design of turbomachines is attractive due to its simplicity and independence of loss models. Arranged as one module, it can be combined with user-specified loss models or known efficiency values e.g. obtained from experimental data. The specification of only one geometric value or the mass flow is sufficient to translate the results of the non-dimensional design into a geometry setting and absolute velocity parameters, which are necessary for performance mapping.

A common objective of design with non-dimensional parameters is to transfer the optimised design of an existing turbomachine to another one. As in this work a completely new design is sought after, the newly obtained similarity parameters are used only to verify if the design results are within the specific radial compressor region of the Cordier-diagram. The Cordier diagram gives an overview of design parameters of state-of-the-art compressors with good performance.

In order to facilitate comprehension of the design strategy, the most important aerodynamic relations and non-dimensional parameters and their interdependencies shall be mentioned here. As special attention has been paid to the impeller design, the main inducer and discharge considerations are described before the overall compressor design procedure is presented.

3.2 Basic Aerodynamic Relationships and Non-dimensional Parameters

A radial compressor consists of the radial impeller, a diffuser, and a volute. An illustration of an impeller and the corresponding velocity diagrams is given in Fig. 15.

The important geometric characteristics at impeller inlet are the blade angles at the hub β_{1H} and shroud β_{1S}, the absolute velocity angle at inlet α_1, the blade angle at outlet $\beta_{2,b}$, and the absolute velocity angle α_2. Further geometric relations are the radius ratio

$$\nu = \frac{D_{1,S}}{D_2} \qquad \text{Eq. 3-1}$$

and the hub to shroud ratio

$$\nu_H = \frac{D_{1,H}}{D_{1,S}} \qquad \text{Eq. 3-2}$$

In this analysis, no inlet guide vanes are applied, therefore α_1 remains constant at 90°.

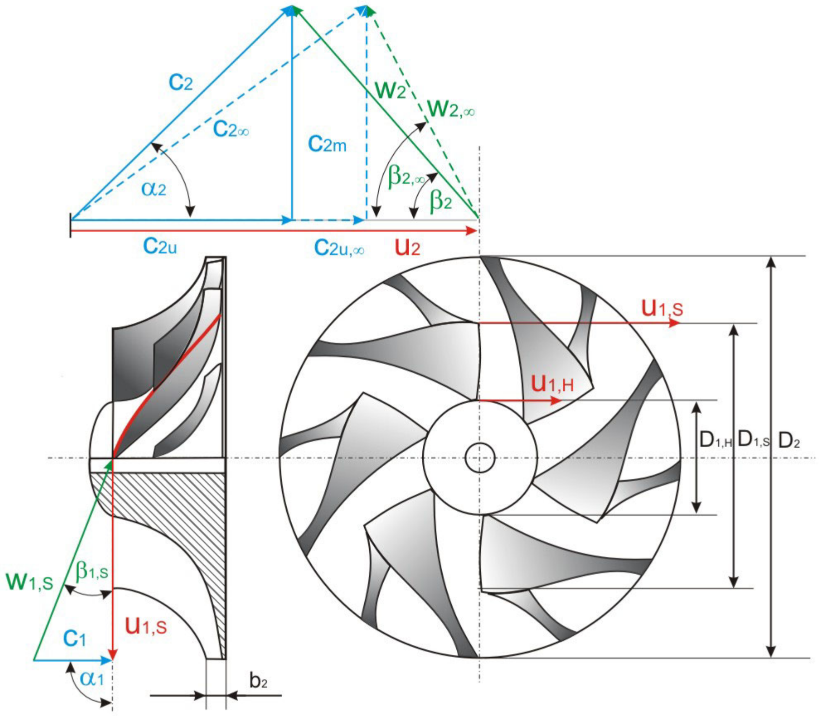
C2
C2∞
α2
C2m
W2
W2,∞
β2,∞
β2
C2u
C2u,∞
u2
u1,S
u1,H
D1,H
D1,S
D2
W1,S
β1,S
C1
u1,S
α1
b2

Fig. 15 Radial impeller geometries and velocity diagrams

Deducing from the velocity vectors and the relationship

$$\vec{c} = \vec{u} + \vec{w}, \tag{Eq. 3-3}$$

the characteristic velocity diagram can be drawn for the impeller inlet and outlet illustrating the specific work transfer from the impeller to the fluid (Fig. 16).

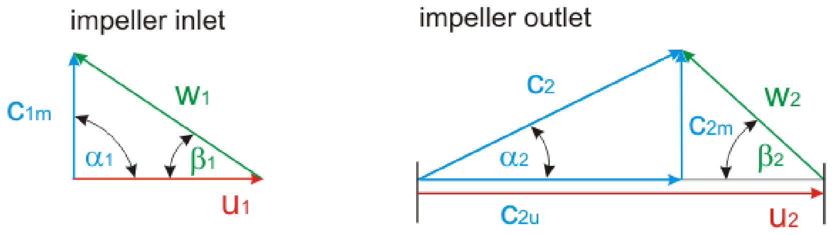
impeller inlet
C1m
W1
α1
β1
u1
impeller outlet
C2
W2
C2m
α2
β2
C2u
u2

Fig. 16 Velocity diagrams at the inlet and outlet of the impeller

All velocity diagrams can be transformed into non-dimensional diagrams represented by Mach numbers which are calculated either with the static local temperature or the total temperature at impeller inlet following

$$Ma = \frac{c}{\sqrt{\kappa \cdot R \cdot T_{local}}} \tag{Eq. 3-4}$$

$$Ma = \frac{c}{\sqrt{\kappa \cdot R \cdot T_{impeller\,inlet,t}}} \qquad \text{Eq. 3-5}$$

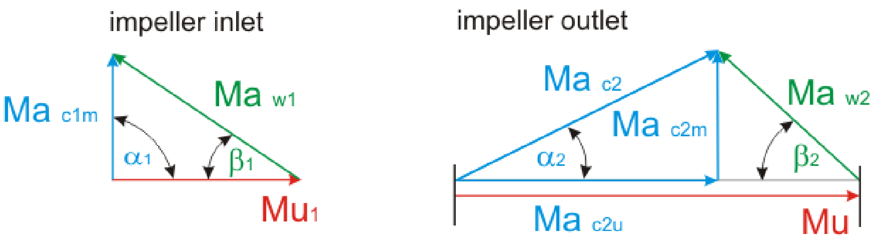

Fig. 17 Mach number diagrams at the inlet and outlet of the impeller

Unlike for absolute velocity diagrams, the calculation with Mach numbers offers a comparison of aerodynamically different states, which is favourable for a general compressor design (Fig. 17).

Additional non-dimensional dynamical characteristics can be defined, such as the slip factor

$$\mu = \frac{c_{2,u}}{c_{2b,u}}, \qquad \text{Eq. 3-6}$$

which shows the effect that the magnitude of tangential velocity is lower than the ideally attainable velocity, the work factor

$$\lambda = \frac{c_{2,u}}{u_2} = \frac{\mu}{1+\mu\frac{\tan\alpha_2}{\tan\beta_{2b}}}, \qquad \text{Eq. 3-7}$$

which demonstrates the ratio between the mechanical impeller work and the work transferred to the fluid, and the non-dimensional impeller speed

$$Mu = \frac{u_2}{\sqrt{\kappa R T_{1t}}}. \qquad \text{Eq. 3-8}$$

Core aerodynamic parameters of the impeller can be then expressed by the non-dimensional parameters such as the total temperature ratio

$$\frac{T_{2t}}{T_{1t}} = 1 + \frac{(\kappa-1)}{\kappa \cdot R \cdot T_{1t}} \cdot \left(u_2 \cdot c_{2,u} - u_1 \cdot c_{1,u}\right), \qquad \text{Eq. 3-9}$$

which gives the stagnation temperature ratio not only for the impeller but also for the entire compressor as the remaining adiabatic components such as the diffuser and the volute do not change the total temperature. The relation between the change of angular momentum of the fluid and the thermodynamic change of state of the fluid is well illustrated. When assuming a swirl-free inlet flow and applying Eq. 3-7 and Eq. 3-8, the total temperature ratio can be expressed by

$$\frac{T_{2t}}{T_{1t}} = 1 + \left(\kappa - 1\right) \cdot \lambda \cdot Mu^2 \qquad \text{Eq. 3-10}$$

demonstrating the dynamical conditions at the impeller. When applying the definition of the isentropic efficiency

$$\eta_{\mathrm{is}} = \frac{\left(\frac{\mathrm{p}_{5,\mathrm{t}}}{\mathrm{p}_{1,\mathrm{t}}}\right)^{\frac{\kappa-1}{\kappa}} - 1}{\frac{\mathrm{T}_{5,\mathrm{t}}}{\mathrm{T}_{1,\mathrm{t}}} - 1} \qquad \text{Eq. 3-11}$$

the compressor total pressure ratio can then be expressed by

$$\frac{p_{5t}}{p_{1t}} = \left(1 + \left(\kappa - 1\right) \cdot \eta_{is} \cdot \lambda \cdot Mu^2\right)^{\frac{\kappa}{\kappa-1}} . \qquad \text{Eq. 3-12}$$

The total pressure ratio is not only dependent on fluid properties represented by the heat ratio but also the isentropic efficiency of the compressor. A value for the isentropic efficiency can be obtained from aerodynamically similar machines or calculated from loss models.

Finally, two important parameters from similarity theory can be defined, which are important for the comparison of compressors, the flow and head coefficient. They are defined by

$$\Phi = \frac{4 \cdot \dot{m}}{\rho_1 \cdot u_2 \cdot \pi \cdot D_2^2} \qquad \text{Eq. 3-13}$$

and

$$\Psi = \frac{2 \cdot \Delta h_{1,2tot}}{u_2^2} = \frac{2}{u_2^2} \cdot \frac{\kappa \cdot R \cdot T_1}{\left(\kappa - 1\right)} \cdot \left(\left(\frac{p_{3,tot}}{p_{1,tot}}\right)^{\frac{\kappa-1}{\kappa}} - 1 \right), \qquad \text{Eq. 3-14}$$

respectively.

3.3 Inducer Design

Ferguson T.B. (1963) gives an overview of research work considering the optimum incidence angle. Ferguson T.B. (1963) reports optimum performance at zero incidence, when blockage is not considered, which will be applied here. Japikse, D. (1996) reports that a negative incidence angle for the design operating point increases operational range, which is an option to be defined in the algorithm for further analysis.

For the inducer design, minimisation of the relative Mach number at the impeller tip is considered to be essential for optimum overall performance. Low relative Mach number at impeller inlet is an indicator for low blade incidence losses at inducer inlet, which again is a dominating dissipation source during work transfer. Furthermore, it is desirable to decrease the relative Mach number at the impeller inlet as the stable operating range between choke and stall increases significantly (Rodgers, C. (1964)).

It has to be mentioned that if single-stage compression is favoured, transonic inducer design becomes necessary. For this, shock models at the impeller tip and the splitter blades as well as friction losses for the transonic flow at the inducer tip have to be introduced in order to complete the evaluation of the single-stage concept. This goes beyond the scope of this work and is not considered here.

The main design parameters are the hub and shroud radii and blade angles. At a fixed mass flow, impeller speed and hub diameter, which is often defined by the torque transmission, the shroud diameter can be varied in order to minimise the relative Mach number at the impeller shroud. The mean inlet velocity is decreased with an increased shroud diameter and thus cross sectional area at the impeller inlet, given by

$$c_{1,S} = \dot{m} \cdot \frac{R \cdot T_1}{p_1 \cdot} \frac{1}{\frac{\pi}{4} \cdot \left(D_{1,S}^2 - D_{1,H}^2 \right)} \quad \text{Eq. 3-15}$$

Simultaneously, the circumferential velocity at the shroud is increasing by the relation

$$u_{1,S} = \omega \cdot \frac{D_{1,S}}{2} \quad \text{Eq. 3-16}$$

The relative velocity though can be expressed by

$$w_{1,S} = \sqrt{u_{1,S}^2 + c_{1,S}^2} \quad \text{Eq. 3-17}$$

Consequently, an optimum exists for the relative inlet velocity which is calculated by an iterative loop. This procedure fixes then the blade angles at the hub and shroud.

With the total pressure ratio, the outlet blade angles, and the velocity angles as input to the procedure, the shaft speed is iterated in an outer loop to find the overall optimum shaft speed at a minimum inlet Mach number.

In order to maintain design algorithms and applied technology at a reasonable level, only sub-sonic modelling and thus inducer design is applied in this work. An increase in the tip Mach number opens a wider design range but imposes also further losses due to shock waves decreasing the overall isentropic efficiency. Once unity is reached, the maximum relative Mach number is held constant as a constraint during further parameter variations.

The inlet blade angle at the shroud remains between 30° and 34°, which is in the range of state-of-the-art inducer designs.

3.4 Discharge Design

The following section aims at the illustration of the impact of major geometric design parameters on aerodynamic design parameters and vice versa. It shall also give basis to a thorough comprehension of the parameter interaction during compressor design. It finally allows to evaluate performance and to reveal operational restrictions due to the in-flight specific boundary conditions. Important aerodynamic parameters are:

- The magnitude and direction of the absolute discharge Mach vector
- The magnitude of the relative inlet Mach number
- The diffusion ratio of the impeller deH
- The specific speed Mu

The outlet Mach vector defines to a great portion the loading of the diffuser system downstream of the impeller. High meridional velocities lead to friction losses and to shock losses around the leading edges of the diffuser and, if used, the diffuser vanes. A too low discharge angle imposes a long circumferential path through the vaneless diffuser causing not only additional friction but may initiate stall and flow reversals to the point of violent surge. Although, the relative inlet Mach number has a strong impact on the inducer section, it also shows important interaction with the diffusion ratio, which again is linked directly to outlet Mach number, e.g. small diffusion ratios may lead to an unstable operation due to increasing boundary layers initialising backflow in the impeller and possibly lead to surge. The specific speed gives important information about the non-dimensional impeller loading from a thermodynamic and mechanical point of view.

The major geometric parameters at the impeller discharge are (see Fig. 15, p.26):

- The blade angle β_{2b}
- The discharge angle α_2
- The diameter D_2 (radius ratio ν)
- The blade height b_2 (non-dimensional blade height b_2/r_2)

A large outlet diameter (or small radius ratio) has a strong impact on the physical stresses and defines through the impeller channel lengths strongly the friction surface and thus the impeller efficiency. Small blade height, for example, interacts strongly with high inlet Mach numbers. When loss models are applied for the prediction of the section performance, these parameters cannot be set independently. Some have partially strong interdependencies with each other while others simply result from other parameters, as in the case of the blade height.

It is not possible and not meaningful to define only geometric parameters to calculate and assess the aerodynamic performance, or vice versa. A design strategy which follows design targets and specifications is rather based on a suitable choice of setting parameters from both categories. In the present case, input values to the procedure are the pressure ratio, the outlet angles, the radius ratio and the specific speed. In order to demonstrate their influence in a systematic way, these values are analysed independently while the efficiency parameter is held constant. The results are presented in detail in Sections B.1 to B.4, p.111.

Considering the preceding relations, it can be summarised that for the here demanded high pressure ratios the optimum geometry settings may be found at low discharge blade angles, low radius ratios and low discharge angles. Diffusion ratio and the relative inlet Mach number are to be kept low. On the other hand, a low discharge blade angle will be limited by the upper stated stress constraints, while a low radius ratio leads to a great outlet diameter. This again has a detrimental impact on the transient behaviour and, more importantly, the isentropic efficiency of the compressor. A low discharge flow angle will also impose a great loading on the subsequent diffuser, decrease the diffuser efficiency and shift the operating conditions nearer to the stability limits due to increased diffuser surface friction. This represents a typical optimisation problem which will be addressed below.

3.5 Diffuser and Volute Design

The fluid discharges from the impeller at high velocity. Therefore, it is essential to convert the kinetic energy efficiently into static pressure. The diffuser system of a centrifugal compressor is usually constructed of either a vaneless diffuser or a combination of a vaneless diffuser followed by a vaned diffuser. The vaneless diffuser is often applied due to its technical simplicity and inexpensive construction and, in the present application of great importance, due to its broad operating range.

A vaned diffuser has the clear advantage of achieving very high pressure ratios which would be favourable when considering only one stage for the total air compression. The fixed diffuser geometry, however, entails a narrow operating range at high mass flows. Off-design compressor operation results in a significant change of the discharge angle, which causes incidences and thus losses at the vane edges. After a narrow operating range at high pressure, the compressor performance collapses within a small range of further mass flow increase. One possibility to avoid this effect is the application of variable vane geometry where the angle of the diffuser blades can be adapted to the optimum discharge conditions. It represents an increase in technical complexity which is believed to be a too great of a step for the demanded prototype application. Considering this circumstance, solely vaneless diffusers are applied in the present work.

The vaneless diffuser consists of two parallel or slightly converging walls or a combination of those. A simple geometric relation is the diffuser radius ratio,

$$\nu_{\mathrm{Diff}} = \frac{D_3}{D_2}, \qquad \text{Eq. 3-18}$$

where the diffuser outlet diameter is divided by the inlet diameter. The inlet diameter is not equal to the impeller outlet diameter as a small gap is often implemented for flow stability reasons. The diffuser radius ratio will be set to 1.6 for the present work, which is state-of-the-art for a broad number of radial compressor applications.

For the design procedure, a simple, but for preliminary design suitable, diffuser stability criterion will be applied from Aungier, R. H. (2000). It accounts for the possibility of rotating stall on-set as a precursor of surge. Independent from the diffuser width to outlet diameter ratio, the diffuser design will consider only discharge flow angles greater than 14° to avoid stability restrictions at design point operation.

The volute situated downstream of the diffuser collects the air flow into a single pipe for delivery to the cathode and gas processing path. At design point operation, the volute is expected to have no impact on pressure rise or drop, while it is often observed that it acts as a diffuser at low mass flows and as a vane at high mass flows compared to the design point. For this work, the external volute design has been applied, as this represents the state-of-the-art for radial compressors and contributes to a maximum overall operating range. As the pressure recovery is expected to be near zero for the volute, the outer diameter of the volute is adapted in order to meet this criterion. Further attention has been paid to the cone exit which is often reported to be a transition piece relevant for choking of the mass flow and thus a possible constraint for operation at high mass flows. The diameters at the cone entry and exit have therefore been adapted to result in low Mach numbers, which is also favourable for the piping velocities and the associated pressure losses.

3.6 Design Procedure

Based on the design topography presented in Section 3.4, p.30, a design procedure has been developed to obtain the thorough geometry setting necessary for the subsequent performance map calculation. The design boundary conditions in the present work can be summarised as follows:

- Only backswept blades $\beta_{2,b}$<90° are applied to keep the diffusion ratio low
- The absolute discharge angle α_2 is greater than 14° to ensure diffuser flow stability
- The relative Mach number at shroud inlet $Ma_{1,w,S}$ is lower than unity to ensure subsonic inducer design
- The diffusion ratio is greater than 0.62 to ensure impeller flow stability
- The optimum specific speed is calculated by minimisation of the relative Mach number $Ma_{1,w}$ at impeller inlet

The performance targets of the compression device can be summarised as follows

Tab. 4 Performance targets of the compression system

parameter	value	unit
total pressure ratio, π_{tot}	7.5	-
mass flow, m	0.18	kg/s
ambient pressure, p_{amb}	0.179	bar
ambient temperature, T_{amb}	216.54	K

From the set of input and output variables, the general formulation of the algorithm can be stated as

$$\left(vel.\,triangles, geom.\,relations\right) = f\left(\nu,\nu_H,\alpha_1,\alpha_2,\beta_1,\beta_{2b},\eta_{is,imp},\eta_{is},\dot{m}_{red},\pi_{tot},n_{red}\right), \qquad \text{Eq. 3-19}$$

of which the most important input variables are the reduced mass flow, the pressure ratio, and the reduced speed.

In order to avoid the input of the isentropic efficiencies for the impeller and overall performance by the designer, an aerodynamic model has been combined with the design programme to create a consistent data set between the geometric design and the design point performance calculation. The loss model is based on detailed correlations of loss mechanisms for each section of the compressor. A detailed overview and discussion of the models is given in Chapter 4, p.43. By the combination of the design programme and the loss models, the number of input variables is reduced by the efficiency values. The output variables of the design programme serve as input to the loss model and vice versa. This will be continued in an iterative calculation until convergence is reached. As these loss models are also applied for the subsequent performance calculation, a consistent set of values is passed from the design step to the performance calculation step.

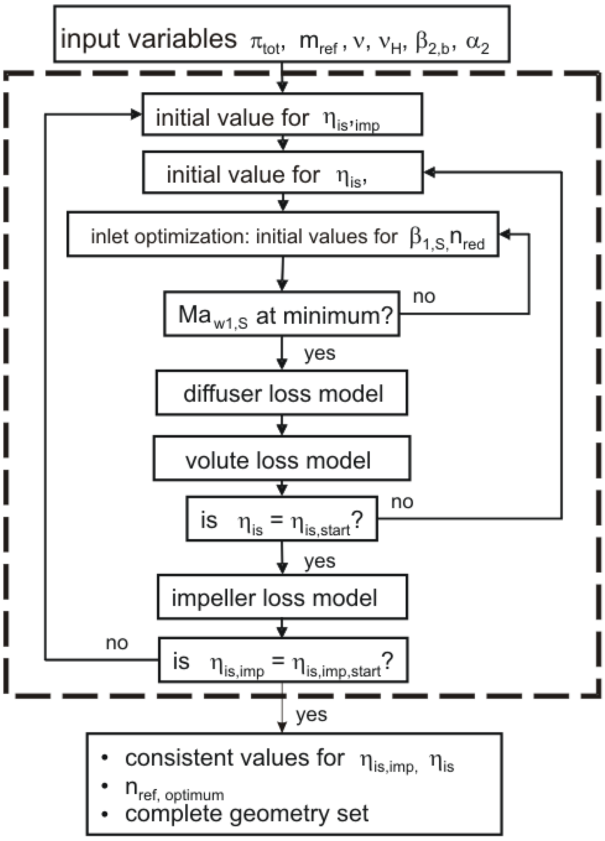
input variables π_{tot}, m_{ref}, ν, ν_H, $\beta_{2,b}$, α_2
initial value for $\eta_{is,imp}$
initial value for η_{is},
inlet optimization: initial values for $\beta_{1,S}$, n_{red}
$Ma_{w1,S}$ at minimum?
no
yes
diffuser loss model
volute loss model
is $\eta_{is} = \eta_{is,start}$?
no
yes
impeller loss model
no
is $\eta_{is,imp} = \eta_{is,imp,start}$?
yes
• consistent values for $\eta_{is,imp}$, η_{is}
• $n_{ref, optimum}$
• complete geometry set

Fig. 18 Design procedure for the single-stage radial compressor

In the design procedure, the shaft speed is calculated by a minimisation of the relative Mach number at the impeller shroud minimising the dominant incidence and friction losses in the inducer section as explained in Section 3.3, p.29. The overall isentropic efficiency is then iterated applying the diffuser and volute models. Finally, the impeller isentropic efficiency is calculated with the impeller loss model until predefined convergence criteria are reached. The nesting of the overall isentropic efficiency into the impeller efficiency loop seems to be not intuitive but achieves quick and stable convergence.

For the demanded pressure ratio of 7.5, a single-stage concept imposes the usage of a vaned diffuser or trans- or supersonic impeller design. Both the vaned diffuser and the transonic impeller require a more sophisticated design procedure. Technology and design requirements can be lowered significantly with a two-stage compressor concept applying vaneless diffusers in each stage. This might increase weight and volume but be outweighed by the broader operating range and the higher reliability.

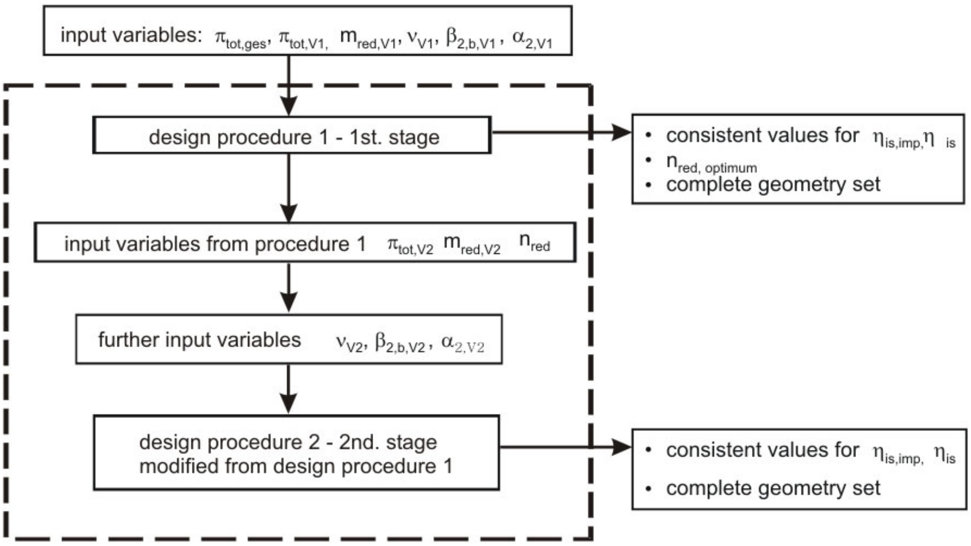
input variables: $\pi_{tot,ges}$, $\pi_{tot,V1}$, $m_{red,V1}$, ν_{V1}, $\beta_{2,b,V1}$, $\alpha_{2,V1}$
design procedure 1 - 1st. stage
consistent values for $\eta_{is,imp}$, η_{is}
$n_{red, optimum}$
complete geometry set
input variables from procedure 1 $\pi_{tot,V2}$ $m_{red,V2}$ n_{red}
further input variables ν_{V2}, $\beta_{2,b,V2}$, $\alpha_{2,V2}$
design procedure 2 - 2nd. stage modified from design procedure 1
consistent values for $\eta_{is,imp}$, η_{is}
complete geometry set

Fig. 19 Design procedure for the two-stage radial compressor

The two-stage concept represents a good alternative for the prototype application. The design procedure is therefore extended to a two-stage compression, which is depicted in Fig. 19. For this purpose, the single-stage design procedure has been duplicated and then modified to handle differing inlet conditions caused by the first stage. Consequently, the number of input variables for the two-stage design procedure increases by further geometric boundary conditions.

3.7 Design Optimisation

3.7.1 Definition of Design Specifications

In order to cover the aforementioned system design requirements, it is fundamental that the turbomachinery design procedure follows pre-defined specifications.

- Maximum isentropic efficiency

The importance of maximum compressor efficiency (Eq. 3-11, p.28) has been already addressed and is demonstrated in Chapter 5, p.54. Therefore it is a primary criterion.

- Maximum diffusion ratio and minimum relative inlet Mach number

While a maximum diffusion ratio (Eq. B-6, p.115) extends the operating range to lower mass flows, the minimum relative inlet Mach number (Eq. 3-4, p.26) favours the opposite effect.

- Maximum power coefficient

The power coefficient is a good indicator for the compactness of turbomachines and is

$$W_{nd} = \frac{\dot{W}}{\rho_{t1} \cdot \pi \cdot r_2^2 \cdot a_{t1} \cdot a_{t1}^2} = \Phi \cdot \Psi \cdot Mu^3 \quad \text{Eq. 3-20}$$

- Minimum outlet diameter D_2, rotor mass m_{rotor}, and rotor moment of inertia J_{rotor}

The outlet diameter allows the evaluation of volume of the compressor and is inherently related to the rotor mass and the rotor moment of inertia. The calculation of these parameters is based on the assumption that the passage diameter along the hub camber line can be represented by a spline function. Low rotor moment of inertia can improve significantly transient response characteristics of the turbocharger and, consequently, the needed control action.

- Maximum mass flow range

The mass flow range defines to a great portion the load range of the entire FC-system. For the design speed, it can be defined by

$$\text{range} = \frac{\dot{m}_{choke} - \dot{m}_{surge}}{\dot{m}_{choke}}, \quad \text{Eq. 3-21}$$

and for the entire compressor map by

$$\text{range}_{mean} = \frac{\sum \text{range}_i}{n_{\text{available speed lines}}}. \quad \text{Eq. 3-22}$$

Following Eq. 3-19, p.33, the remaining parameters ν, $\beta_{2,b}$, and α_2 are left to be specified by the compressor designer and can be varied in meaningful intervals. The solution space is defined by the intervals given in Tab. 5.

Tab. 5 Solution space for the single-stage optimisation

parameter	lower limit	upper limit	unit
radius ratio, ν	0.45	0.7	-
discharge blade angle, β_{2b}	45	80	°
discharge angle, α_2	14	34	°

3.7.2 Optimisation Limits

The choice of these parameters has a significant impact on the aforementioned design targets. Applying the design algorithm described above, a parameter variation for the radius ratio is carried out and illustrated in Fig. 20 and Fig. 21 (continued Fig. B-6 to Fig. B-8, p.116). For one example of a single-stage compressor, an efficiency optimum exists at a radius ratio of 0.63 (Fig. 20). A maximum diffusion ratio or minimum relative inlet Mach number are obtained at a radius ratio of 0.55 (Fig. 20) while the highest power coefficient is found at a radius ratio of 0.75 (Fig. 21). This demonstrates well that the achievement of all design criteria is not possible and the design result represents always a compromise of counteracting tendencies.

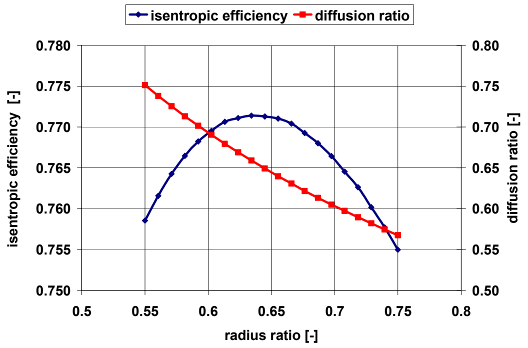

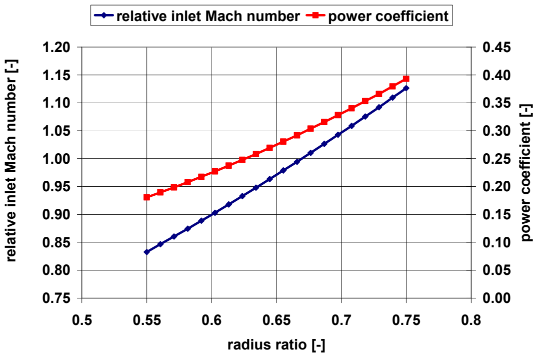

Fig. 20 Isentropic efficiency and diffusion ratio as a function of the radius ratio

Fig. 21 Relative inlet Mach number and power coefficient as a function of the radius ratio

It has to be mentioned that these results are only valid for a fixed outlet flow of α_2=20°and a blade angle of β_b=55°. When changing each of these parameters in the defined interval, respectively, the point of maximum efficiency (and all other parameters) moves to a new value, which is due to the strong non-linearity of the algorithm and the models.

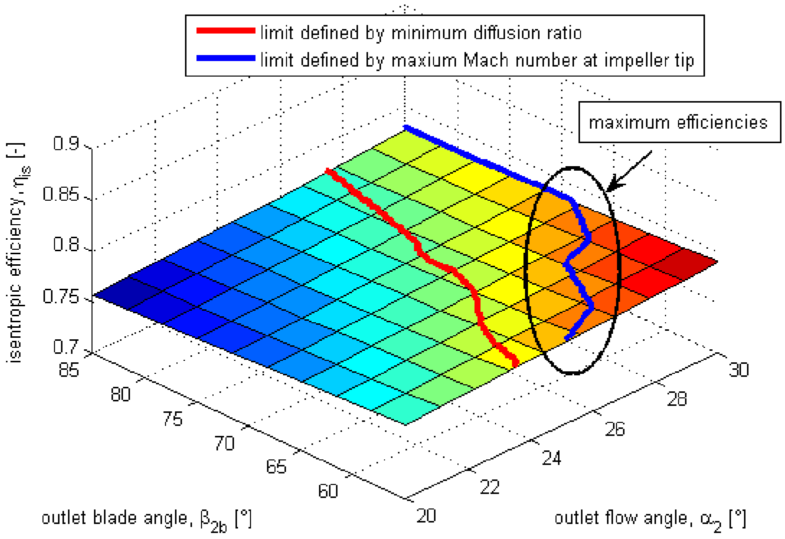

Fig. 22 Design plane for maximum efficiencies as a function of the impeller outlet flow angle and the impeller outlet blade angle

Following the design criterion of maximum efficiency for all permutations of the outlet flow and blade angles, a solution plane can be depicted. The common knowledge that maximum stage efficiency can be found at high outlet flow angles and small outlet blade angles is confirmed by the results shown in Fig. 22 and confirms the prediction capability of this procedure for a reliable preliminary design. The solution plane is constrained by the upper mentioned minimum diffusion ratio in the impeller and the maximum inlet relative Mach number at the impeller tip. Therefore, the maximum efficiency value is defined by an array of points along the maximum Mach number line shown in Fig. 22.

3.7.3 Decrease of Input Variables for the Design Procedure

It is still unsatisfactory, that the final design result is not definite. Due to the high number of free variables and their interdependencies, it appears furthermore complex and little illustrative to the designer to find the best compressor design especially when multiple design targets are pursued. The number of free parameters is therefore further decreased by embedding the design targets in an optimisation function offered by the Matlab software. The local maximum of the function is then found within the pre-defined solution space according to Tab. 5, p.36.

Thus, the input parameters for the compressor design are reduced to the known parameters, which are the mass flow, the pressure ratio, and the specifications of the design targets. The general expression of the algorithm then has the form

$$\left(vel.\,triangles, geom.rel., n_{ref,optimum}, \eta_{is,imp}, \eta_{is}, n_{red}\right) = f\left(\dot{m}_{red}, \pi_{tot}, design\ requirements\right) \qquad \text{Eq. 3-23}$$

The result is a set of 4-D matrices which are filtered and recalculated according to the turbomachinery design requirements. An illustration of one 4-D matrix is given in Fig. 23. The cluster of blue points represents the entire solution plane for the isentropic efficiency in the 4-D solution space which is convolved by the 3-D illustration.

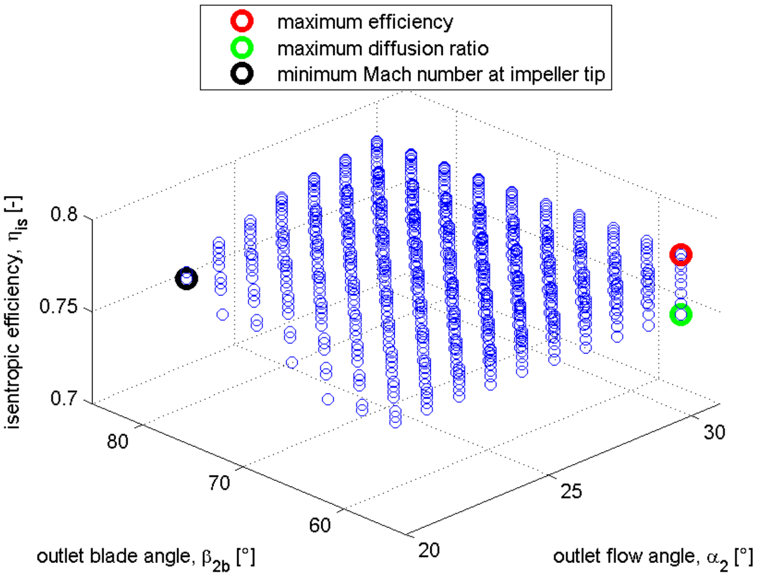

Fig. 23 4-D matrix visualisation of the optimum efficiency for the single-stage compressor design

What can be outlined in the figure is that the maximum compressor efficiency can be found at maximum outlet flow angle and minimum outlet blade angle indicated by the red circle. The green and black circles represent the corresponding efficiency values when the design procedure is optimised for highest diffusion ratio or lowest relative inlet Mach number, respectively. This means that different design targets lead to different aerodynamic parameter settings. For the two-shaft compression design, the matrices have a 7D form but are handled in the same mathematical way.

3.7.4 Multi-objective Optimisation

It is common in optimisation problems that one design has to cover several design criteria at the same time, which represents a multi-objective optimisation. The design optimisation has been extended within the Matlab software to allow a free number of design specifications and the possibility to weigh these design tasks according to the flight or PEM specific operating requirements.

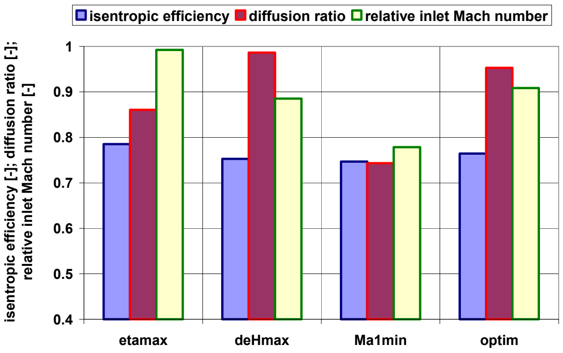

Fig. 24 Compressor characteristics for different design strategies

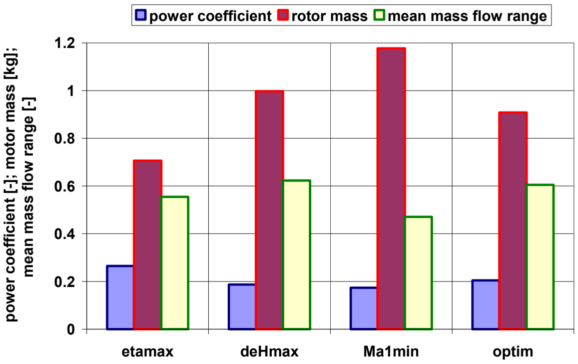

Fig. 25 Compressor characteristics for different design strategies

The capability of weighted compressor design optimisation with the developed algorithm is demonstrated in Fig. 24 and Fig. 25. In this example, isentropic efficiency and operating range are primary criteria, which have been achieved by a maximum diffusion ratio and minimum relative inlet Mach number. When optimisation is carried out only for one design goal, then at least one other goal does not achieve satisfying values. The last column in both figures shows that weighting of the design tasks by the same algebraic factor results in an overall gain for each parameter and therefore an overall optimum. The overall optimum has to be paid by a slightly decreased isentropic efficiency when compared to the efficiency oriented optimisation. It is well illustrated in Fig. 25 that coverage of every design task is not possible, which puts forth the compromise aspect of optimisation. The rotor mass is high even for the weighted optimisation while the power coefficient is comparatively low.

The algorithm offers the most important turbomachinery requirements to be achieved by one calculation step. Moreover, it is designed to allow quick introduction of new criteria and specific weighting which might be found during advanced analysis to be relevant for the successful turbomachinery integration.

3.7.5 Optimum Pressure Ratio Split for the Two-stage Compression

For the two-stage compression, the pressure ratio split between the two stages becomes an additional optimisation parameter. The design procedure is applied now for different pressure ratio splits while in each case optimum compressor efficiency is pursued. The results for the pressure ratio variation are given in Fig. 26.

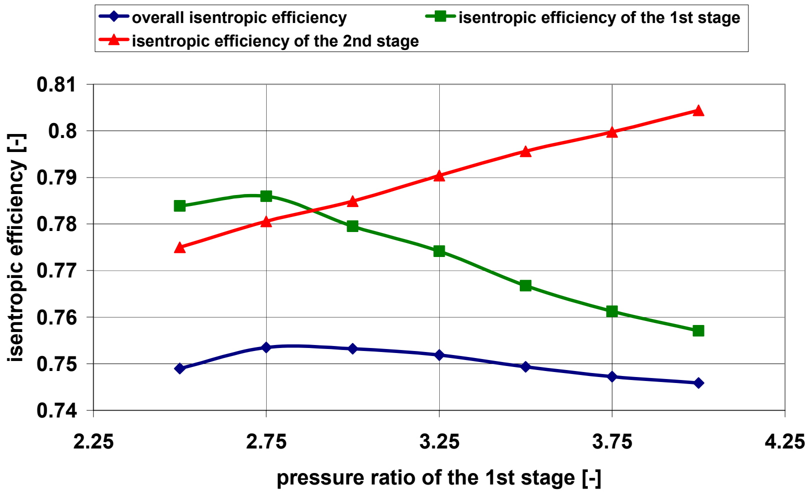

Fig. 26 Optimum pressure ratio split fort the two-stage compression

An optimum can be found for a compression ratio in the first stage of 2.75, which is a result from two counteracting tendencies. While the isentropic efficiency of the first stage has a flat maximum at 2.75, it decreases with further pressure ratio due to the increasing impeller diameter. Transferring the greater part of the fluid work, it cannot be compensated by the increasing efficiency of the second stage. Therefore, the design pressure ratio of the first stage is set to the found optimum value.

3.7.6 Comparison between the Single-stage and Two-stage Compression

As has been addressed in Section 2.3, p.12, the design choice between a single-stage or a two-stage compression has significant impact on turbomachinery design. The here developed design procedure is a tool for a final evaluation as to which concept is favourable for overall system performance.

For comparability reasons, the concepts are calculated with the same aerodynamic loss correlations. It has to be kept in mind, though, that Shaaban, S. (2004) validated these models for radial compressor with pressure ratios from 2 to 3.5. Therefore, the prediction quality for the isentropic efficiency has to be handled with care. The results of the aerodynamic performance, on the other hand, can be fully evaluated for the high-pressure ratio single-stage concept as the maximum relative Mach number at impeller inlet is unity, which eliminates transonic flow and shock waves in the inducer. This provides a basis for a comparison between the two compression concepts.

Again, the overall isentropic efficiency is chosen as optimisation criterion. The design results are shown in Tab. B-1, p.118. The detailed set of geometric parameters is given in Tab. B-2, p.118. It has been observed that optimum efficiency is obtained in both cases, when the maximum Mach number at the inlet of the first compressor is reached.

For the single-stage compression, it can be stated that the radius ratio is very low resulting in a great outlet diameter of the impeller and consequently of the entire compressor. The long flow channel of the impeller provides a large surface for friction and lowers the impeller and overall isentropic efficiency significantly, which qualitatively confirms the validity of the impeller model. An efficiency drop of approximately 7 percentage points has to be accepted when choosing the single-stage concept. Additionally, the mass flow range is significantly decreased at design speed due to the lower diffusion ratio.

A graphical comparison between the single-stage and two-stage compression can be carried out with the illustration given in Fig. 27. The constant speed lines of the single-stage and two-stage compressor are indicated by the red and blue curves, respectively.

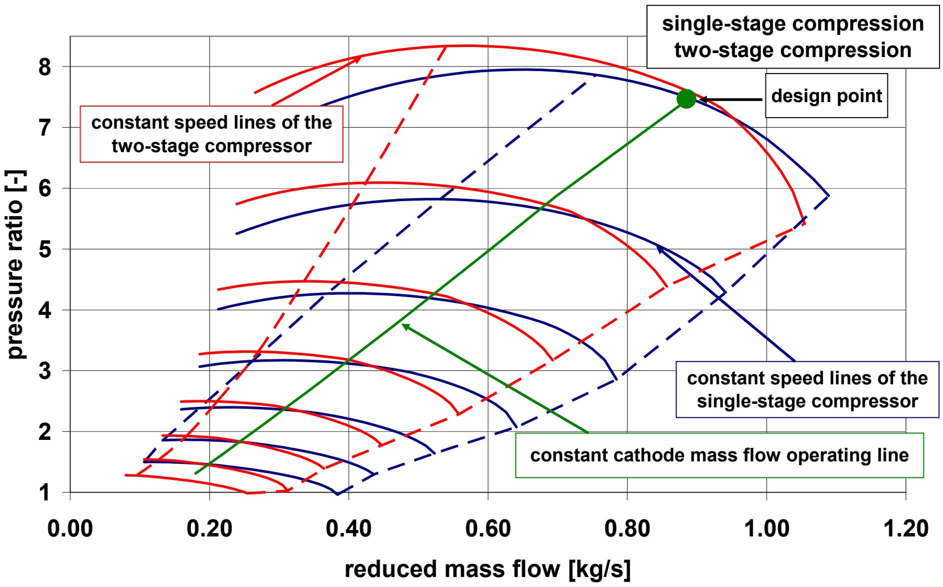

Fig. 27 Comparison between the single-stage and the two-stage compressor maps

It is important to state that both compression concepts are capable of covering the demanded operating line, defined by a constant cathode inlet pressure and cathode mass flow throughout the envelope. Moreover, the operating line for the constant cathode mass flow is close to or parallel to the peak of the lines of constant shaft speed, pointing at a high compressor isentropic and therefore overall air supply efficiency. Additional devices such as inlet guide vanes or a vaned diffuser are not necessary for the fulfilment of the design requirements but remain future options for improving operational flexibility.

Regarding the mass flow range of the two-stage compression, it can be observed for the design and intermediate shaft speeds (and thus operating altitudes) that the operating range is greater for mass flows left of the operating line. This can be explained by the fact that the total pressure increase is split into steps which moves the diffusion ratio of the design point in the first stage to higher values when compared to the single-stage compression (see Tab. B-1, p.118) and thus the surge line to lower mass flows. The operating range at intermediate and low shaft speeds to the right of the operating line, however, is lower when compared with the single-stage compressor. This circumstance can be explained with the greater volute for the single-stage compressor while the design mass flow is kept constant. With the volute representing the most important section for the choke characteristic, it can be deduced that the increased cross-sectional area reduces the aerodynamic losses in the volute and allows therefore a wider range to higher mass flows. This explains also why the mean operating range values shown in Tab. B-1, p.118, are almost identical for both concepts. An option to increase the mass flow range also at design speed is to further increase the cross-sectional area of the volute, which increases, on the other hand, the weight and the volume of the single-stage concept.

It is now left to the designer’s choice, whether isentropic efficiency and thus power demand or mass flow range is considered to be more important for overall performance. The single-stage concept, surely, is attractive due to its compact design and its closeness to state-of-the-art turbocharger architecture. Due to the remarkable increase in efficiency, the two-stage compression is favoured in this work and applied in the subsequent analysis.

4 Process Modelling

4.1 Radial Compressor

The radial compressor requires a complex modelling approach due to a high number of aerodynamic phenomena occurring on the compression path. The models for impeller and volute are taken from Shaaban, S. (2004), while the diffuser model is derived from Traupel W. (1962). The impeller model accounts for incidence, friction, disk friction, diffusion, passage, clearance, and blade loading losses. The diffuser is based on the conservation of mass, energy and momentum. The volute model accounts for friction, exit cone, and diffusion losses as well as loss of meridian velocity. Shaaban, S. (2004) developed this model as a reliable program for computing off-design conditions and validated it with experimental data obtained from a wide range of turbocharger compressors differing in flow and head coefficient. The model results agree well with the investigated radial compressors and offer a good means of extrapolation to low shaft speeds.

4.1.1 Slip Factor

The calculation of the tangential component of velocity at impeller discharge has been subject of extensive study. The objective is to find a reasonably simple method to calculate the mean tangential component of velocity in order to allow accurate calculations of the pressure ratio and thus the demanded power input to the compressor.

The slip factor accounts for the reduction in the anticipated swirl velocity at the impeller outlet. The difference between the actual and the ideal velocity diagram at the impeller outlet are shown in Fig. 15, p.26. In an ideal velocity diagram, the relative flow coincides with the blade angle. In practice, the flow cannot be perfectly guided by a finite number of blades. As the magnitude of the tangential component of velocity is decreased, it leads to a decreased pressure ratio as can be seen from Eq. 3-9 and Eq. 3-12, p.28. A general definition of the slip factor is

$$\mu = \frac{c_{2,u}}{c_{2b,u}} = \frac{c_{2b,u} - c_{slip}}{c_{2b,u}} = 1 - \frac{c_{slip}}{c_{2b,u}} . \qquad \text{Eq. 4-1}$$

The classical explanation for the slip phenomenon uses the concept of a relative eddy in the impeller passage. As the flow into the impeller is usually irrotational and a frictionless fluid remains irrotational, the flow at the outlet must rotate with an angular velocity opposite to that of the impeller. The slip velocity can be then expressed by

$$c_{slip} = r_{eddy} \cdot \omega \quad . \qquad \text{Eq. 4-2}$$

The eddy radius can be formulated for backswept blades accounting for flow separation and aerodynamic blockage in the impeller outlet area by

$$r_{eddy} = \frac{\pi \cdot D_2}{2 \cdot z} \cdot \sin \beta_{2b} \cdot F_{eddy} \quad . \qquad \text{Eq. 4-3}$$

The empirical coefficient F_{eddy} accounts for the effect of the geometrical and operating conditions of the impeller on the eddy radius. The final expression for the slip factor is

$$\mu = 1 - \frac{u_2}{c_{2b,u}} \cdot \frac{\pi}{z} \cdot \sin \beta_{2b} \cdot F_{eddy} \quad . \qquad \text{Eq. 4-4}$$

A good comparison and assessment of different slip correlations is given in Shaaban, S. (2004). A simple and often used correlation for the slip factor was presented by Stanitz, J.D. (1952) as

$$\mu = 1 - \frac{0.63 \cdot \pi}{z} \quad , \qquad \text{Eq. 4-5}$$

where the number of blades is accounted in a radially bladed impeller and Wiesner, F.J. (1967)

$$\mu = 1 - \frac{\sqrt{\sin \beta_{2b}}}{z^{0.7}} \quad , \qquad \text{Eq. 4-6}$$

who adds the effect of outlet blade angle on the slip and a correction factor dependent on the radius ratio. In view of the complex flow mechanisms within and behind the impeller, Balje, O.E. (1981) reports that the assumption of Wiesner appears to be a highly simplifying assumption. A complex but more accurate correlation for the eddy correction in Eq. 14 is proposed by Shaaban, S. (2004) and is validated for three different compressors with vaneless diffusers with a very good accuracy. The correlation accounts for the diffusion ratio, the radius ratio, the Reynolds number, the passage camber due to backswept blades, and the effect of fluid inertia occurring at small blade angles and high mass flows. Due to the strongly non-linear character of the correlation, Shaaban, S. (2004) recommends a simplification, which results in a slightly lower accuracy than the complex expression but offers a better slip factor prediction than the upper stated correlations:

$$\mu = 1 - \frac{u_2}{c_{2b,u}} \cdot \frac{\pi}{z} \cdot \sin \beta_{2b} \cdot 0.76 \qquad \text{Eq. 4-7}$$

A value of 0.76 for the eddy radius allows an accuracy of 5% deviation in the measured slip factor and is therefore used in the design algorithm.

4.1.2 Aerodynamic Loss Models

Once the total outlet temperature can be calculated with the corrected circumferential velocity according to Eq. 3-10, p.28, the total impeller outlet pressure can be calculated with Eq. 3-12, p.28, and the impeller loss coefficient which is defined as

$$\xi_{imp} = \frac{c_{p,air} \cdot \left(T_{2t,ad} - T_{2t,is}\right)}{u_2^2} \quad \text{Eq. 4-8}$$

The total impeller loss coefficient can be then calculated as follows

$$\xi_{imp} = \frac{\sum W_i}{u_2^2} \quad \text{Eq. 4-9}$$

The empirical coefficients are obtained from a minimisation procedure based on experimental data. A description of the losses is given in Section C.1, p.119. A thorough discussion about the loss model and its prediction quality is given by Shaaban, S. (2004).

The diffuser model is based on Traupel W. (1962) and is valid for vaneless diffusers, where it is assumed that losses occur due to fluid friction and energy dissipation. In order to calculate the outlet conditions the conservation of mass, energy and angular momentum is applied. The description of the applied equations is given in Section C.2, p.120. In the volute, friction as well as exit cone, diffusion losses and dissipation of meridional velocity are considered which are described in further detail in Section C.3, p.121.

4.2 Radial Turbine

The turbine mass flow is modelled by an expansion through a nozzle with an effective total-to-static pressure ratio taking into account the centrifugal force on the turbine mass flow as it is also suggested by Whitfield, A (1990) or Aungier, R. H. (2000). The effective pressure ratio is reduced by the radial outward pressure caused by the rotating turbine channel. The effective pressure ratio is then

$$\pi_{6t8s,eff} = \frac{p_{6t} - 0.5 \cdot \rho_6 \cdot \left(r_{rot} \cdot \omega\right)^2}{p_8} \quad \text{Eq. 4-10}$$

For low design shaft speeds, the influence of the centrifugal forces is neglected. The mass flow rate can be then expressed as

$$\dot{m}_t = c_{d,T} \cdot A_T \cdot \frac{p_{6t,eff}}{\sqrt{R_{exh} \cdot T_{6,t}}} \cdot \Phi_{T,eff} \quad , \qquad \text{Eq. 4-11}$$

The turbine discharge coefficient, $c_{d,T}$, is dependent on the inlet guide vane position and the Reynolds number. The flow coefficient $\Phi_{T,eff,}$ such as the calculation of the isentropic efficiency are outlined in Section C.4, p.123.

4.3 Pressure Loss

For the off-design analysis simple pressure loss models have been used. For the humidifier and the post-combustor a quadratic correlation has been applied with

$$\Delta p_{unit} = K_{\Delta p,unit,design} \cdot \dot{V}_{unit}^2 \qquad \text{Eq. 4-12}$$

while for the cathode a linear pressure characteristic is assumed

$$\Delta p_{cathode} = K_{\Delta p,cathode,design} \cdot \dot{V}_{cathode} \quad . \qquad \text{Eq. 4-13}$$

The constants are obtained from design conditions given in Tab. A-1, p.109. It has been found that the pressure losses across the air path are very sensitive parameters for the air mass flow operating range. Pressure loss optimisation should be therefore addressed at an early point of development. For a demonstrator plant, these values may be even optimistic, especially for the cathode section.

4.4 Further Components

As mentioned above, the reformer, the humidifier, and the PEM are described by simple thermodynamic steady-state models accounting for the gas composition at the inlet and stoichiometric conditions within the unit at the desired operating point. Input parameters are the relative humidity for the humidifier and the power output and current density for the stack.

The dynamic models for the humidifier, the reformer and the stack are provided by DLR Stuttgart. The humidifier is modelled following Neubrand, W. (1999) and Detallante, V. (2002). A description of the reformer is given by Lenz, B. (2005) and Lattner, J. R. (2004). The PEM stack model is applied from Bernardi, D. M. (1992), Riekmann, C. (1997), Siebke, A. (2003), and Wöhr, M. (1999).

The post-combustor is modelled according to the first law of thermodynamics and is assumed to operate ideally. It allows sequential burning of the cathode off-gases and additional kerosene which can be injected for boosting the turbine inlet temperature during fast transients. In a first step, the burning of the anode off-gases and the corresponding temperature is calculated. In a second step, kerosene is added to the combustor until the defined TIT is reached. The burning equation follows

$$4\,C_{12}H_{23} + 71\,O_2 \rightarrow 48\,CO_2 + 46\,H_2O\ . \qquad \text{Eq. 4-14}$$

The empirical formula of kerosene and its properties e.g. the average molecular weight, enthalpy of formation and the net calorific value has been taken from Rachner, M. (1998). Based on the definitions for the specific heat capacity and enthalpy in Baehr, H.D. (2002) and user-defined coefficients for the polynomials, the exhaust gas composition, its specific heat capacity and the specific heat ratio are calculated for each operating point. It has to be kept in mind for the off-design analysis that temperature deviations in the combustor are only due to transients in composition or mass flow transients at the cathode inlet and not due to electrochemical interaction at the membrane.

4.5 Dynamic Process Modelling

4.5.1 Radial Compressor

A reliable dynamic compressor model has been proposed by Greitzer, E.M. (1976). According to Fig. 28, it comprises three sections, which are the duct, plenum, and throttle.

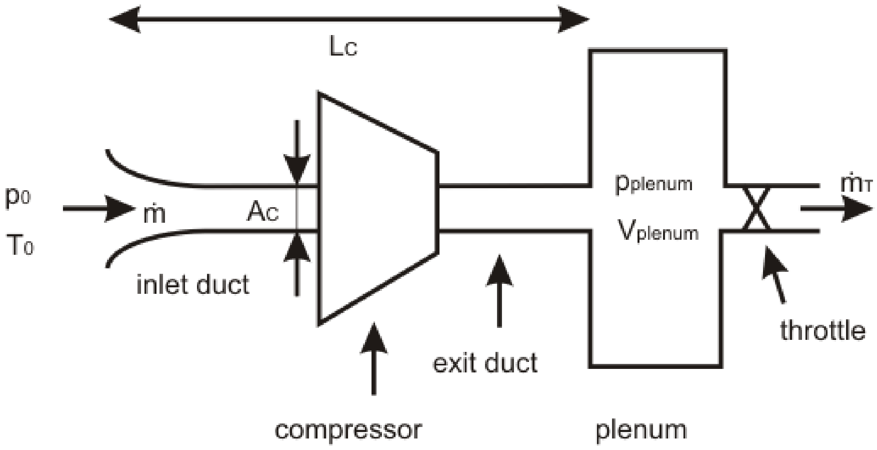

Fig. 28 Compressor model according to Greitzer, E.M. (1976)

The model has been developed for transient modelling of single-stage and multiple-stage axial compressor performance in the stable operating regime as well as for operation prediction during stall and surge of the compressor. As a result, Greitzer, E.M. (1976) deduced stability criteria for on-set of and distinction between surge and rotating stall, which are dependent on two compressor geometry parameters, the compressor length L_C and the cross sectional area compressor inlet A_C, and plenum characteristics. Despite its simplicity, these criteria have kept relevance for present system stability analysis. Based on experimental data, Fink, D.A. (1992) reports that the model can also be applied for radial stages, although it is developed for axial stages. The model is based on simplifications such as:

- One-dimensional incompressible flow in compressor duct
- Isentropic change of state inside the plenum
- Linearisation of turbine characteristic
- Negligible length of throttle duct
- Negligible gas angular momentum in compressor passage

The compressor is simulated as an actuator disc or a discontinuity plane across which pressure and temperature increase instantaneously inside the duct, with the pressure rise described by the steady-state compressor map. The dynamic system equations are derived from the conservation of momentum and mass for the duct and the plenum, respectively, which are

$$\frac{d}{dt}\left(\Delta p\right)=\frac{\kappa\cdot R\cdot T_{plen}}{V_{plen}}\cdot\left(\dot{m}-\dot{m}_T(p_{plenum})\right)=\frac{a_{plen}^2}{V_{plen}}\cdot\left(\dot{m}-\dot{m}_T(p_{plenum})\right) \qquad \text{Eq. 4-15}$$

and

$$\frac{d}{dt}\left(\dot{m}\right)=\frac{A_c}{L_c}\cdot\left(p_C(\dot{m}_{red},n_{red})-\Delta p\right). \qquad \text{Eq. 4-16}$$

It can be seen that the plenum volume and sound velocity inside the volume affect the pressure change rate. Both equations are coupled with each other and are of non-linear character which describes the inertia of gas dynamics inside the compression system.

A third equation is proposed by Greitzer, E.M. (1976) to account for the dynamic pressure rise over the compressor:

$$\frac{d}{dt}\left(\Delta p_C\right)=\frac{1}{\tau_C}\cdot\left(\Delta p_{C,stat}-\Delta p_C\right)\text{with}\,\tau=\frac{L_C}{c_{mer}} \qquad \text{Eq. 4-17}$$

The compressor response time is simulated by a first order time lag in the order of the through-flow time of the compressor, which is obtained from experimental data. The difference between static and dynamic pressure rise over the compressor becomes negligible for systems of a large plenum volume as it is the case in this analysis. It is therefore not applied in the present model.

4.5.2 Shaft Dynamics

For the modelling of the transient change of shaft speed, the conservation of angular momentum is applied. The shaft dynamics for the turbocharger are expressed by

$$\frac{d}{dt}(n) = \frac{1}{4 \cdot \pi^2 \cdot J} \cdot (\tau_m + \tau_t - \tau_c) \qquad \text{Eq. 4-18}$$

The moments of inertia for the two shafts are dominated by the two compressors and the turbine, which are calculated from geometric parameters obtained from the design procedure. In the case of the reformer air compressor, no turbine torque exists. The turbine and compressor torque are obtained directly from the static performance maps, while the shaft speed, as result of this equation, is fed back to these calculating blocks, respectively. It can be seen from Eq. 4-18 that if the turbine torque is not equal to the compressor torque, the shaft speed will change with time. One important actuating parameter is therefore the power or torque to obtain a specific control action such as constant shaft speed or constant pressure output during system transients.

4.5.3 Plena

Based on the dynamic compressor model in Section 4.5.1, the plenum between the compressor outlet and compressor throttle is considered (as only this section is of importance for compressor stability analysis). In various SOFC and PEM system analyses, all volumes occurring on the air and exhaust gas path are summarised by one plenum. Consequently only one throttle exists, which is often the gas turbine itself. This represents a simplification especially when several technical devices are sequentially arranged each exhibiting different size and therefore volume. In preliminary analyses for the present work, it has been verified by a simple mass flow increase scenario that the air system response is changed significantly when calculating with one or several sequentially arranged volumes. Pressure and mass flow at turbine inlet is strongly affected due to the long air path. The accurate description of the turbine power output is important for the mechanical power management of the turbocharger section and the necessary control action which again impacts the subsequent controller design. A severely delayed pressure and mass flow information at turbine inlet, for example, leads to a higher electrical power demand, which underlines the importance of small device volumes not only from the weight management point of view.

Therefore the model has been extended in a way that the volumes between the compressor and the turbine (humidifier, PEM-stack and post combustor) are each represented by one volume model and one pressure loss characteristic. It is assumed that a lumped distribution of temperature and density for each volume achieves the necessary accuracy for overall system analysis without stepping too deeply into the reactor's details and thus increasing calculation time. This strategy limits the detection of failure mechanisms which are of local character e.g. within the reformer. If these local mechanisms have impact on overall process stability and range, they have to be indicated by appropriate criteria as it is done for the surge limit of the compressor. For the pressure change the conservation of mass is applied with

$$\frac{d}{dt}\left(p_{unit}\right)=\left(\frac{R\cdot T}{V}\right)_{unit}\cdot\left(\dot{m}_{in}-\dot{m}_{out}\right). \qquad \text{Eq. 4-19}$$

Due to the thermal requirements in the humidifier and the stack, the temperatures of the gases show only small deviations from steady-state values during off-design operation and transients and are therefore considered to be constant.

A fully aerodynamic modelling of one device is possible if the equation of momentum is introduced. This is represented in our case by the simple pressure loss correlations such as Eq. 4-12, p.46. These equations are again coupled with each other and are of non-linear nature. This presented model strategy has a modular character. This means that the pressure loss characteristic can be easily implemented or modified for each device. The interaction between the equations is shown in Fig. 29.

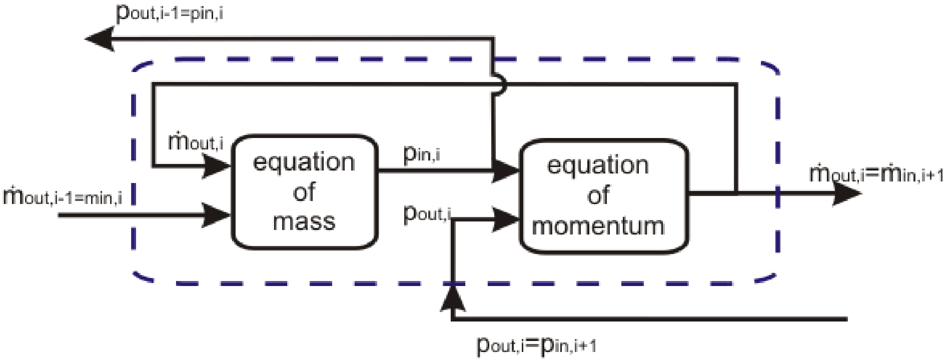

Fig. 29 Downstream pressure modelling strategy for the distributed device volumes

The downstream pressure of each device is then defined by Eq. 4-19, which is solved for the next downstream device. The last device is the radial turbine while its backpressure is the altitude dependent ambient pressure. This modelling strategy is costly in calculating time as pneumatics has to be calculated against the mass and energy flow. It takes however into account the dynamic pneumatic interaction of each device and allows therefore a more accurate evaluation of overall system dynamics.

4.5.4 Compressor Stability Aspects and Surge Modelling

4.5.4.1 Characterisation of Rotating Stall and Surge

Compression systems exhibit aerodynamic instabilities like rotating stall and surge. Surge is known as overall oscillation of the annulus-averaged axial flow in the compressor. Rotating stall, in general, is not symmetric but is characterised rather by a wavelike disturbance with rather small amplitudes when compared to surge. As a general explanation, both phenomena are initiated by local boundary layer separation in the impeller or the diffuser section due to low kinetic energy of the fluid at low flow numbers and high head coefficient. Rotating stall is often observed as a precursor of surge and commonly considered to trigger surge in the compression system. In radial compressors, a distinction between those two phenomena is sometimes difficult as they are observed to appear closely together. When all impeller vanes are stalled over the entire passage height, surge is present, turning the more-dimensional phenomenon into a one-dimensional one, as the entire mass flow through the compressor starts oscillating. Amplitudes may be higher than the average meridional velocity causing flow reversal in the compressor.

Surge and rotating stall must be avoided for safe operation as they induce large mechanical loads on the structure and entail a significant loss of power. While surge leads to instantaneous damage of the impeller and bearings due to the high energy density of the fluid impact on the impeller, rotating stall might cause excessive heating of the blade structure which can result in fatigue of the compressor. For overall operation, a reversal of the cathode mass flow or fluctuations in the gas processing air can lead to severe damage of the corresponding devices and thus lead to a complete break-down of the PEM-system. In practice, the surge line of a specific compressor is obtained from experimental data. This line is moved to higher mass flows providing an arbitrary but reliable operating limit of the compressor which represents the so-called surge margin. Unfortunately, steady-state operation near the surge limit allows for both high pressure ratio and high efficiency, two main requirements of a compression system. During transient operation, the surge margin might not suffice to prevent the compressor from surge as the operating line might temporarily trespass the surge line though start and end point of the transient control action lie in the stable region. Special attention will be paid to this circumstance during transient process analysis and controller design (Chapter 6, p.72).

4.5.4.2 Review on Surge Modelling

Presently, no integral theory exists for the analytical description of all surge and stall phenomena, as they appear to be highly complex and interacting with each other while dependent on a whole set of boundary conditions. Therefore, surge and rotating stall prediction is limited especially with newly designed and not experimentally evaluated compression systems.

As a simple circumstance, it has been observed that oscillating pressure and mass flow occur during operation in the region of positive gradient of constant speed line, see Japikse, D. (1996). The assumption that the on-set of surge correlates with the saddle point of the speed line is not only in good accordance with numerous experimental data obtained from axial and radial compressors but also allows an analytical approach available from system theory. It can be generally stated that the compression system is unstable for

$$\left.\frac{\Delta\Psi}{\Delta\Phi}\right|_{n=\text{constant}} > 0 \qquad \text{Eq. 4-20}$$

and metastable for

$$\left.\frac{\Delta\Psi}{\Delta\Phi}\right|_{n=\text{constant}} = 0 \qquad \text{Eq. 4-21}$$

.

As a mechanical analogon, Greitzer, E.M. (1976) considered the compression system as a Helmholtz resonator, oscillating with the Helmholtz frequency when a disturbance is introduced into the system. It can be defined by the geometry in and downstream of the compressor as

$$\omega_H = a \cdot \sqrt{\frac{A_C}{V_P \cdot L_C}} \qquad \text{Eq. 4-22}$$

.

The system equations Eq. 4-15 and Eq. 4-16, p.48, can be normalised to allow a general stability analysis. The mass flow is normalised by $\rho_0 A_C U$, the pressure difference by $1/2\rho_0 U^2$ and the time by the inverse Helmholtz frequency $1/\omega_H$, obtaining

$$\frac{d(\Delta\Psi)}{d\tilde{t}} = \frac{2 \cdot \omega_H \cdot L_c}{U} \cdot (\Phi_C - \Phi_T) \qquad \text{Eq. 4-23}$$

and

$$\frac{d\Phi_C}{d\tilde{t}} = \frac{U}{2 \cdot \omega_H \cdot L_c} \cdot (\Delta\Psi_C - \Psi_T) \qquad \text{Eq. 4-24}$$

where

$$B = \frac{U}{2 \cdot \omega_H \cdot L_c} \qquad \text{Eq. 4-25}$$

represents a factor, which summarises the dynamic behaviour of the system during instability. It is dependent on rotational speed and the speed of sound within the plenum. The achievement of Greitzer, E.M. (1976) was to transform the system equations in such a way that the application of a stability analysis known from a non-linear mass-damper system is possible. He further demonstrates that, once the compressor instability is triggered, the B-parameter serves as indicator whether rotating stall or surge and which type of surge is to be expected. For great B-parameters (>5), deep surge occurs while small B-parameters ($\approx$1) lead to mild surge. Very small B-parameters ($\approx$0.5) do not lead to surge but trigger rotating stall accompanied by a small pressure and mass flow drop at a new steady-state operating point without overall oscillation.

4.5.4.3 Criteria for Modelling of Surge and Surge Margin

The stability analysis presented in Greitzer, E.M. (1976) reveals that the type of periodic motion is of non-linear, non-conservative character, where energy is fed into the oscillation over part of the cycle so that the motion is maintained even if dissipative forces are acting. The conditions necessary for periodic oscillations is not a critical value of the slope anywhere on the compressor characteristic but rather in a region surrounding the point of zero slope. For surge to occur, the compressor characteristic must have a positive greater slope than 1/(B^2F'), over some part of the cycle, where F' represents the slope of the throttle characteristic. The on-set of the instability, though, is only possible when the criterion defined in Eq. 4-20 is fulfilled.

Deviations from this theory can be observed when surge occurs already at small but negative slopes which are close to the maximum of the constant speed line. Additionally, when the curvature of the speed line is very flat and the region of small slope is wide, as it is the case with vaneless diffusers, the distinction of the surge point is difficult and seems to be arbitrary.

As further surge criterion might serve the deHaller number or diffusion ratio of the impeller. Generally, a minimum value of 0.7 has to be attained in order to assure stable operation for the design point. It has been found that the on-set of surge in the available data sets of suitable turbocharger compressors coincides when the diffusion ratio of the impeller reaches the value of 0.62. For low shaft speeds, the surge line overlaps almost exactly with the maximum of the curve while at intermediate and high shaft speeds this point is found right of the maxima of the speed lines. Concerning the preceding consideration, this surge criterion has been applied for the present analysis as surge is not expected at higher diffusion ratios. As it encircles a smaller operating range than defined by the criterion of zero slope of the speed line, it represents the more conservative criterion and is therefore favoured.

In order to simulate real operation conditions, a surge margin has been applied for the subsequent analysis. Once the surge line for the entire compressor map is determined from the aforementioned criteria, each value is increased by 20 %, representing the surge margin and thus the operating limit for low mass flows.

$$\dot{m}_{\text{surgemargin}} = \dot{m}_{\text{surge}} \cdot 1.2 \qquad \text{Eq. 4-26}$$

This value appears to be high but represents again a conservative strategy.

5 Steady-state Air Supply System Analysis

This analysis gives insight into the general characteristics and thus operating limits of the system for steady-state operation but covers also slow transient demands when occurring in the domain of 2.5% of the design power output per minute. This is a typical scenario, see Fig. 3, p.9, during the climb and descent motion of the aircraft, and can be regarded as quasi-steady. Changes of ambient conditions occur at a time constant which is one magnitude lower than a corresponding load transient. Faster transients evoked by a change of power demand are addressed in the subsequent chapter. The following analysis aims at the improvement of the most important air supply system characteristics which are

- The turbocharger (TC) drive power and
- The mass flow range.

Both are dependent on the operating altitude. The turbocharger drive power decreases the overall power output and also system efficiency and should be decreased through the setting of the system parameters. The mass flow range of the air supply system defines to a great portion the overall operational flexibility of the FC power unit and should be increased.

The following aspects have been found to be sensitive on the TC drive power and the mass flow range:

- Cathode pressure
- Pressure loss across the cathode
- Turbomachinery design
- Application of co-firing

The improvement of the TC drive power and the mass flow range is carried out in two separate sections, while it can be expected that the setting of one system parameter is favourable for one system characteristic but counteracting with the other.

The calculations are based on the concept presented in Fig. 7, p.14. The design operating point of the entire system is set for cruising flight conditions. An overview of the design point boundary conditions is given in Tab. A-1, p.109.

5.1 Improvement of the Drive Power for Constant Cathode Mass Flows

For the improvement of the TC drive power, the cathode mass flow is held constant maintaining constant air utilisation. It is of interest to find a design parameter setting which points to the minimum use of external power for the air supply system.

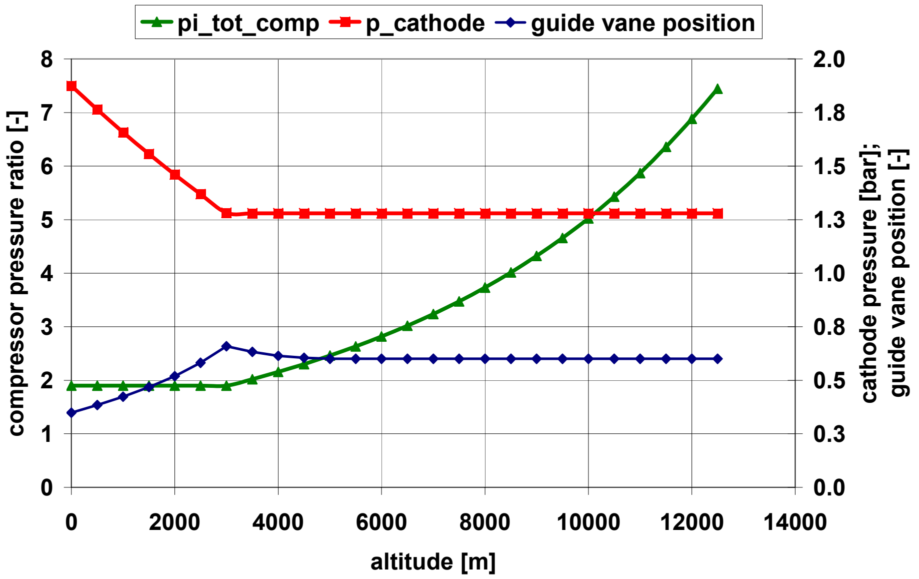

Fig. 30 Air supply system parameters as a function of the operating altitude

Though operation is possible with a constant cathode pressure, it has been found early during the analysis that this strategy leads to high power consumption at low altitudes, which is due to the low turbine expansion ratio. A better strategy is to increase the cathode pressure for operation below altitudes of 3000 m until a maximum value is reached e.g. at sea level (see Fig. 30).

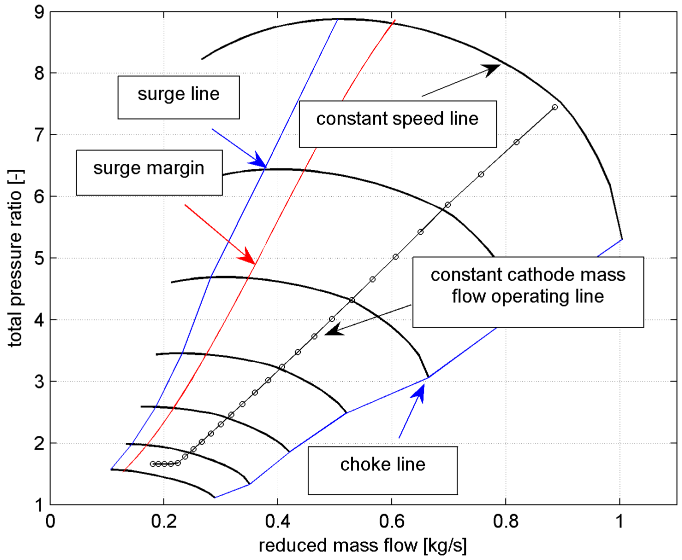

Fig. 31 Operating line in the compressor map as a function of the operating altitude

For a first step, the cathode pressure is steadily increased to a maximum value of 1.9°bar. The corresponding operating line in the compressor map is shown in Fig. 31. A detailed discussion of the optimum cathode pressure as a function of the altitude is carried out in Section 5.1.1.

An overview of the compression and expansion ratio and the area ratio of the guide vane at the turbine inlet is given in Fig. 30. The area ratio peak around 3000 m is a result of the fixed pressure ratio for altitudes below 3000 m. As cathode inlet pressure decreases faster than ambient pressure, the effective turbine pressure ratio decreases. It reaches a minimum at this altitude and has to be compensated by a higher area ratio in order to maintain the required constant cathode mass flow.

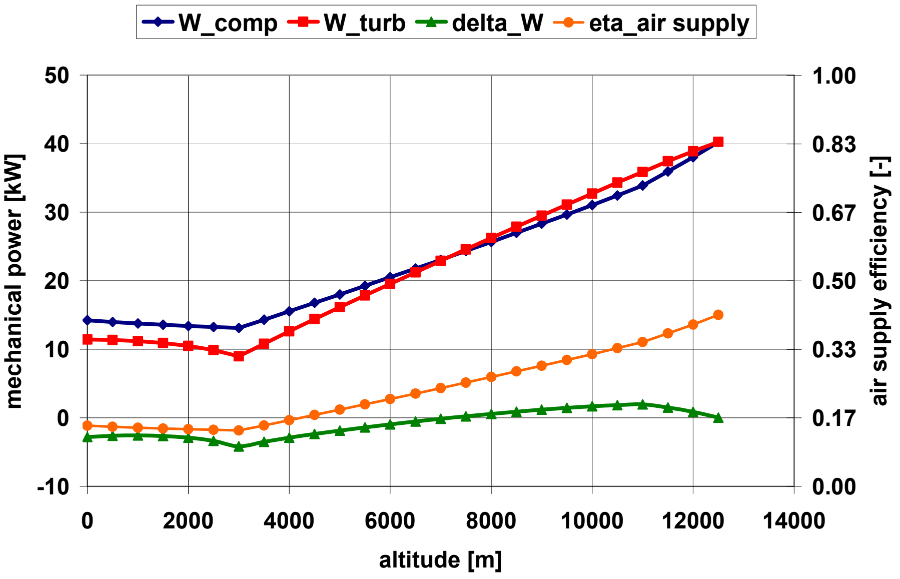

Fig. 32 Power management of the turbocharger

An insight into the power management of the turbocharger section is given in Fig. 32. According to the considerations made in Chapter 2, the turbine power output and compressor power demand are balanced for the design point. For decreasing operating altitudes, turbine power output is slightly higher than the power demand but drops faster than the compressor demand. The power gap increases for low altitudes and is then approximately constant. The maximum TC drive power is around 4 kW and is considered to be acceptable for the prototype concept. If the cathode pressure would have been held constant also at low operating altitudes, the power demand would increase beyond 10 kW.

It is meaningful to formulate a supply efficiency for the air supply system and thus to allow an evaluation of the driving device. It can be formulated by

$$\eta_{supply} = \frac{\dot{W}_{compressor,mech}}{\dot{W}_{Kerosene} + \dot{W}_{anode off-gas}} \qquad \text{Eq. 5-1}$$

and compares the mechanical power demand of the compressor with the chemical energy introduced to the post-combustor. In the case of co-firing, these are the portions of unused hydrogen among the cathode off-gases and the additionally injected kerosene. This mechanical efficiency is not to be mistaken with a thermal efficiency calculated for a Joule process. This would be in the present case equal to zero as no additional shaft power is taken from the Joule process. The efficiency definition allows a comparison with other compressor driving devices e.g. an electric motor but also for mixed operation strategies such as co-firing and simultaneous electric support. Consequently, a direct trade-off can be made between the cathode pressure function and the FC design power output.

The supply efficiency without co-firing is shown in Fig. 32. It is steadily increasing with altitude due to the increasing expansion ratio. As it gives also the efficiency value when the process is co-fired it provides an evaluation criterion whether co-firing is favourable not only from power generation but also from an efficiency point of view. In order to satisfy e.g. high long-term power demands, where overall kerosene consumption becomes important, it can be then decided on this ground whether it is favourable to change the operating point of the FC or to burn additional kerosene in the post-combustor.

5.1.1 Cathode Pressure Function

There exists a whole set of possibilities to define the cathode inlet pressure as a function of the altitude. For keeping the number of free parameters low, firstly, a simple function has been chosen: The compressor pressure ratio does not fall below a minimum value.

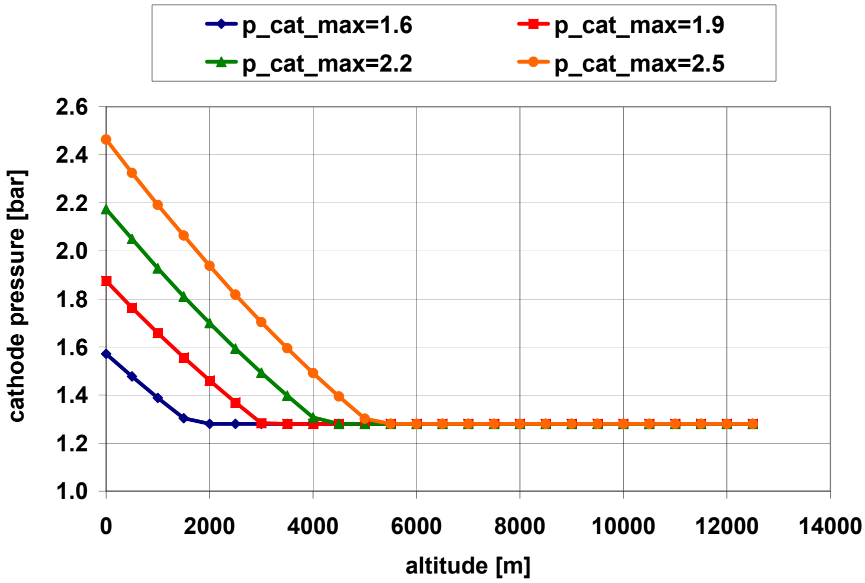

Fig. 33 Simple cathode pressure function

Consequently, the cathode pressure increases with descending altitudes. The free parameter is the minimum pressure ratio which is varied and evaluated, while the maximum cathode pressure is found at ground altitude, see Fig. 33. The corresponding operating lines in the compressor map are given in Fig. 34 and show that an increased maximum cathode pressure moves the operating line to the surge margin. Once the surge margin is reached cathode mass flow will have to be steadily increased to maintain a constant reduced mass flow (see Eq. 2-7, p.19).

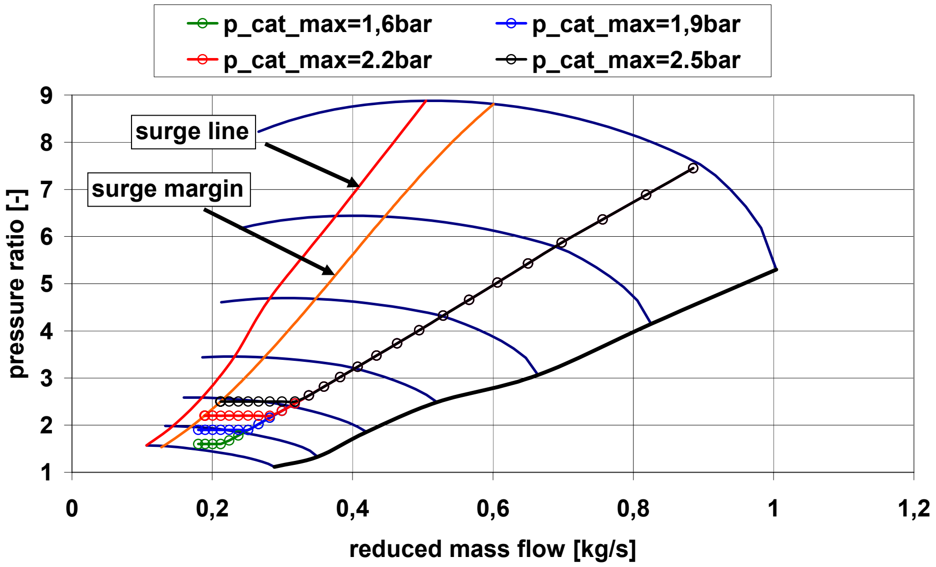

Fig. 34 Compressor map operating lines for the simple cathode pressure function

The TC drive power for these scenarios is given in Fig. 35. It is a result of the interaction of the unit performance and the cathode pressure function and therefore a good evaluation criterion. The power demand should be low and not changing abruptly over the altitude in order to minimise the steady-state and dynamic impact on the power management and controls of the FC unit.

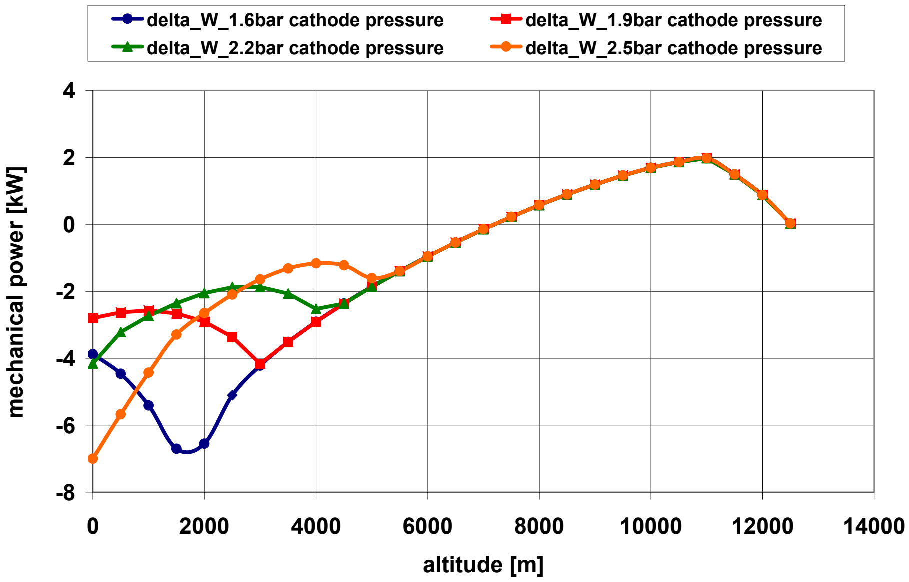

Fig. 35 TC drive power for the simple cathode pressure function

While a low maximum cathode pressure leads to a relative minimum at intermediate altitudes, the high maximum pressure shows high power demand at low altitudes. A cathode pressure of 1.9 bar shows moderate changes at low altitudes with a maximum power demand of 4 kW.

It can be summarised for the simple cathode pressure function that the cathode pressure of 1.9 bar is an optimum from power consumption point of view. It is however not satisfactory that the compressor operates near the surge margin at low operating altitudes.

The cathode pressure function is therefore modified where the minimum and maximum value as well as the slope of the linear section can be defined freely (see Fig. 36). The maximum cathode pressure is varied between 1.3 bar and 1.9 bar and held constant until an altitude of 1000 m. The minimum cathode pressure is reached at 7000 m, defining the slope of the cathode pressure curve. The optimum values for the corresponding altitudes have been found from iterations during analysis but can be also adapted to the designer's needs.

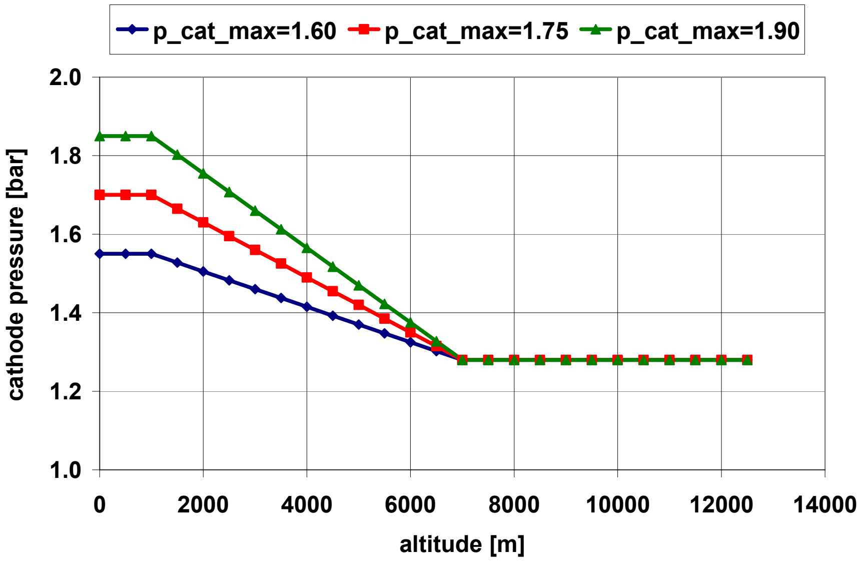

Fig. 36 Advanced cathode pressure function

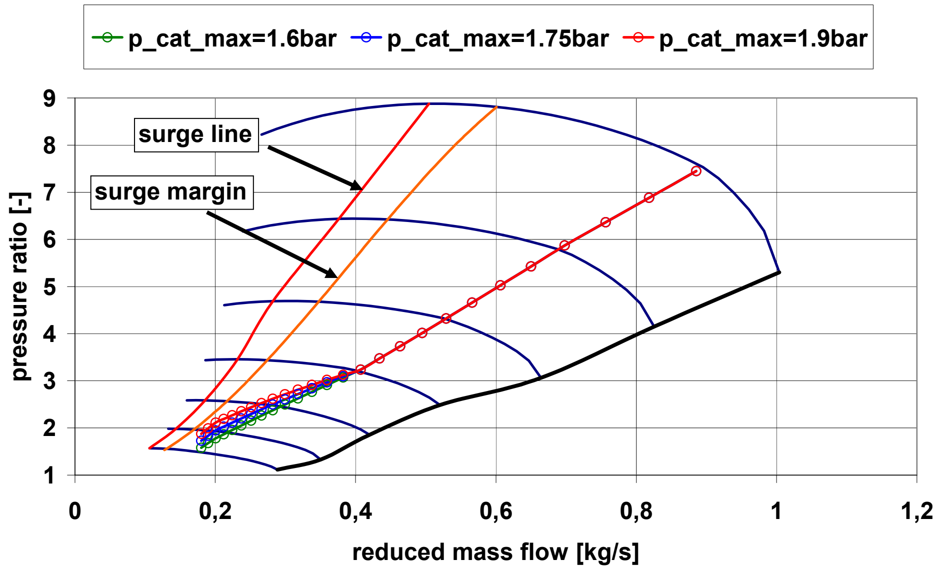

Fig. 37 Compressor map operating lines for the advanced cathode pressure function

This cathode pressure function shifts the operating lines at low altitudes away from the surge margin (see Fig. 37) and should be therefore favoured against the simple one. For high maximum pressures however this benefit is becoming small.

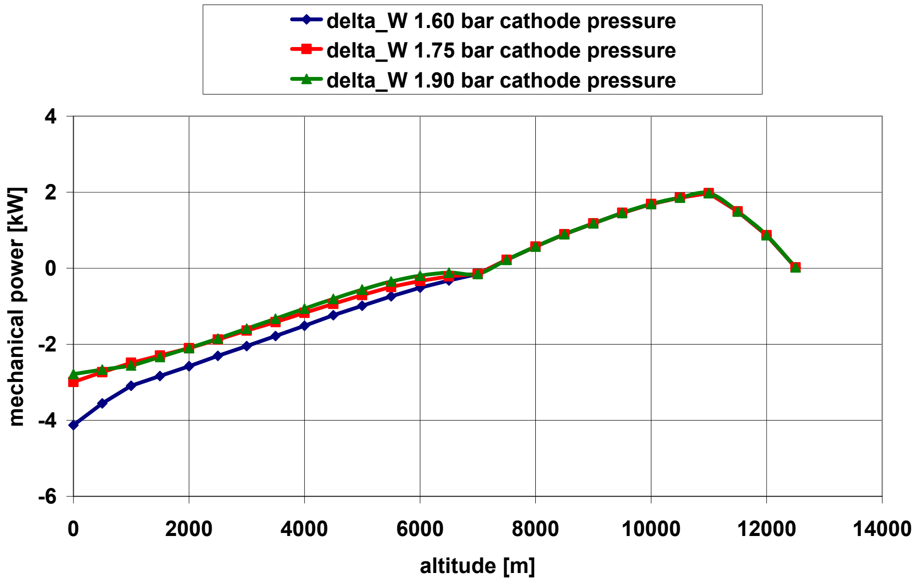

Fig. 38 TC drive power for the advanced cathode pressure function

A further advantage of this cathode function is that the TC drive power for the turbocharger section is smoothened along the envelope, see Fig. 38. The maximum power demand is now around 3 kW and reduced by 25% compared to the simple cathode pressure function. A maximum pressure beyond 1.75 bar gives no benefit for the external power demand, while moving the operating line towards the surge margin. Therefore, the maximum pressure is chosen with 1.75 bar and applied for the subsequent analyses.

5.1.2 Influence of the Cathode Pressure Loss

It is probable that demonstrator stacks are not optimised regarding the internal flow. The influence of an increased cathode pressure loss on overall performance is therefore investigated here. As the pressure loss characteristic is highly dependent on the unit design, the here followed pressure loss assumptions of linear and quadratic correlations for the cathode and the main devices on the gas path respectively are afflicted with a considerable uncertainty. The analysis shall demonstrate however the importance of an aerodynamically optimised flow path.

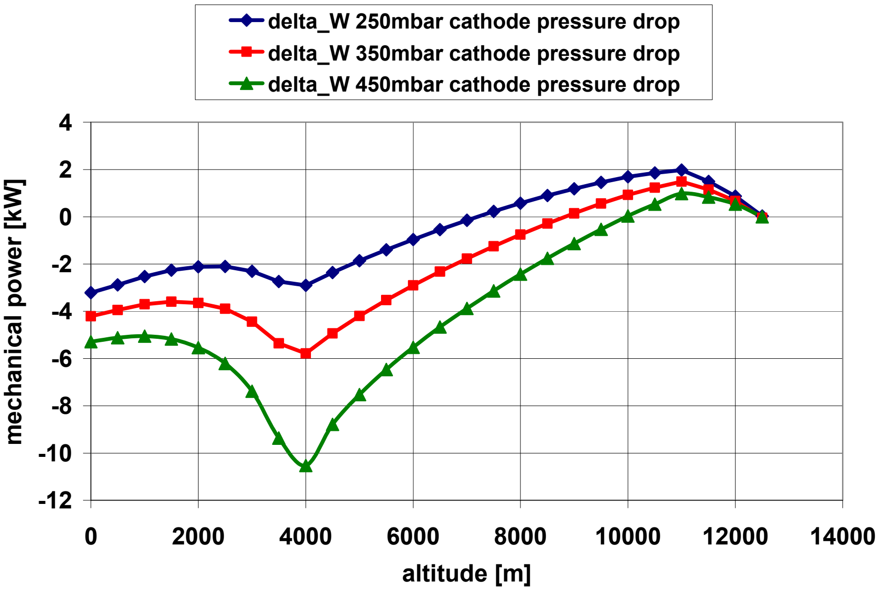

Fig. 39 TC drive power for the simple pressure function and a varying cathode pressure loss

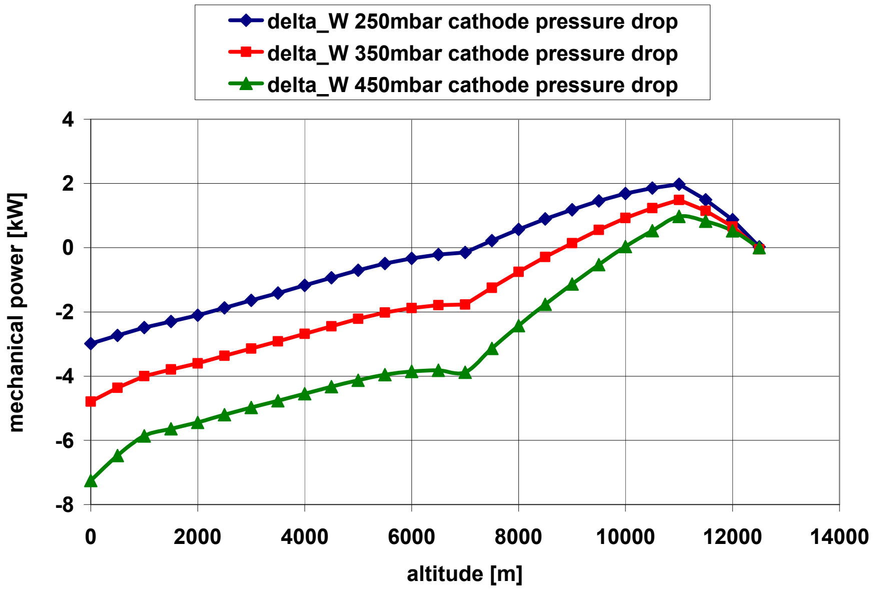

Fig. 40 TC drive power for the advanced pres. function and a varying cathode pressure loss

The drive power for the simple and advanced cathode pressure function is shown in Fig. 39 and Fig. 40, respectively. The drive power is significantly higher for the simple cathode pressure function with a power demand peak of around 10 kW when assuming a cathode pressure loss of 450 mbar. It will be decreased at low altitudes by the increasing cathode pressure but remains at a value of 6 kW at ground operation. The advanced cathode pressure function shows much smoother power demand curves for all pressure loss variations, but does not eliminate the increased power demand for the air supply throughout the envelope. It is well demonstrated by this analysis, that a low pressure loss across the cathode should be addressed early during the stack design as it significantly decreases the power to the air supply system.

5.1.3 Influence of the Turbomachinery Design

A core objective of this work is to assess the interaction of the turbomachinery design and the overall system performance, such as efficiency and operating range. The impact on the transient system behaviour will be addressed in particular in Chapter 6, p.72. Here, it is demonstrated to which degree the turbomachinery choice, its design, but also the matching of the compressor and turbine design have an impact on the TC drive power.

The drive power of the two-stage compression is shown in Fig. 41 for the advanced pressure function, which was shown in Fig. 36. If the two-stage compressor is replaced by the single-stage concept, the drive power demand is increased over the entire envelope in the range of 6 kW. This is due to the lower isentropic efficiency of the single-stage compressor. At cruising flight conditions, the power gap may increase up to 8 kW. This is particularly disadvantageous because of the long portion of the cruising flight throughout the envelope. This result is obtained if the turbine remains designed for the two-stage compressor.

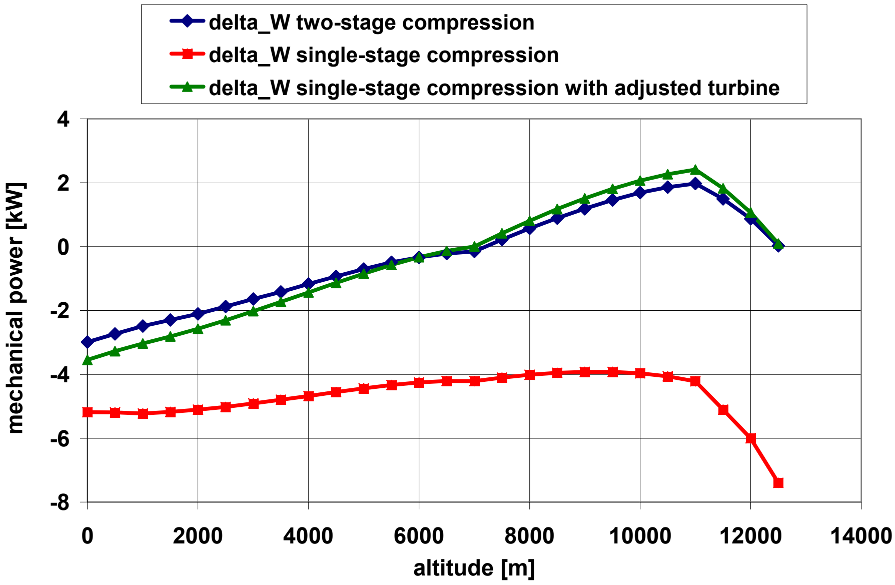

Fig. 41 TC drive power for the single-stage and two-stage compressor

A re-design of the turbine for the single stage compressor gives a similar drive power curve as for the two-stage concept, see Fig. 41, but requires a higher turbine isentropic efficiency. While the two-stage compressor turbine exhibits an isentropic efficiency of 0.62 for the design point, the single-stage compressor turbine design requires a minimum of 0.76. If this efficiency should not be achievable, a lower FC power unit efficiency throughout the entire envelope has to be accepted. This circumstance may outweigh the advantage of the compactness and lower weight of the single-stage compressor.

It can be now shown to which degree an improved turbomachinery design can influence overall system efficiency. This holds in particular when both components compressor and turbine are not only matched but also designed with a maximum isentropic efficiency. The maximum isentropic efficiency was a primary order criterion during compressor optimisation. The turbine efficiency for the radial turbine is obtained from a dimensionless efficiency map for different spouting velocities and geometry parameters (Whitfield, A (1990)). Maximum values of 0.88 are reported to be possible. If special attention is paid to the turbine design and design point efficiency is increased to a value of 0.82, the power consuming air supply system can be shifted to a fully power generating system as can be seen in Fig. 42.

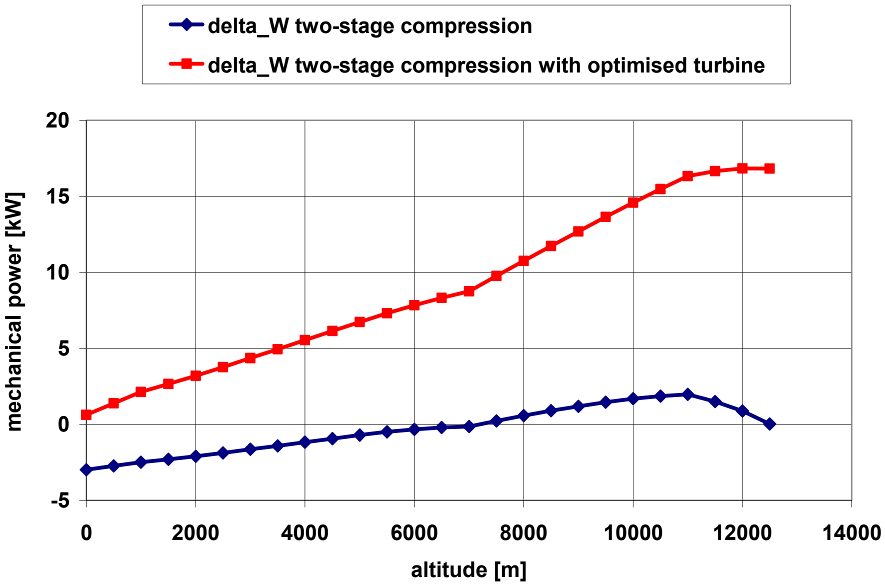

Fig. 42 TC drive power for an efficiency improved turbine design

While the air supply system is self-sustaining even at sea level, it can generate excess power of more than 15 kW at the design point becoming a bottoming Joule cycle as known from the SOFC-GT systems. The splitting of the generated power between fuel cell and air supply system (or GT in this case) represents, on the other hand, a major complication for operating strategies and controls as can be observed in the SOFC-GT application. Together with the application of a highly optimised compressor and turbine device, this scenario remains an option for systems which have proven feasibility and accomplished a successful commercialisation.

It can be summarised that the appropriate design of the turbine has significant potential to decrease the drive power of the turbocharger, and that sophisticated turbine design may change the air supply system into a power generating device.

5.1.4 Influence of Co-firing with Additional Kerosene

The possibility to apply a post-combustor and burn additional kerosene to eliminate external power demand and thus electric power management has been already addressed in Section 2.8.3, p.21. It can be shown in Fig. 43, that this operating strategy can be applied for operation down to sea level. At intermediate altitudes, the air supply generates a small amount of power but is then in equilibrium at cruising flight.

The turbine inlet temperature and the inlet guide vane position show moderate changes, see Fig. 44, which encourages assuming this concept to be technically feasible. The efficiency of the co-firing is low as it is applied at low and intermediate operating altitudes.

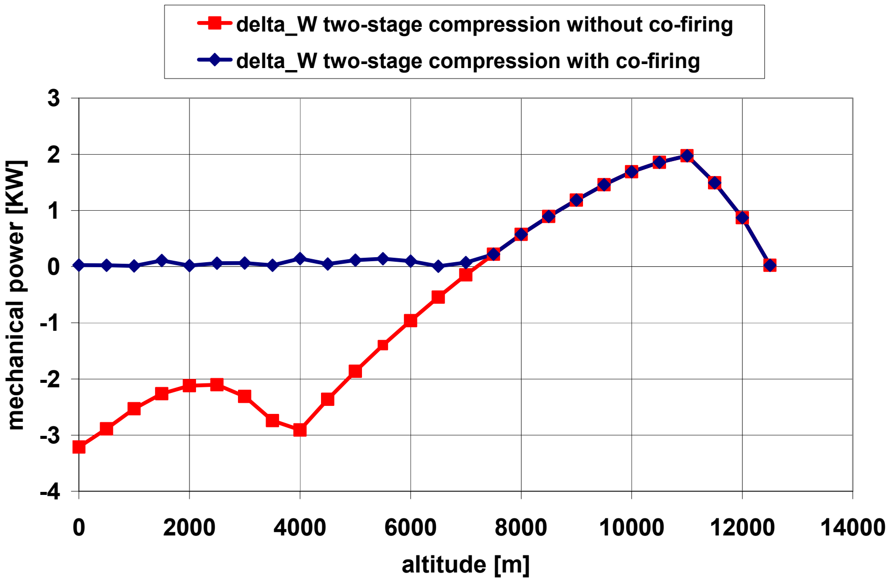

Fig. 43 TC drive power with and without additional co-firing

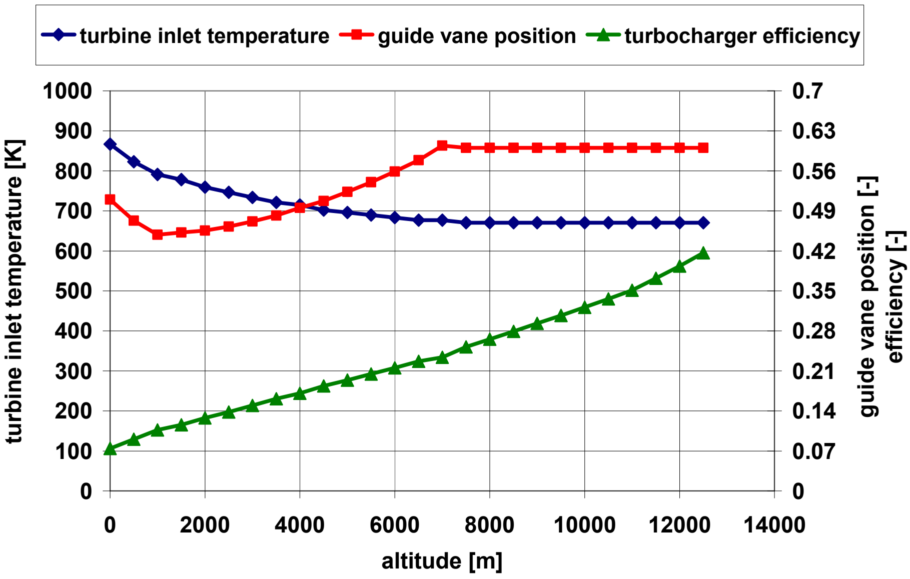

Fig. 44 System parameters during co-firing as function of the operating altitude

Co-firing represents therefore an option to overcome high power demands at low and intermediate altitudes but cannot be recommended for long-term operation. If minimum kerosene consumption is to be achieved for the overall FC power unit, it can be stated that the kerosene is explored more efficiently at the stack membrane than in the post-combustor.

5.2 Improvement of the Mass Flow Range

It is of interest for the overall operating strategy to detect to which degree the air supply system can follow air mass flow demands. One common requirement during stack transients is to maintain the air utilisation factor and thus stoichiometry at the cathode membrane. If the air supply system reaches its maximum operating limit, then the air utilisation has to be increased which again has negative impact on stack efficiency and the cooling management.

A great portion of the overall power unit operating range is therefore defined by the air supply mass flow operating range. This again is defined by the aerodynamic restrictions from the compressor and the turbine and the resulting power balance between the compressor and turbine. Further it is dependent on the pressure loss characteristics of the main devices such as the humidifier, the cathode, and the post-combustor. The following section aims at the demonstration of the potential to increase the mass flow range of the air supply system.

For a thorough variation of operating altitudes and possible cathode mass flow demands, an operating map for the TC drive power can be generated. It is shown in Fig. 45 in a three dimensional view and is plotted versus the entire compressor map. The corresponding inlet guide vane position is given in Fig. 46. An alternative visualisation in the two dimensional plane of these parameters is given in Fig. D-1 and Fig. D-2, p.125. The maps shown are valid for a constant cathode inlet pressure of 1.33 bar.

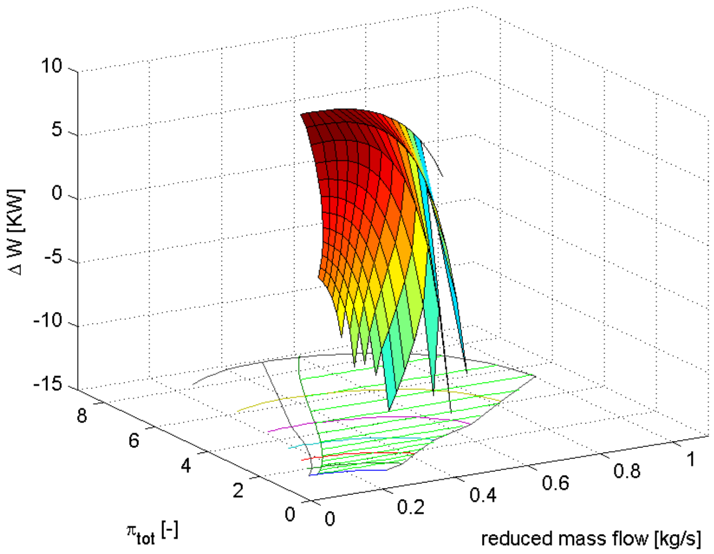

Fig. 45 3D map of the TC drive power as a function of the operating altitude and the mass flow

Once the operating altitude, the mass flow, and the pressure output are known, the TC drive power and the inlet guide vane position can be obtained from these maps. These parameters define the entire state variable vector of the air supply system and are therefore the setting parameters of the air supply system. They will be used as input vector for the subsequent control analysis.

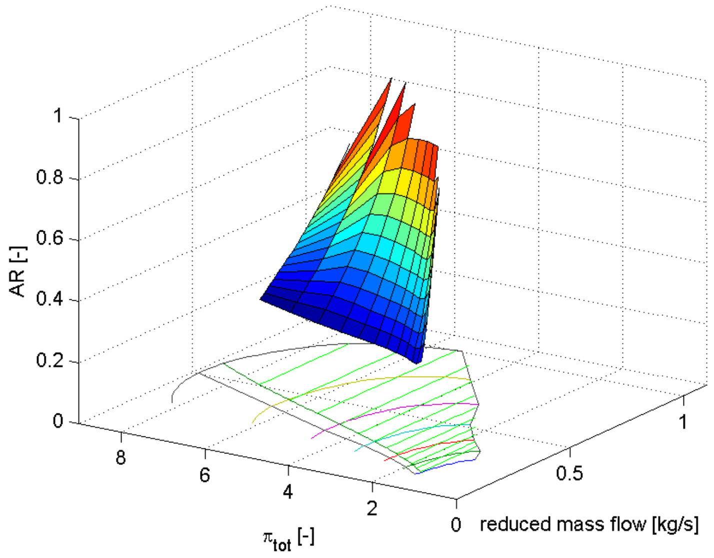

Fig. 46 3D map of the inlet guide vane position as a function of the operating altitude and the mass flow

As already addressed in Section 2.7, p.19, it is not useful for the design of the stack to use reduced mass flows. Only the real cathode mass flow has physical meaning at the membrane and has impact on stack chemistry and controls. In order to improve the clearness of the analysis results and to allow a comparison of the here presented options for increasing the mass flow range, an adapted presentation has been chosen, see Fig. 47.

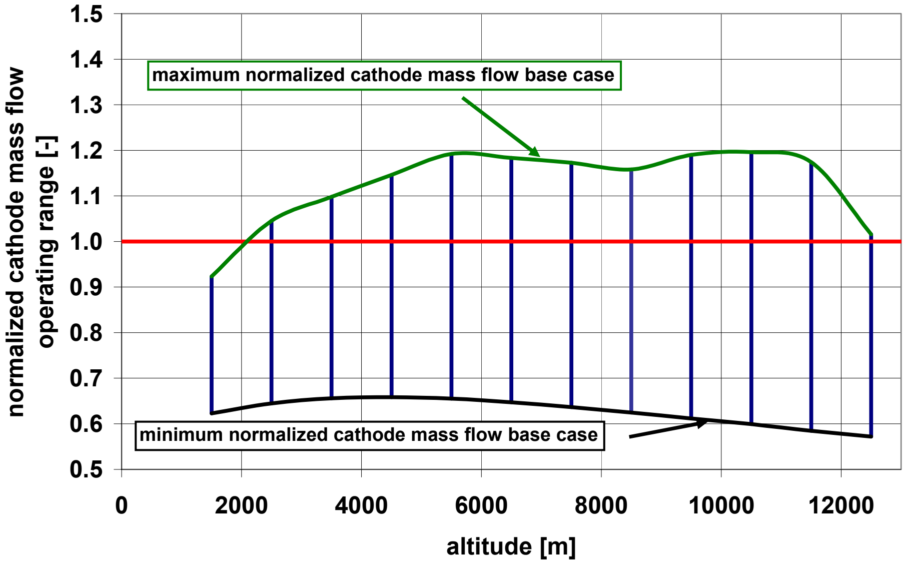

Fig. 47 Normalised cathode mass flow operating range for the base case

The cathode mass flow is normalised by the design cathode mass flow, which is indicated by the horizontal line. At each altitude, a minimum and maximum normalised mass flow can be depicted, which is defined by the compressor surge margin and the choke flow condition at turbine inlet, respectively. Extending this procedure over the entire altitude range, a complete cathode mass flow operating range can be depicted in one graph.

5.2.1 Influence of the Cathode Pressure on the Mass Flow Range

The importance of the cathode pressure function for the TC drive power has been addressed. It can be observed in Fig. 48, that the maximum mass flow can be significantly shifted to higher values when the cathode pressure is increased by 0.2 bar which is assumed to be feasible with a state-of-the-art stack design. It can be deduced that a further range extension is possible with higher cathode pressures. The reason for this circumstance is given in the turbine characteristic where the choke mass flow is higher due to increased turbine inlet pressure.

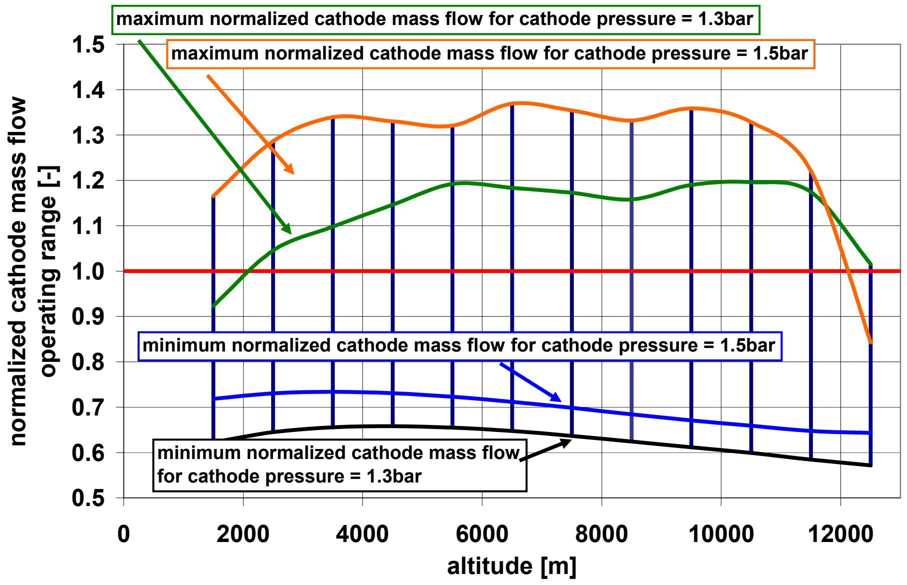

Fig. 48 Cathode mass flow operating range as a function of the cathode pressure

An increase of the cathode pressure, on the other hand, increases the TC drive power significantly for the entire operating range. To allow a better comparison of the increased power demand, the power difference between the modified case and the base case is shown for each operating point in Fig. D-3, p.126. It can be seen that, only if the cathode pressure is increased by 200 mbar at the cruising flight altitude, the air supply system has a power demand increase of up to 3 kW.

It has to be therefore considered that an increase of the cathode pressure with the aim to increase the choke mass flow has to be paid by a higher electric demand of the air supply system. The increase of the cathode pressure is therefore not an option for long-term operation but can overcome system transients where high mass flows are necessary. This is e.g. when the air utilisation in the stack is not to increase beyond a maximum value during high power demands.

5.2.2 Influence of the Cathode Pressure Loss on the Mass Flow Range

The importance of the cathode pressure loss for the TC drive power has been already demonstrated. In this analysis, the cathode pressure loss is increased by 200 mbar to a value of 450 mbar in order to demonstrate its impact on the mass flow range. High cathode pressure losses may be expected for the first prototypes.

The maximum operating range is affected negatively at low operating altitudes, see Fig. 49. The TC drive power, on the other hand, increases significantly, see Fig. D-4, p.126, over the entire altitude range and particularly at high mass flows. This can be explained by the remarkably decreased turbine inlet pressure.

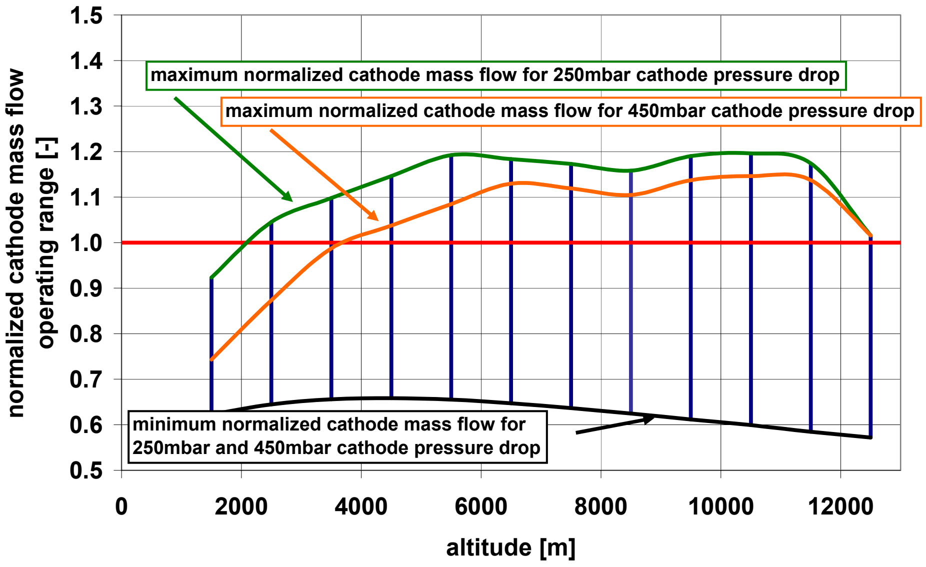

Fig. 49 Cathode mass flow operating range as a function of the cathode pressure loss

Consequently, the decrease of the cathode pressure loss has to be addressed early during the stack development as it decreases the TC drive power as well as increases the mass flow range.

5.2.3 Influence of the Turbine Design on the Mass Flow Range

Again, it shall be demonstrated how turbomachinery design influences overall performance of the power unit. In this analysis, the design inlet pressure of the turbine has been decreased from 0.98 bar to 0.78 bar by 200 mbar in order to investigate the influence of an unconventional design choice. Pictorially speaking, the turbine is designed too big.

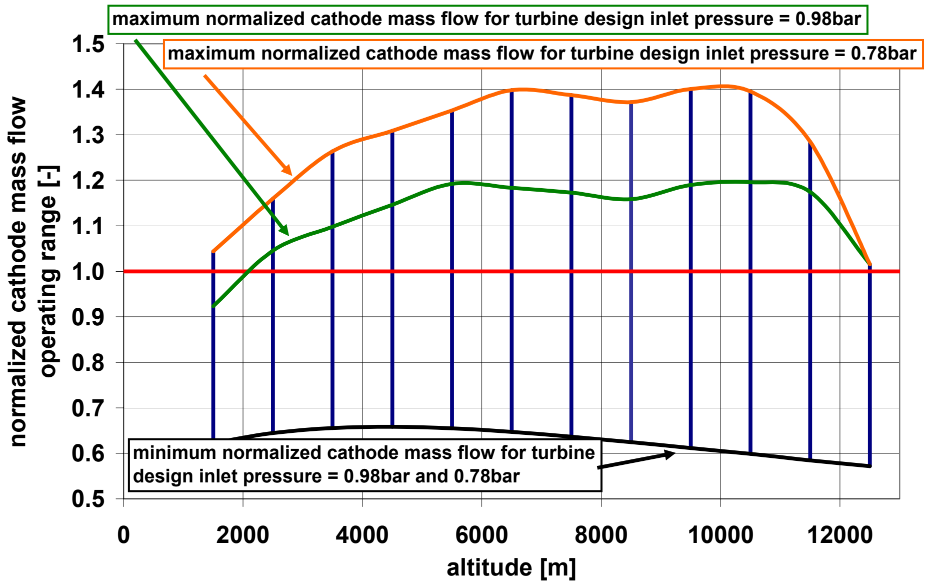

Fig. 50 Cathode mass flow operating range in dependency of the turbomachinery design

As shown in Fig. 50 and Fig. D-5, p.127, this choice reveals to be highly advantageous both for the mass flow range and the TC drive power. The maximum mass flow can be moved by approximately 20% almost over the entire altitude range while the drive power is decreased by 2 kW to 8 kW when compared to the base case.

It has to be kept in mind that a further decrease of the design inlet pressure leads to an increased cross-sectional area of the turbine, to a greater rotor diameter, and thus rotor moment of inertia, which will have a negative impact on the transient response characteristic of the air supply system.

5.2.4 Influence of Co-firing on the Mass Flow Range

The scenario of injecting additional kerosene into the post-combustor to decrease the TC drive power at high mass flow has been addressed in Section 5.1.4, p.64. It is found to be an option for short-term scenarios to overcome high load demands. It is shown in this analysis, how co-firing affects the mass flow range.

Due to the increased turbine inlet temperature during co-firing, the choke mass flow of the turbine decreases and simultaneously limits the maximum mass flow, see Fig. 51. At the same time, the mechanical efficiency of the air supply system drops beneath the values of the base case without co-firing as seen in Fig. D-6, p.127. Therefore, co-firing is not applicable when high mass flows are required.

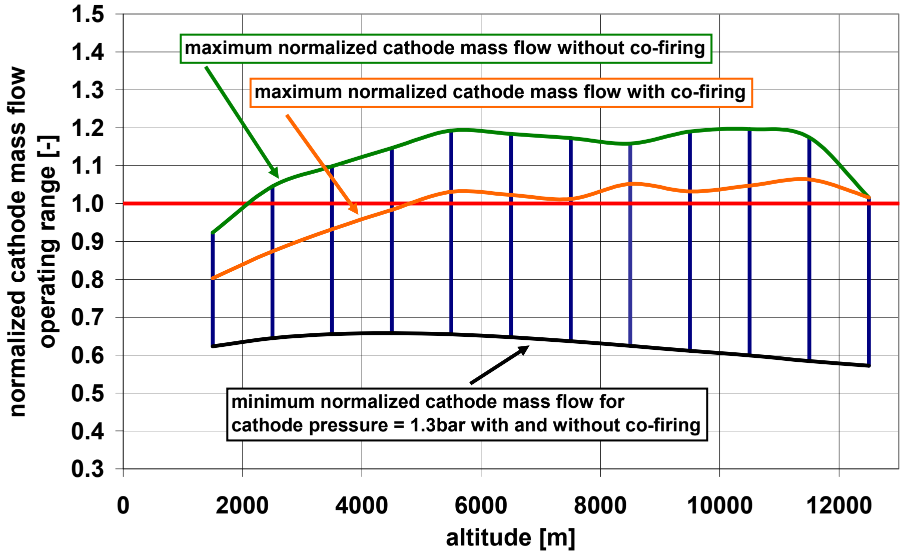

Fig. 51 Cathode mass flow operating range in dependency of co-firing

The drop of the operational flexibility might be compensated, regarding the preceding analysis results, by a simultaneous increase of the cathode pressure and the application of an adapted turbine design. Despite these modifications, the mechanical efficiency is expected to remain smaller than without co-firing, which excludes co-firing as an option for the long-term operation.

Considering now that efficiency plays a minor role for short high-power demands, which occur mainly during the climb and descent phase, co-firing can support the fuel cell power output by minimising the parasitic losses for the air supply. If TIT is increased up to 1000 K, the air supply can even generate power. The expected power output from the air supply system is then in the range of 10% of the design stack output. It can be assumed that this additional power can be activated quickly as, once the kerosene is ignited, it instantaneously increases turbine power.

Application of co-firing remains an alternative for overcoming fast power transients when the reformer path lacks response agility. This is especially true when the fuel cell operates at part-load and has to increase power output e.g. by a factor of two or more. Within the first seconds, safe operation is guaranteed until maximum cathode mass flow and air utilisation are reached. When the reformer has increased its hydrogen generation, co-firing can be reduced to allow for higher mass flows and also higher air utilisation in order to reach a new operating point at better efficiency.

It is comprehensible that co-firing requires a high level of understanding of the fuel cell and the air supply system and operational experience of the system under flight conditions. Further, the development of a dual combustor for hydrogen and kerosene represents a challenging development task. It is therefore left open at this analysis step, whether peak power demands could also be overcome with less development effort and less impact on the operating strategy.

6 Controls Optimisation Using a Simplified PEM-FC Model

In this section, the following guiding questions are answered:

- Which are the basic challenges and system requirements for safe transient operation?
- To which degree do the air supply system concept and the turbomachinery design impact the transient system characteristics?
- Which control architectures and strategies for the air supply system are possible to ensure safe and quick overcome of transients?

While slow transients can be well covered by off-design analysis, here fast power demand changes shall be investigated, see Fig. 3, p.9, and will be evaluated for the presence of critical operating conditions. Power increases of up to 20% of the design power output per minute can be expected for the more electric aircraft design at the end of the climb phase and must be covered by the power unit. These considerations can only be evaluated with fully dynamic models as applied here. Critical operating conditions such as compressor surge or dehydration of the stack membrane will be considered. In order to separate the turbomachinery-specific from the PEM-specific influences and to focus on the air supply section, the highly detailed PEM model will be introduced in a separate section.

In order to allow and cover fast pneumatic transients but also for safety reasons, the application of a blow-off valve at compressor outlet (for a fast decrease in mass flow demand) might be necessary. The use of a blow-off valve clearly imposes pneumatic (pressure) disturbances on the system which are believed to be more acceptable than to shut down and restart the air supply as a consequence of compressor surge. As during blow-off operation, the cathode and reformer mass flow are not significantly decreased, no critical conditions are expected for the reformer or the stack. Very fast power demands, such as power peaks occurring when several power devices are switched on simultaneously, are not discussed here. They are not expected to have an impact on air supply design but rather on stack and power management design.

As two setting parameters (the inlet guide vane position at turbine inlet and the TC drive power) are available, only two variables can be controlled for the air supply system. These are the compressor mass flow and the compressor outlet pressure. It is necessary to vary the mass flow in order to maintain constant air utilisation during power transients. Cathode pressure changes are required throughout the altitude range, as discussed in the Section 5.1.1 on the cathode pressure function, and during load transients. The first requirement represents only a quasi-steady change due to a relatively slight temperature and pressure gradient as a function of the aircraft's climb and descent velocities. A fast pressure increase might be helpful to raise the PEM power output by increasing stack efficiency through increasing the pressure dependent Nernst potential. A decrease of the cathode pressure at cruising flight conditions, on the other hand, can help to increase the maximum mass flow due to the compressor map characteristic, see Section 5.2.2, p.68.

6.1 Open-loop Analysis

In order to quantify system behaviour, a mass flow and pressure increase step function of 20% compared to the design operating point is examined. The analysis is carried out for a flight altitude of 6000 m, during the climb or descent period where high load fluctuations occur on-board, see Fig. 3, p.9.

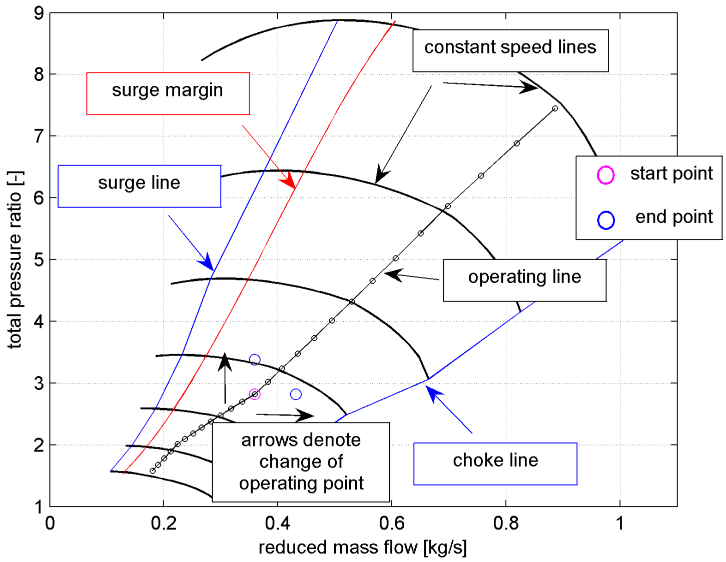

Fig. 52 Step response analysis for a cathode mass flow and pressure increase

The corresponding compressor map is given in Fig. 52. The operating range is limited by the surge margin and the choke line. The dotted black line gives the operating line of the air supply system throughout the entire envelope while the PEM-FC is run at design mass flow and cathode pressure. It is slightly increased at low flight altitudes moving the operating line towards the surge margin as it has been deduced to be optimum for the maximum mass flow operating range and minimum power demand at low altitudes.

An overview of the assumed lumped volumes of each unit and the rotor moment of inertia obtained from the turbomachinery geometry is given in Tab. 6. The design case is characterised by the boundary conditions presented in Tab. A-1 and Tab. B-2, p.118. Unlike in classical step response analysis where only one parameter is changed to analyse state space response, both electric support and the guide vane position of the turbine are set to values defining a new steady-state operating point. These are a mass flow increase at constant compressor pressure or vice versa. Thus it is possible both, to evaluate system response for a scenario which is relevant in the present application and to demonstrate the transient system characteristics. Obtained from the preceding off-design analysis, the setting values of the inlet guide vane position and TC drive power are available from the three-dimensional function presented in Fig. 45 and Fig. 46, p.66, respectively. The system response of the turbocharger section is shown in Fig. 53 for the design case and an increased PEM-FC volume or rotor moment of inertia by a factor of three, respectively.

Tab. 6 Design point assumptions for the main components of the air supply system

parameter	value	Unit
volume		
- compressor	0.025	m^3
- humidifier	0.150	m^3
- PEM-stack	0.500	m^3
- combustor	0.150	m^3
rotor moment of inertia:		
- turbocharger	0.00486	$kg\ m^2$
- reformer compressor	0.00112	$kg\ m^2$

It is of interest and might be called “ideal” that during a mass flow increase, compressor pressure output remains constant and vice versa. This system characteristic cannot be expected, though, when regarding the non-linear character of the compressor dynamics given in Eq. 4-15 and Eq. 4-16, p.48, and the interdependency between the compressor and turbine characteristics.

It can be recognised in Fig. 53 that the operating line is deviating in each scenario from the optimum line, while a pressure increase results in a strong decrease in mass flow towards the surge margin. In the case of increasing the mass flow, the large moment of inertia and PEM volume counteract with each other to result in an operating line closer to the ideal one, while in the case of pressure increase, the effects accumulate and lead to an even greater deviation from the ideal operating line.

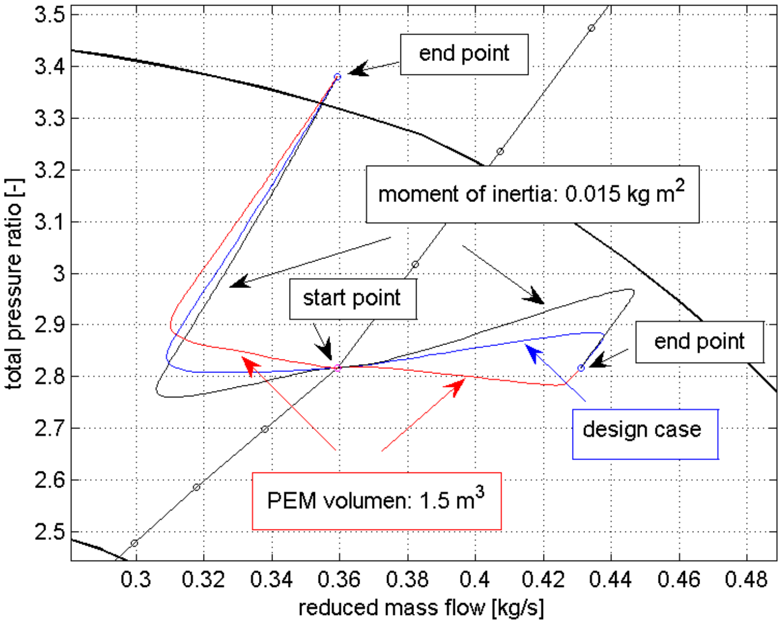

Fig. 53 System response for a cathode mass flow and pressure increase

The response time is defined as the time when 95 % (three time constants) of the desired set point change is reached. It is plotted in Fig. 54 and Fig. 55 as a function of the rotor moment of inertia and the PEM volume for each operating point change scenario. For both increased PEM volume and moment of inertia, response time is increased. Cathode mass flow response time is around 1 sec and increases with rotor moment of inertia but is less sensitive to increased PEM volume, which is an important fact for the subsequent mass flow response optimisation.

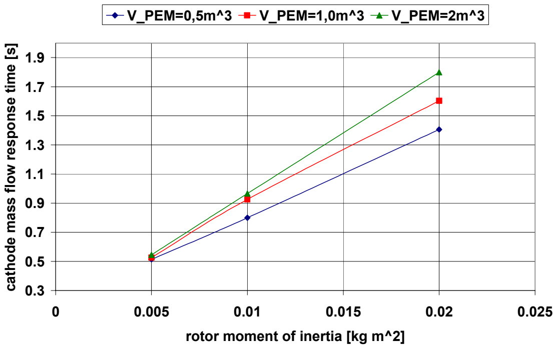

Fig. 54 Cathode mass flow response time of the turbocharger section

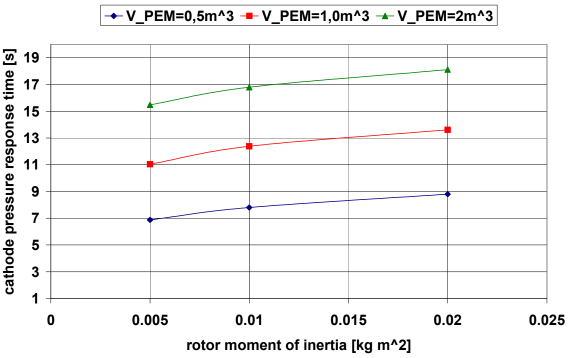

Fig. 55 Cathode pressure response time of the turbocharger section

For a pressure increase, the results are inverted. The system response is increased by a factor of two when the PEM stack volume is tripled in size. The mean response time is at about 10 sec and is a magnitude higher than the response time for the mass flow increase, which is mainly due to the compressor and turbine characteristics. While in the pressure increase scenario the electric power remains almost constant, the electric power to the compressor motor is significantly increased for the mass flow increase scenario to overcome the pressure losses and the lowered efficiency parameters in the compressor and the turbine. The additional compressor power to the system therefore leads to quicker responses than observed when solely the guide vane position is adjusted.

As expected, the open-loop system response is dependent on the energy storage, e.g. the system volume and the rotor moment of inertia. Minimising these parameters for advanced system design is favourable for improving the system response but with a different effectiveness. For improving the mass flow response characteristics, the PEM volume plays a minor role. A decrease of rotor moment of inertia improves mass flow response significantly, which should be incorporated early in demonstrator design. System behaviour is changing considerably when a (feed-back) controller is applied. Therefore the present analysis will be extended to a fully controlled system including the reformer air compressor.

6.2 Controller Requirements and Controller Architecture

Based on the current understanding of the system it is assumed to be a too great step to design an integral controller for the reformer section, the FC cooling management, the air supply, and the power management. Moreover, the present strategy to apply detailed aerodynamic models instead of transfer functions would clearly increase the integration effort. The controller architecture is limited to the air supply components but designed to fit into a hierarchical FC power unit controller. Mass flow and cathode pressure are then input variables to the air supply controller. These might be controlled by a superior controller or optimisation procedure to find the overall optimum operating point for the FC power unit.

The primary control requirement of the air supply system is to provide a required mass flow at a specified pressure. Among these two targets, the mass flow control is considered to be most important because it affects the stack cooling and the stoichiometry at the membrane. Pressure changes should be made rather smoothly to avoid additional mechanical stress between the anode and the cathode side but might be considered for achieving an increase of stack efficiency or operating range.

The present air supply represents a two-input-two-output problem, where the inlet guide vane position at turbine inlet (u_1) and the electric support (u_2) are the setting parameters and the compressor outlet pressure (y_1) and the mass flow through the compressor (y_2) are the controlled variables. This is also true for the reformer air compressor, where the electric motor power and back pressure valve set the mass flow and the reformer inlet pressure, respectively. For this purpose, two independent controllers are proposed. Each controller is divided up into two independent single-input-single-output (SISO) sub-controllers controlling one variable.

In order to determine the global issues related to the actuator topology, the control design will assume perfect measurements of the performance variables. Electrical actuator dynamics are neglected because they are considered to be more than a magnitude faster than pneumatic system response time. The inlet guide vane exhibits a fast first-order behaviour while the back-pressure valve at the reformer air compressor is slower by a factor of 5.

6.3 Input-Output Pairing

The responses of the output to step changes in the actuator signals show a coupled and anisotropic system (Fig. 53), because the mass flow responds faster than the pressure. It is of interest now which setting variable has to control which variable for the turbocharger section and the reformer compressor, respectively, in order to have least interaction and thus best controller performance. A wrong choice of the input-output pairing can lead to poor controller performance with great control action. At high coupling of the wrong pairing, the system can become unstable and uncontrollable even though the uncontrolled system has negative eigenvalues. A method used to measure the interaction and assess appropriate pairing is called Relative Gain Array (RGA), as presented in e.g. Bequette, B.W. (2007), where

$$\mathrm{RGA}(G) = G \times \left(G^{-1}\right)^{T} = \begin{pmatrix} \lambda_{11} & \lambda_{12} \\ \lambda_{21} & \lambda_{22} \end{pmatrix} = \begin{pmatrix} \lambda_{11} & 1-\lambda_{11} \\ 1-\lambda_{11} & \lambda_{11} \end{pmatrix} \qquad \text{Eq. 6-1}$$

and

$$\lambda_{ij} = \frac{\left(\dfrac{\partial y_i}{\partial u_j}\right)_{u_k\ k\neq j}}{\left(\dfrac{\partial y_i}{\partial u_j}\right)_{y_k\ k\neq i}} . \qquad \text{Eq. 6-2}$$

Each element of the RGA matrix indicates the interaction between the corresponding input and output pair. It is preferred to have a pairing that gives an RGA matrix close to identity matrix, resulting in minimum interaction with the input-output pairs which are not trace elements of the RGA. This means that control actions of the designated setting variable has maximum impact on the desired control variable and has least influence on all other control parameters. The RGA of the turbocharger section is

$$\mathrm{RGA}(0\ \mathrm{rad/s})_{\mathrm{turbocharger}} = \begin{bmatrix} 1.78 & -0.78 \\ -0.78 & 1.78 \end{bmatrix}, \qquad \text{Eq. 6-3}$$

which leads to a pairing choice of (inlet guide vane) – (compressor outlet pressure) and (TC drive power) – (compressor mass flow) to avoid instabilities at low frequencies as it is true for the step function scenario. The RGA for the reformer air compressor is

$$\mathrm{RGA}(0\ \mathrm{rad/s})_{\mathrm{reformer\ compressor}} = \begin{bmatrix} 0.82 & 0.18 \\ 0.18 & 0.82 \end{bmatrix} \qquad \text{Eq. 6-4}$$

and suggests the best pairing choices to be (backpressure valve) – (reformer compressor outlet pressure) and (electric demand) – (reformer air compressor mass flow).

Due to the varying operating altitude of the aircraft and the non-linearity of the system characteristics, the RGA for the turbocharger section is not constant over the altitude range as depicted in Fig. 56. It shows that the operating point at 6000 m exhibits the maximum coupling for this pairing choice, which represents therefore a good starting point for the controller design. At higher altitudes, the coupling drops to values around unity, increasing the controller performance. This coincides well with the long operating time of the power unit at these altitudes.

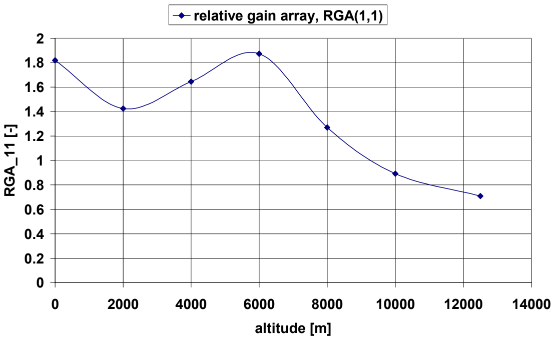

Fig. 56 RGA for the turbocharger section as a function of the operating altitude

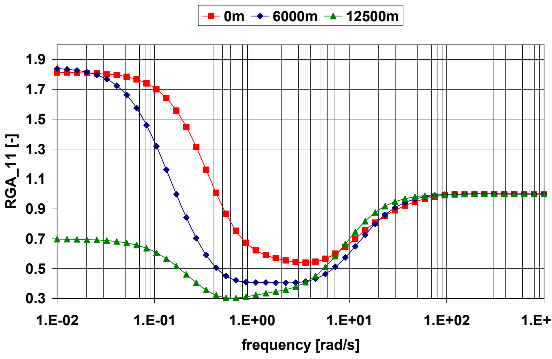

Fig. 57 Frequency dependent RGA of the turbocharger section at 6000m

The controller performance can drop significantly in performance during quickly varying control demands or frequency disturbance due to measurement noise, even if the controller show good results for the step analysis. A frequency analysis of the turbocharger section at different operating altitudes (Fig. 57) shows that the coupling decreases at high frequencies at low to mean altitudes. The coupling at cruising altitude increases slightly with higher frequencies but the RGA reaches again unity, which confirms the pairing choice and allows the assumption that the proposed controller architecture is able to attain the desired control actions at a reasonable performance.

6.4 Coupled and Decoupled Single-Input-Single-Output (SISO) Control Approach

As outlined above, two independent SISO controllers have been designed for the air mass flow and compressor pressure, respectively. They are analysed for a mass flow and a pressure increase, Fig. 59, p.81. While the mass flow increase causes only slight deviations in compressor pressure ratio, the pressure increase changes the mass flow strongly towards surge margin. This can cause a critical operating condition, especially for demands of high pressure increase at low altitudes, where the design operating line is moved to surge. A trespassing of the surge line would lead to compressor surge and thus a complete break-down of mass flow which must be avoided. For the opposite scenarios (mass flow or pressure decrease, not shown here) the response characteristics are almost symmetric and therefore not critical to the compressor.

An increase in pressure output of the compressor would surely not be accomplished in a step change but in a much slower process because abrupt pressure fluctuations at the cathode inlet or asymmetric pressure differences across the membrane due to the pneumatically longer anode and gas processing path are not desirable. Nevertheless, the step change represents a worst-case scenario for the compressor and is used as starting ground in order to improve controlled system dynamics. For a coupled controlled system, the introduction of a decoupler is a common step to improve overall controller performance (Bequette, B.W. (2007) and Föllinger, O. (1990)). It can be regarded as an “intermediately-installed” controller minimising or eliminating the undesired control action evoked by the system-controller interaction. The basic decoupling architecture is given in Fig. 58.

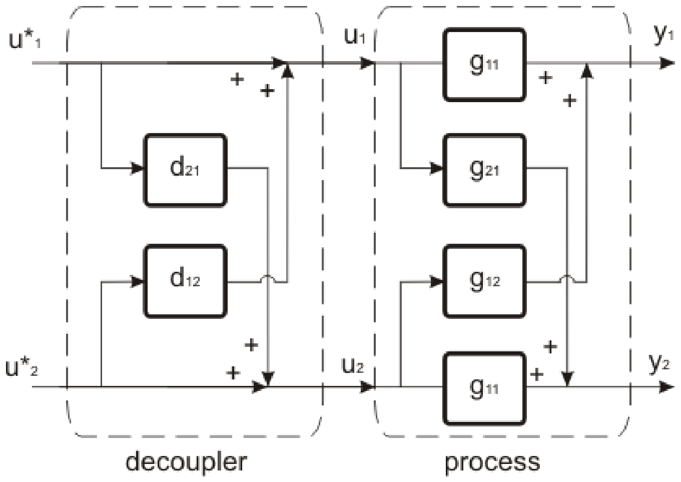

Fig. 58 Controller architecture including a simplified decoupler

Therefore, a synthetic input vector is introduced. The relationship between the synthetic input vector and the process output vector is

$$y(s) = G_p(s) \cdot D(s) \cdot u^*(s) \quad , \qquad \text{Eq. 6-5}$$

where D(s) represents the decoupling matrix and $G_p(s)$ the process transfer matrix. For a simplified decoupling strategy, D(s) remains restricted to

$$D(s) = \begin{bmatrix} 1 & -\frac{g_{12}(s)}{g_{11}(s)} \\ -\frac{g_{21}(s)}{g_{22}(s)} & 1 \end{bmatrix} \qquad \text{Eq. 6-6}$$

when the decoupler is expected to operate ideally. The synthetic process matrix is then

$$\begin{aligned} G_p^* = G_p(s) \cdot D(s) &= \begin{bmatrix} g_{11}(s) & g_{12}(s) \\ g_{21}(s) & g_{22}(s) \end{bmatrix} \cdot \begin{bmatrix} 1 & d_{12}(s) \\ d_{21}(s) & 1 \end{bmatrix} \\ &= \begin{bmatrix} g_{11}^*(s) & 1 \\ 1 & g_{22}^*(s) \end{bmatrix} \end{aligned} \qquad \text{Eq. 6-7}$$

where

$$g_{11}^*(s) = g_{11}(s) - \frac{g_{12}(s) \cdot g_{21}(s)}{g_{22}(s)} \qquad \text{Eq. 6-8}$$

and

$$g_{22}^*(s) = g_{22}(s) - \frac{g_{21}(s) \cdot g_{12}(s)}{g_{11}(s)} \quad . \qquad \text{Eq. 6-9}$$

Here, the decoupler is calculated with the process transfer matrix obtained from the system model which is linearised at 6000 m and at the design stack operating point. Similar to feed-forward controller design, right half plane poles can occur in the decoupler matrix when positive zeros are present in the process transfer matrix. Therefore they are factored out and replaced by low-pass filters. This also assures retaining a physically feasible controller, which requires a denominator of a higher order than of the numerator. In the case of static decoupling, the decoupling matrix does not consist of transfer functions based on the linearised models but of constants which are obtained by setting the transfer matrix to s=0. Static decoupling represents a simple strategy and decreases controller performance but it is often used in practice, especially if the dynamic parameters are uncertain as it may be expected for the demonstrator phase. It will therefore be included in the controller assessment.

The results for the independent SISO and the statically and dynamically decoupled controllers are given in Fig. 59, where the operating lines are depicted in the compressor map. Again, a severe deviation in compressor mass flow towards surge can be observed during the step pressure increase. The deviation can be significantly reduced by static decoupling and almost eliminated with dynamic decoupling. This is also true for the step mass flow increase resulting in a slight pressure loss throughout the operating point change. Basically, no overshoot or oscillation occur during the transients, which can be confirmed also for an arbitrary choice of mass flow and pressure change for each controller type.

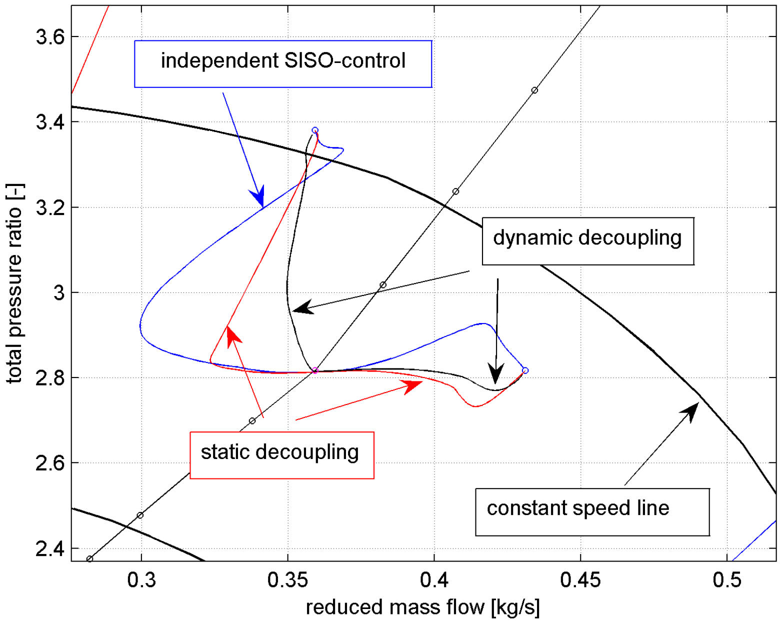

Fig. 59 System response for the independent and decoupled SISO-control during a cathode mass flow and pressure increase

For the present mass flow increase analysis, both the mass flow in the turbocharger and the reformer compressor are increased, because it is assumed for simplification that a stack power increase will cause a higher mass flow on the anode and cathode side. Applying the dynamic decoupler during the step mass flow increase of 10%, the desired compressor mass flow is reached after one second, which is assumed to be satisfactory, while the deviation of the pressure at the compressor outlet remains below 1% of the demanded pressure value (Fig. 60).

The actuators show reasonable dynamics. Small overshoots are shown in Fig. 61 for the dynamically decoupled controller type for the turbocharger section and the reformer air compressor, respectively. Note that the turbocharger changes from a power generating to a power consuming device in order to overcome the rising pressure losses. The power peak is at approx. twice the power increase needed for the steady-state operating point change. At 4 kW, it is low when compared to a 80 kW stack power output.

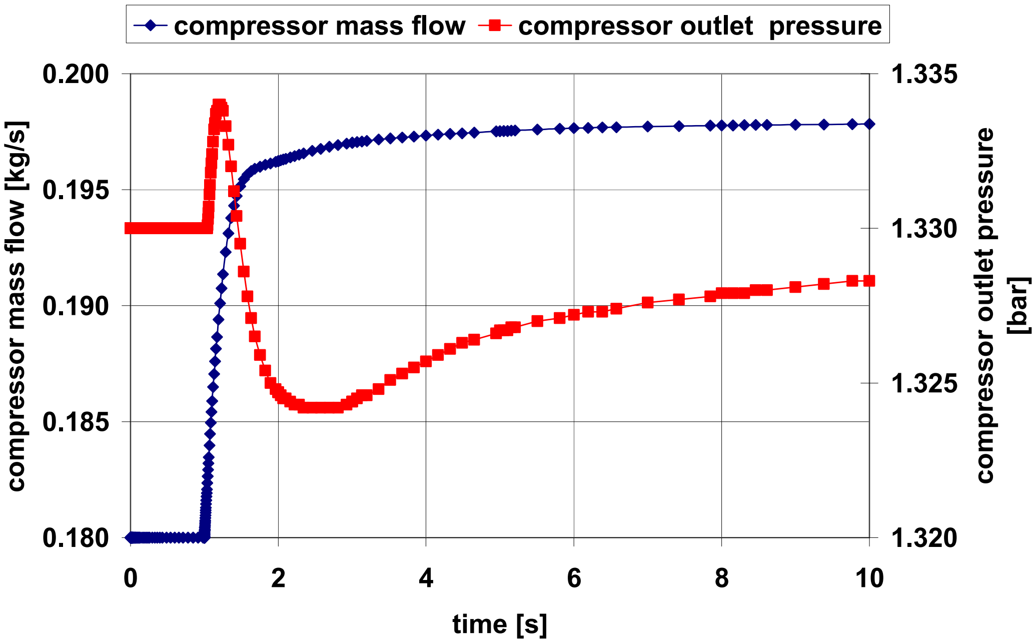

Fig. 60 Compressor mass flow and outlet pressure response for a mass flow increase at 6000m

It is left to a future analysis, to which degree the overall power management can absorb such power peaks without destabilising the power system or violate control demands. A ramp or polynomial set point function or the implementation of a low-pass filter would clearly smooth the power peak but also have a negative impact on response time.

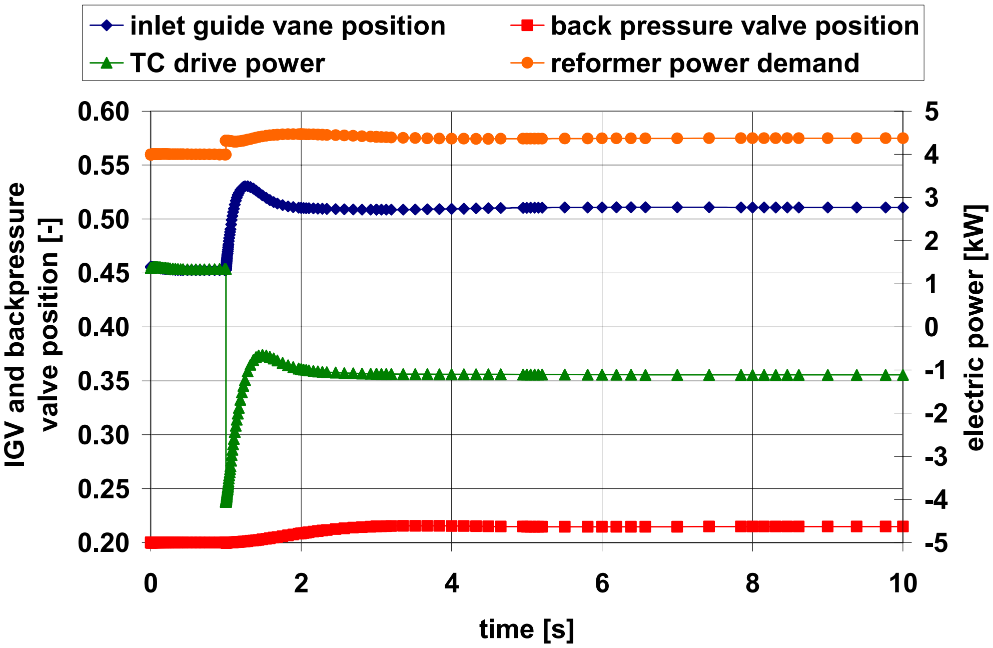

Fig. 61 IGV, valve position, and electric power demand during a mass flow increase at 6000m

The actuator dynamics of the downstream reformer air compressor are relatively slow due to the slow temperature and pressure change at the turbocharger compressor and the demanded higher reformer air mass flow. It is clear that these dynamics are highly dependent on the control quality of the turbocharger controller situated upstream. They remain however still uncritical even if the turbocharger section is controlled with the independent SISO controller type.

6.5 Validity of the Decoupled SISO Controller for the Entire Altitude Range

It is one important requirement for the controller that it must cover the entire altitude range. Therefore, the thorough analysis is performed with the non-linear models of the system.

Due to the strong non-linearity of the compressor and the turbine maps, it has to be investigated how the controller performs at altitudes different from the controller design altitude of 6000 m. The compressor mass flow change for a step increase at 0 m, 6000 m and 12000 m altitude and the dynamically decoupled controller type are shown in Fig. 62.

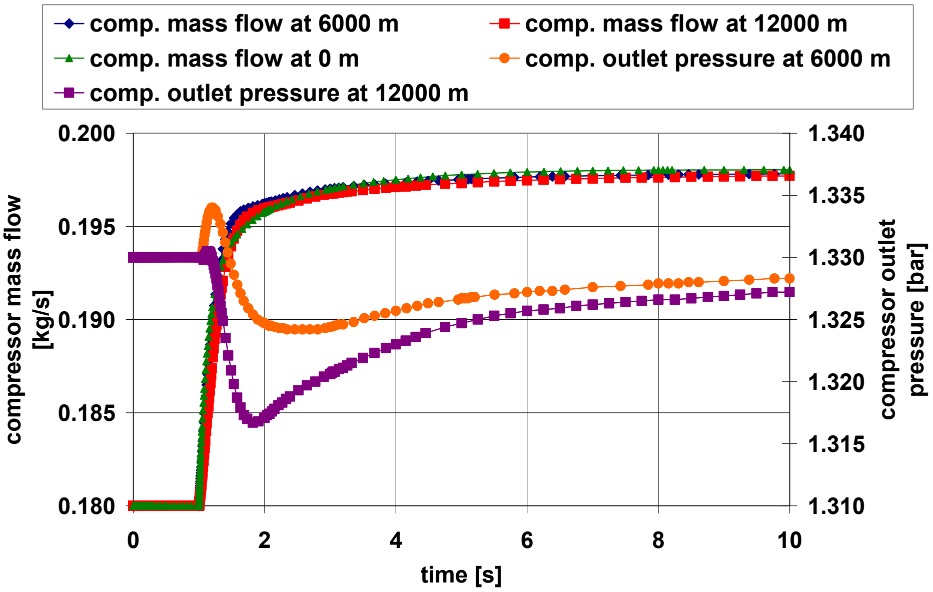

Fig. 62 Compressor mass flow and outlet pressure response for a mass flow increase at different operating altitudes

The mass flow curves lay close together while the corresponding pressure curves deviate slightly from each other, which is still satisfactory. The pressure curve for 0 m is also similar but is found at a higher pressure level due to increased cathode pressure at low altitudes. This can be also confirmed for an arbitrary choice of set point change. Therefore the controller type proposed proves to be valid and shows good performance for the entire altitude range.

6.6 Multiple-Input-Multiple-Output, Linear-Quadratic-Gaussian Control Approach

A relatively modern controller design approach for the feedback state controller is the linear quadratic gaussian (LQG) controller where the control action is based on a quadratic performance criterion. The LQG controller minimises this cost criterion, optimises the control action and enables to trade off regulation performance and control effort. LQG control technique is often applied in aviation and space applications where the minimisation of control action plays a significant role (see Föllinger, O. (1990)). It is based on a state feed-back control approach where the system is fully controllable by the state vector and the state feedback gain K. The state feedback controller represents therefore a proportional controller in the feed-back loop. With a model of the form

$$\begin{aligned} \dot{x} &= A \cdot x + B \cdot u \\ y &= C \cdot x + D \cdot u \end{aligned} \qquad \text{Eq. 6-10}$$

where u is the vector of control inputs, x is the state vector, and y is the vector of measurements, and the control law

$$u = -K \cdot x \qquad \text{Eq. 6-11}$$

the closed loop dynamics are given by

$$\dot{x} = (A - B \cdot K) \cdot x \,. \qquad \text{Eq. 6-12}$$

The closed loop poles are the eigenvalues of (A-B·K). In a “classical” state-space controller design, it is possible to define K in a way that the eigenvalues provide the desired control performance. For the LQG approach, the regulation performance is measured by the quadratic criterion of the form

$$J(u) = \int_0^\infty \left\{ x^T \cdot Q \cdot x + 2 \cdot x^T \cdot N \cdot u + u^T \cdot R \cdot u \right\} dt \,. \qquad \text{Eq. 6-13}$$

Q, N, and R are the weighting matrices of the state variables, the input variables and their combination, respectively, and are user specified. The first design step seeks a state-feedback law according to Eq. 6-11 that minimises the cost function J(u). The minimising gain matrix K is called the LQ-optimal gain and is obtained by solving the associated algebraic Riccati equation in S:

$$0 = A^T \cdot S + S \cdot A - \left(S \cdot B + N \right) \cdot R^{-1} \cdot \left(B^T \cdot S + N^T \right) + Q \qquad \text{Eq. 6-14}$$

K is derived from S by

$$K = R^{-1} \cdot \left(B^T \cdot S + N^T \right) \qquad \text{Eq. 6-15}$$

and can be obtained from the function library available in Matlab. For further analytical insight and limitations of this mathematical procedure see Ludyk, G. (2001) and Föllinger, O. (1990).

The here presented control task of the air supply system requires four control variables, these are mass flow and output pressure at the main compressor and the reformer compressor, respectively, and therefore four setting parameters which results in a 4x4 MIMO-problem. For the state-space controller, the controller cannot be designed independently as done with the SISO controller approach, but has to be undertaken in a fully integral design step, where all input and output variables are controlled by one matrix. Generally, this procedure increases control performance for coupled systems but increases on the other hand controller design effort. The main objective of the LQG approach is not to increase control performance as this has been proven well by the decoupled SISO strategy but rather to show the potential to minimise the control effort for the same control quality when compared to the results presented in Section 6.4, p.79.

A comparison between the system response for the dynamically decoupled SISO and LQG control approach is shown in Fig. 63 and Fig. 64 for the main compressor and the reformer compressor, respectively. It can be recognised that control performance is slightly increased for the main compressor. The pressure fluctuations at the reformer compressor are even significantly reduced, also well seen in Fig. 67, while the mass flow response is good.

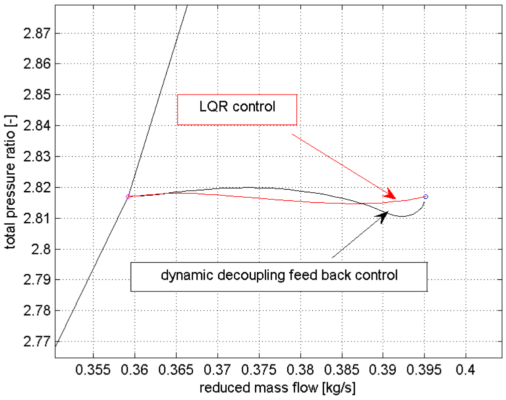

Fig. 63 Comparison of the TC section response for the dynamically decoupled SISO and the LQG control

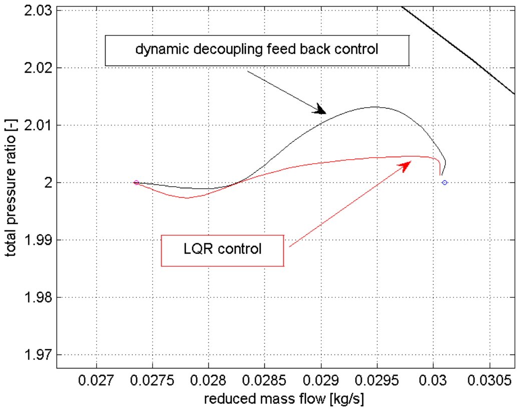

Fig. 64 Comparison of the reformer compres. response for the dynamically decoupled SISO and the LQG control

An overview of the mass flow and pressure response characteristics is given in Fig. 65 and Fig. 67 for the main compressor and the reformer compressor, respectively. For reasons of comparability, both controllers are tuned in a way that the mass flow response is almost identical.

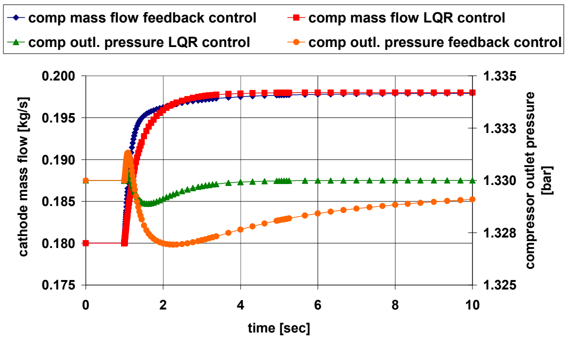

Fig. 65 Comparison of the TC section response for the decoupled SISO and the LQG control

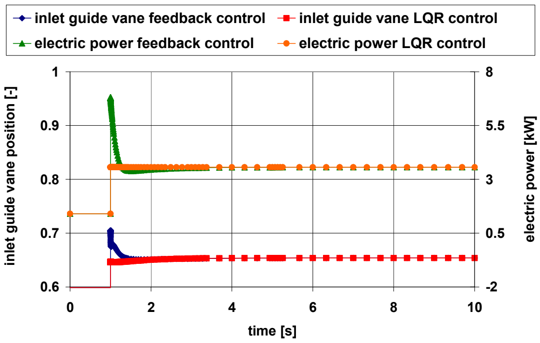

Fig. 66 Comparison of the control action for the TC section for the decoupled SISO and the LQG control

It is well shown in Fig. 66 and Fig. 68 that actuator dynamics are significantly reduced with the LQG approach while the control performance is similar or even better as for the pressure output.

Especially the power peaks are eliminated which is a clear advantage for the fuel cell power management. The setting variables show a characteristic which might be expected from the open-loop control but with the quality of full feed-back control architecture. This makes the LQR control approach an interesting control strategy for this application.

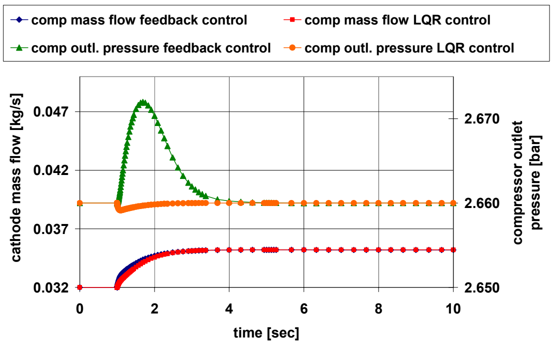

Fig. 67 Comparison of the reformer compressor response for the decoupled SISO and LQG control

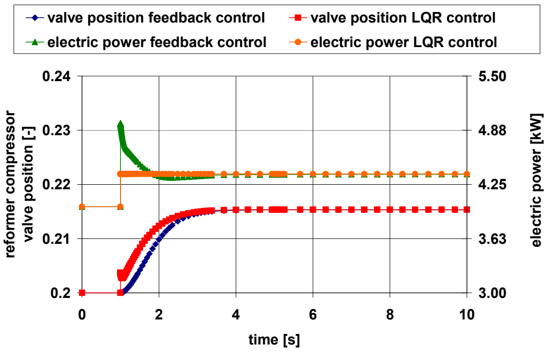

Fig. 68 Comparison of the control action for the reformer compressor for the decoupled SISO and the LQG control

For a successful use and final evaluation of this control architecture, though, further design effort is necessary. The state-space controller is based on the fact that all state variables are known in order to allow a full feed-back of all state variables. As this is often not possible for technical systems, a state estimator has to be introduced to guess the state space vector from the available measurement. This state estimate is generated by the Kalman filter which also considers system disturbance and measurement noise. It is an optimal estimator dealing with Gaussian white noise, which minimises the asymptotic covariance of the estimation error based on the covariance data. The Kalman gain L is again determined through an algebraic Riccati equation. For the final design, the LQ-optimal gain K and the Kalman filter have to be designed in one integral step resulting in a LQG regulator, see Fig. 69.

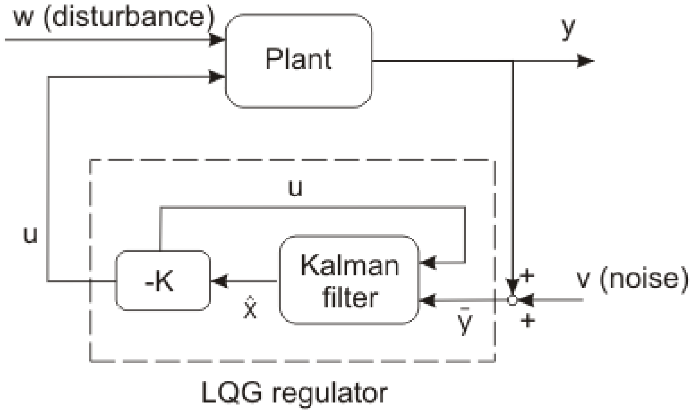

Fig. 69 State-space controller including a LQG regulator

It is further important to mention that the presented results are only valid for the simple PEM FC model, which keeps the design effort reasonable. The use of the highly detailed stack model and the associated differential equations, and thus further states, increases the system matrix size significantly, which might make system reduction strategies necessary. As these steps go deep into the domain of control theory and application and entail a separate field for analysis and evaluation, the LQR control approach is not further pursued in this work.

6.7 Validation of the Control Architecture and Tuning with an Advanced PEM Model

In the last section of this chapter, a final comparison between the application of the simple and the highly detailed PEM-FC model and its influence on the pneumatic performance shall be drawn. For model stability and calculation time reasons, a highly simplified model on the cathode but also the reformer path has been used. It is not accounting for any dynamic phenomena or interactions between the partial oxygen pressure and electrochemical performance. Stack power has been set constant for both model types to ensure comparability.

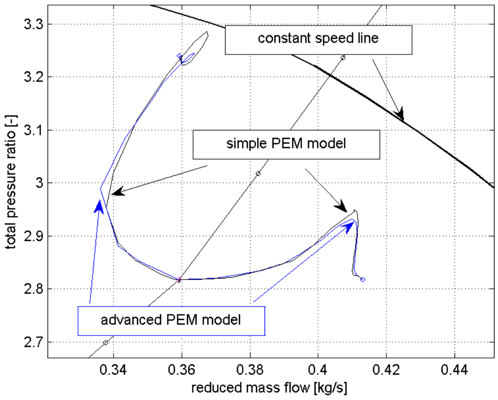

Fig. 70 Comparison of the system response for the simple and the advanced PEM-FC model

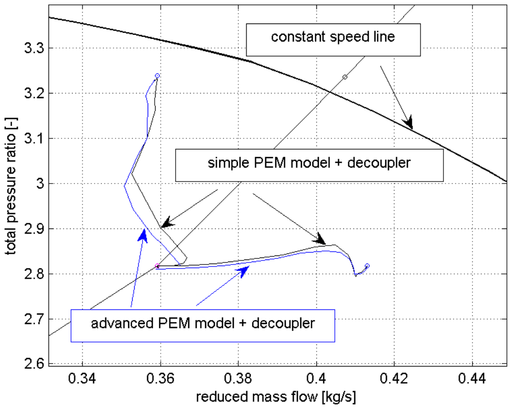

Fig. 71 Comparison of the system response for the simple and the advanced PEM-FC model applying the decoupled controller

Again, a cathode mass flow and pressure increase is investigated for the simple SISO control architecture. It can be seen in Fig. 70 that system response is very similar for both models with a small overshoot which can be recognised for the pressure increase and the detailed PEM-FC model. The results for the decoupled scenario (Fig. 71) show also good agreement but are obtained with a recalculated decoupling matrix. This is necessary to avoid steady offset as the transfer matrices of the different models are not the same.

The strategy to design the air supply control architecture on a simple FC model is proven to be a good choice for fast controller development and assessment. The combination with the highly detailed and calculation-time consuming model can be left to a last model integration step where the controller has only to be slightly tuned.

7 Response Analysis Using an Advanced PEM-FC Model

In the last chapter, a fully dynamic investigation is undertaken to prove the theoretical models under in-flight conditions. The system response is optimised considering all aspects of cathode turbomachinery design, cathode pressure strategy, and controller design.

7.1 System Behaviour during PEM-FC Step Load Scenarios

It can be expected that a new free parameter, the stack current, imposes changes in system response as the composition of the anode off-gases change significantly. The system response during a step increase of the stack current of 20% and 30% starting from the design power output is given in Fig. 72. The current increase is limited by a maximum hydrogen utilisation of around 0.9. This is when further hydrogen available in the anode channel cannot be transported to the membrane due to diffusion losses. The local current then becomes zero. It can be seen that overall system response remains good. However, pressure deviations grow stronger and the cathode mass flow response becomes more sluggish, especially for the high stack current increase (see also Fig. E-1and Fig. E-2, p.128).

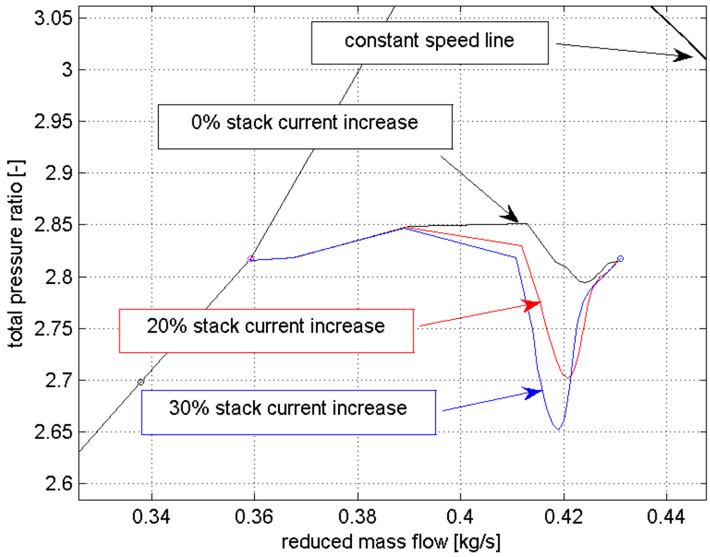

Fig. 72 System response as a function of the stack current increase

After the stack current change, the calorific values of the stack off-gas decreases, which again leads to decrease of TIT. The additional power lack has to be compensated by a higher supporting power from the electric net, which is unfortunate during the higher output demand from the stack.

7.2 System Behaviour during PEM-FC and Reformer Step Load Scenarios

It is realistic that the reformer performance will also be increased in case of a higher stack power demand. A small time delay has to be expected from the reformer until it has reached the demanded hydrogen production while the changed operating conditions are again delayed by the gas cleaning devices. Here, the cathode air, the stack current, and the reformer output performance are increased by 20%, which would maintain the air utilisation constant.

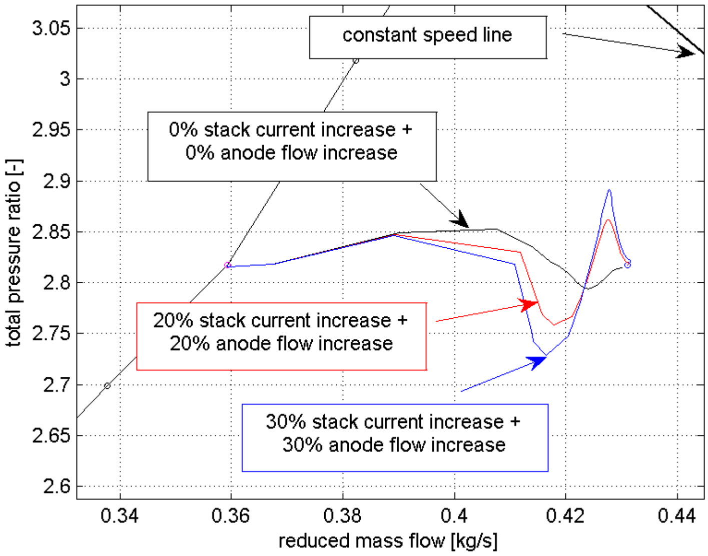

Fig. 73 System response as a function of the stack current and reformer performance increase

System response for these scenarios is again acceptable as seen in Fig. 73, while the sluggishness of the mass flow response is eliminated to the highest degree (Fig. E-3 and Fig. E-4, p.129). This can be explained by the more uniform composition of the cathode off-gases and therefore the TIT response, which consequently decreases the necessary control action to achieve the required mass flow.

7.3 Extended Operational Flexibility by Advanced Cathode Pressure Function and Turbine Design

In order to demonstrate the considerations of how to improve operational flexibility and system response, an extreme operating scenario is examined where the cathode mass flow is increased by 50% at an operating altitude of 6000 m. As the desired operating point is highly power consuming because of a disadvantageous compressor efficiency and high compressor mass flow, it is not a recommended operating scenario. It shows however the capability of the controller to cover even operating scenarios far aside from the design point.

In a first scenario, the reformer performance and stack current will be increased by 25%, which keeps the hydrogen utilisation at moderate parameters. When increasing the cathode mass flow by the same value of 25% (see Fig. 74), the inlet guide vane position reaches an opening ratio of 0.78 which is close to the maximum, illustrating that the upper limit for the mass flow is nearly reached.

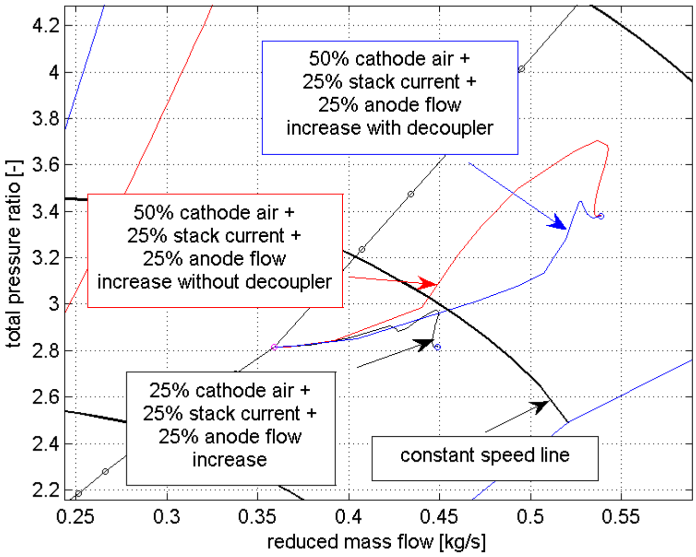

Fig. 74 System response during an extreme operating scenario with an adjusted turbine design, an advanced cathode pressure function, and the application of a decoupled controller

In the second scenario depicted in Fig. 74, the cathode air is increased by 50% while the compressor outlet pressure is raised from 1.33 bar to 1.6 bar in order to allow a higher mass flow through the turbine. The decoupler is not applied yet. As a result, the guide vane position reaches the end operating point with an opening ratio of 0.77. Pressure is slightly fluctuating and exhibits a small overshoot in the range of 9% of the end value while the mass flow end value is reached rather sluggishly (Fig. E-5 and Fig. E-6 p.130). Nevertheless, system response is stable and the desired mass flow is settled after 2 s. In the last scenario, the decoupler is activated which has the result that the mass flow has reached its end point approximately after 1 s. The desired pressure value is reached after 2 s instead of 5 s as without the decoupler (Fig. E-5 and Fig. E-6 p.130). Basically, no overshoot occurs as can be well seen in Fig. 74.

7.4 System Behaviour during Typical On-board Load Scenarios

In the last analysis of this work, it shall be demonstrated that the developed model and the turbomachinery design allow for both operation throughout a typical flight envelope based and highly fluctuating power demands at any operating altitude. Based on a load demand from a more electric aircraft, a complete envelope is calculated with the presented models and the controller. It is assumed that a strong power demand change occurs at cruising flight conditions. This might be the case during break-down of redundant power units or during unexpectedly simultaneous high power demands from different power consumers.

The here investigated load demand of the PEM-FC is shown in Fig. 75 in a normalised form. It shows a steep demand increase during the climb phase, drops quickly during cruising flight, and then drops slowly during the descent phase to a value of 0.8.

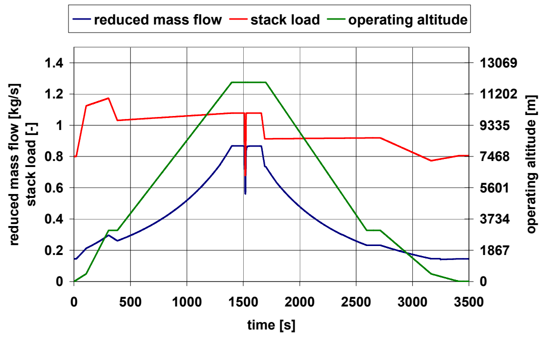

Fig. 75 Load demand, reduced mass flow and operating altitude for the reference flight envelope

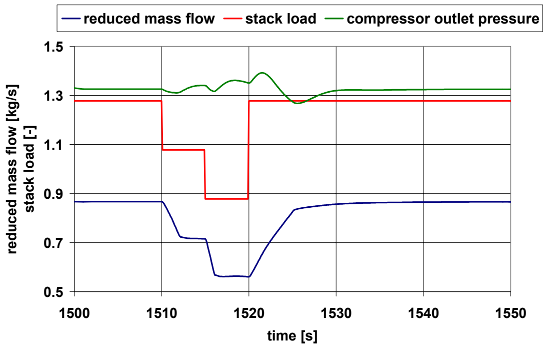

Fig. 76 Load demand, reduced mass flow and operating altitude for the load change at cruising flight conditions

During cruising flight, the power demand and the mass flow are decreased in two steps by 15% points, respectively. Finally, it is increased again to the starting value by one step, which is shown in Fig. 76 in a zoomed time range. For the last load step, this represents an increase of over 50% of the stack current and the cathode mass flow, respectively, as the air utilisation is tried to be kept constant.

The compressor line of the entire envelope of operation is given in Fig. 77, which summarises all preceding results in one illustration. The blue section represents the climb phase and is located to the right of the design mass flow due to the stack demand. The stagnation of the aircraft at intermediate altitudes and a decrease of power demand cause a sharp bend at low shaft speeds.

It can be seen that the power demand steps at the cruising altitude are handled well by the controller architecture. Note that even if the compressor line seems to deviate strongly in the compressor map, the real pressure fluctuation at the compressor outlet remains low within a range of 5% of the output value, see Fig. 76, which can be explained by the high pressure ratio at cruising flight conditions. It can be therefore stated that cathode pressure fluctuations remain low for the controlled system which was a design requirement for the air supply in combination with the PEM-FC. Power demand is decreased at cruising flight altitude shifting the compressor line left of the design mass flow. During the descent phase, the system reaches the operating point at ground level safely and with sufficient distance from the surge margin.

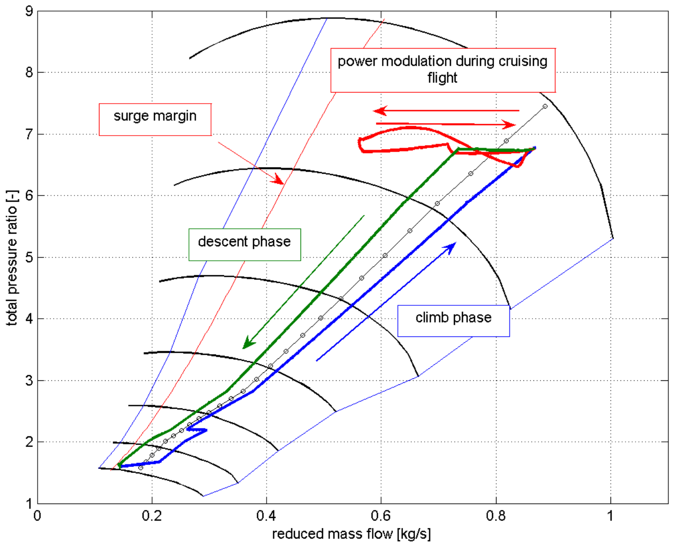

Fig. 77 System response during a typical on-board load scenario for the entire envelope

It can be seen from Fig. 77 that air utilisation should be adjusted. At low operating altitudes, operation in the compressor map occurs close to the surge margin which does not leave room for further mass flow variations or control actions. A higher mass flow would be desirable and simultaneously increase air utilisation. At high altitudes, the air supply operating point is rather to be shifted towards the surge margin in order to decrease the external air supply power demand and thus increase overall performance.

8 Conclusions

An air supply system on the basis of radial turbomachinery for the in-flight PEM-FC is shown to be technically feasible. The use of radial compressors is found to be a suitable compressor technology. Due to the requirement of a constant compressor mass flow and outlet pressure at every altitude, the compressor can be operated close to its design flow and head coefficient over a wide range of the operating altitude. This aerodynamic similarity points to an operation with high isentropic efficiencies and sufficient margin from aerodynamic operating limits. Transonic inducer design is omitted to keep design and manufacturing sophistication reasonable. Based on the present performance models, the decision between single-stage and two-stage compressors can be made in favour of the two-stage concept due to the higher overall isentropic efficiency of around 10% with a pressure ratio of 7.5. Optimum compression performance is obtained when the first compressor has a pressure ratio of 2.75. Driving the compressor with a turbine is found to be essential for the decrease of the power demand of the air supply system. The option of additional combustion of kerosene eliminates the demand of external electric power but is burdened with poor efficiencies. It is therefore not sensible for long-term operation but an option for fast transients.

An improvement of overall performance is obtained if the cathode pressure is adapted to the operating altitude. The power demand of the air supply system is minimised when the cathode pressure is gradually increased up to 1.6 bar at intermediate operating altitudes. Further potential for decreasing the power demand is found if special attention is paid to the design of the turbine section. The air supply system turns into a power generating device throughout a broad flight altitude range if the isentropic turbine efficiency is increased up to 0.8. The additional power is in the range 10% of the FC power output but imposes higher complexity on the power management of the FC power unit.

In order to further optimise mass flow range and power demand, both the pressure loss characteristics of each device on the cathode path and the turbine design have to be addressed early during component design and development, e.g. an increased cathode pressure loss of 0.2 bar reduces the possible operating range of high mass flows by one half. An unexpected advantage is obtained when the turbine is designed too big with a mass flow of 20% higher than the design PEM-FC outlet mass flow. The mass flow range is then increased by approximately 20% without any deteriorating impact on the power demand of the air supply system.

Unlike in current modelling strategies, the transient analysis has been based on the sequential arrangement of pneumatically interacting lumped volumes. It is found to be an essential model for approaching real physical behaviour. The system shows anisotropic transient behaviour due to the non-linear compressor and turbine characteristics. Mass flow response is inherently stable and fast, while pressure response tends to be rather sluggish. Abrupt pressure increase in particular has to be avoided, as compressor mass flow might fall below the surge margin. Inherent system dynamics can be improved by minimising the system plena and the moment of inertia of the turbocharger.

The simple but reliable control strategy of applying SISO controllers allows the integration into a hierarchical FC power unit controller. While the control performance is good for the mass flow increase, the system response exhibits strong deviations towards the surge margin when pressure is increased abruptly. The application of a decoupled controller significantly minimises the coupling effect with an improved ability to follow set points both for pressure and mass flow. Rise times are around 1 s with no overshoot or oscillations for a step set point change while actuator dynamics remain reasonable. Although the decoupling matrix is obtained from one linearisation point, the controller architecture proves stable and shows good performance for the entire flight envelope. This is an important result considering the highly non-linear system characteristics. It can be further stated that the strategy to develop a controller with an adaptive modelling depth with emphasis rather on pneumatic and aerodynamic than on electrochemical phenomena has proven to be effective. The replacement of the simplified PEM-FC model by a highly advanced one required only moderate controller tuning to restore almost identical controller performance.

The objective of this work is to demonstrate the significance of the appropriate turbomachinery design for the overall performance, which again has to be based on the comprehension of the overall system. The effectiveness of this methodology can be well demonstrated applying the most important considerations deduced from the conceptual analysis, the turbomachinery design, and the transient analysis in one extreme operating scenario: This is defined by a load increase of 50% at intermediate operating altitude and includes the corresponding cathode mass flow increase. The scenario can be calculated successfully without any critical or unstable operating conditions and with acceptable controller dynamics. It is important to point out, that neither the end point nor the quality of the transient would be achievable without the simultaneous application of the results from all analysis steps.

After integration with a highly detailed PEM-FC stack model, the air supply system and controller are finally confirmed to be suitable for the entire operating range. It is possible to cover the flight envelope from climb to end of the descent phase in a safe mode and with enough margin from the compressor surge line both for the standard and the future “more electric” power demand requirements of civil aircraft.

9 Outlook

In this work, the two-stage compression is favoured due to the higher isentropic efficiency. The extension to a transonic inducer design opens the full assessment of a single-stage compression. This clearly leaves state-of-the-art impeller design but approaches “classical” turbocharger arrangements and better satisfies the requirement for compactness. Reliable aerodynamic shock models then have to be introduced to the procedure, while special attention has to be paid to the interactions between the impeller and the diffuser section.

For the increase of operational flexibility, variable guide vanes upstream and downstream of the impeller are technically feasible options. They represent, on the other hand, a source of malfunction, whose impact has to be assessed carefully. A challenging option to increase the compressor operating range is to shift the stability line by prevention of surge. This can be done by the application of a blow-off valve or more sophisticated devices like active surge control. In order to evaluate the potential to further increase turbine power output, a full aerodynamic description of the turbine is necessary. Additional power from the air supply system has significant impact on the overall power management and increases the complexity of operating strategies and controls. The choice of the load share between the PEM-FC and the air supply system, on the other hand, allows further weight optimisation.

An important question to be investigated is how the FC system can manage peak load demands safely and with minimum electric power demand. One possibility is the application of a dual post combustor with the option of additional injection of kerosene. The challenge is to handle overall dynamics even though physical operating limits such as choke flow in the turbine section or air utilisation of the FC stack are reached. To minimise the control action during peak load demands will be a decisive key for successful overall integration. LQR controllers seem to satisfy this requirement, while they are already widely used in flight and space applications. Due to the strong non-linearity of the system, it remains however a non-trivial task to design the controller with adequate performance for the entire altitude range.

A last challenging but decisive task remains the full integration of the FC system with the electric network of the aircraft. The evaluation of the interactions between the electric consumers and the power generating device gives the last confirmation whether PEM-FC technology can meet the requirements of the civil flight application.

Bibliography

[1] Adamson, K-A. (2005): Fuel Cell Planes, Fuel Cell Today, 2005

[2] Angermann, A. (2004); Beuschel M.: Matlab – Simulink – Stateflow, Grundlagen, Toolboxen, Beispiele, 3. Auflage, Oldenbourg Verlag, München, 2004

[3] Aungier, R. H. (2000): Centrifugal Compressors: A strategy for aerodynamic design and analysis, ASME Press, New York, 2000, ISBN 0-7918-0093-8

[4] Baehr, H.D. (2002): Thermodynamik, Grundlagen und technische Anwendungen, Springer Verlag, Berlin, 2002, ISBN 3-540-43256-6-X

[5] Balje, O.E. (1981): Turbomachines, A guide to design, selection and theory, John Wiley & Son, New York, 1981, ISBN 0 471 06036 4

[6] Baines, N.C. (1998): A meanline prediction method for radial efficiency. IMechE, 6th International Conference on Turbocharging and Air Management Systems, Paper No. C554/006/98, London, UK, 1998

[7] Barchewitz, L. P. (2006): Design and Modelling of air supply systems for in-flight PEM-FC, GT2006-688, ASME TurboExpo, Barcelona, 2006

[8] Barchewitz, L. P. (2007): Dynamic Modelling and Controls of an Air Supply System for in-flight Proton Exchange Membrane Fuel Cells, GT2007-27900, ASME TurboExpo, Montreal, 2007

[9] Bequette, B.W. (2007): Process Control, Modelling, Design and Simulation, Prentice Hall, 2007

[10] Bernardi, D. M. (1992); Verbrugge, M. W.: A Mathematical Model of the Solid-Polymer-Electrolyte Fuel Cell. Journal of the Electrochemical Society, Vol. 139, No. 9, pp. 2477-2491

[11] Bireaud, B., Despierre, A. (2001): Simulation of the WR-21 Advanced Engine, ASME Turbo Expo, 2004-GT-0020, New Orleans, Louisiana, USA, 2001

[12] Mayer, M. (2003): Abgasturbolader, BorgWarner TurboSystems ‚Die Bibliothek der Technik, 103, Verlag Moderne Industrie, 2003

[13] Bundschuh, N. (2005); Bromberger K: Design and Simulation of SOFC Hybrid Systems for Aircraft Application: Investigation of different System Power and Architectural Integration, H2Expo –International Conference Fuel Cell Systems for Transportation, Hamburg, 2005

[14] Came, P.M., McKenzie, I.R.I. (1979): The performance of a 6.5 pressure ratio compressor having an impeller with swept-back blades, NGTE memorandum 79013

[15] Cunningham, J.M. (1999); Hoffman, M.; Moore, R.: Requirements for a Flexible and Realistic Air Supply Model for Incorporation into a Fuel Cell Vehicle (FCV) System Simulation, 1999-01-2912, Society of Automotive Engineers, 1999

[16] Cunningham, J.M. (2001): Air System Management for Fuel Cell Vehicle Applications, master thesis, University of California, 2001

[17] Daggett, D. (2003): Fuel Cell APU for commercial aircraft, presented at SECA Annual meeting 2003: www.netl.doe.gov/publications/proceedings /03/seca/DavidDaggett.pdf

[18] Daggett, D. (2005); Lowery, N.; Wittmann, J.: Fuel Cell APU for commercial aircraft, H2Expo –International Conference Fuel Cell Systems for Transportation, Hamburg, 2005

[19] Daily, J.W.; Nece, R.E. (1960): Chamber dimension effects on induced flow and frictional resistances of enclosed rotating discs, trans. ASME, Journal of Basic Engineering, Vol. 82, pp. 217-232, 1960

[20] de Jaeger, B. (1995): Rotating Stall and Surge Control: A Survey, Proceedings of the 34th IEEE Conference on Decision and Control, New Orleans, 2, 1857-1862

[21] Detallante, V. (2002); Langevin, D., Chappey: Kinetics of water vapour sorption in sulfonated polymide membranes. Desalination, Vol 148 (2002), pp. 333-339

[22] Eelman, S. (2003): High temperature fuel cells as substitution for the conventional APU in commercial aircraft, DGLR-JT-2003-183, Deutscher Luft- und Raumfahrtkongress 2003

[23] Eckert, B.; Schnell, E. (1980): Axial- und Radialkompressoren, 2. Auflage, Springer Verlag, Berlin, 1980

[24] Elder, R.L.; Macdougal, I. (1983): Simulation of Centrifugal Compressor Transient Performance for Process Plant Applications, Journal of Engineering for Power, 1983

[25] Ferguson T.B. (1963): The centrifugal stage, Butterworths, London, 1963

[26] Ferrari M. (2005); Magistri, L.: Control system for Solid Oxide Fuel Cell Hybrid Systems, ASME Turbo Expo, GT-2005-68102, Reno-Tahoe, Nevada, USA, 2005

[27] Fister, W. (1984): Fluidenergiemaschinen, Physikalische Voraussetzungen, Kenngrößen, Elementarstufen der Strömungs- und Verdrängermaschinen, Springer Verlag, Berlin, 1984

[28] Freeh, J. (2005): Off-design performance analysis of solid-oxide fuel cell / gas turbine hybrid for auxiliary aerospace power, FUELCELL2005-74099, Ypsilanti, Michigan, 2005

[29] Friend, M.G. (2003); Daggett, D.: Fuel Cell Demonstrator Airplane, AIAA 2003-2868, AIAA/ICAS International Air and Space Symposium and Exposition: The Next 100 Y, Dayton, Ohio, 2003

[30] Fink, D.A. (1992); Cumpsty, N.A.; Greitzer, E.M.: Surge Dynamics in a Free-spool Centrifugal Compressor System, Journal of Turbomachinery, April 192, Vol. 114 pp.321,33

[31] Föllinger, O. (1990): Regelungstechnik, Hüthig Buch Verlag Heidelberg, 1990

[32] Gravdahl, J.T. (1999): Centrifugal Compressor Surge and Speed Control, IEEE Transaction on control systems technology, 1999

[33] Gravdahl, J.T. (2000): Active Surge Control of Centrifugal Compressors using Drive Torque, 2000

[34] Greitzer, E.M. (1976): Surge and Rotating Stall in Axial Flow Compressors, Transaction of the ASME, 1976

[35] Groth, K (1985): Entscheidungshilfe zum Thema Schraubenkompressoren, Fachzeitschrift Pumpen, Vakuumpumpen, Kompressoren, 1985

[36] Hagelstein, D. (2001): Experimentelle Untersuchungen an einer Radialverdichterstufe mit verschiedenen Vorleitgittern variabler Geometrie, doctoral thesis, Hannover, 2001

[37] Heisler, O. (2005); Bahnen, R.: Intelligent Air Supply, Pumps and Compressors 2005 with Compressed Air and Vacuum Technology, 2005

[38] Hildebrandt, A. (2006): Modelling and Numerical Analysis of the Centrifugal Compressor and its Operation in the Pressurised SOFC GT Process, doctoral thesis, Lund Institute of Technology, Lund University, Sweden, 2004

[39] Hörl, F. (1987): Systemtheoretische Methode zur dynamischen Zustandsüberwachung von Gasturbinen, doctoral thesis, Universität München, München, 1987

[40] Japikse, D. (1996): Centrifugal Compressor Design and Performance, Concepts ETI Inc., 1996

[41] Kim, J.H.; Kim, T.S. (2001): Dynamic Simulation of Full Start-up Procedure of Heavy Gas Turbines, ASME Turbo Expo, 2001-GT-0017, New Orleans, Louisiana, USA, 2001

[42] Kuhlberg, J.F.(1969); Sheppard, D.E.: The Dynamic Simulation of Turbine Engine Compressors, AIAA Paper 5th Propulsion Joint Specialist Conference, 69-486, U.S. Air Force Academy, Colorado, USA, 1969

[43] Kulp, G. (2001): A Comparison of Two Air Compressors for PEM Fuel Cell Systems master thesis, Virginia Polytechnic Institute and State University, 2001

[44] Lang, O. (2004): Verdichter und Expander für mobile Brennstoffzellensysteme, MTZ7-8/2004 and Informationstagung Motoren, Heft R515, Frankfurt, 2004

[45] Lattner, J. R. (2004), Harold, M. P.: Comparison of conventional and membrane reactor fuel processors for hydrocarbon-based PEM fuel cell systems, International Journal of Hydrogen Energy 29 (2004) 393 – 417

[46] Lawson, L. (2003); Tucker, D.: Experimental Simulation of Fuel Cell Gas Turbine Hybrid Systems, GT2003-38460, ASME Turbo Expo, 2003

[47] Lenz, B.; Full, J.; Siewek, C.: Reforming of Jet fuel for Fuel Cell APUs in Commercial Aircraft, Fraunhofer Institute for Solar Energy Systems

[48] Lenz, B. (2005); Aicher, T.: Catalytic autothermal reforming of Jet fuel, Journal of Power Sources 149 (2005) 44–52

[49] Lunze, J. (2006): Regelungstechnik 1 & 2, 4. Auflage, Springer Verlag, Berlin, Heidelberg, 2006

[50] Ludyk, G. (2001): Theoretische Regelungstechnik 1 & 2, Springer Verlag, Berlin, Heidelberg, 2001

[51] Matlab Manual, Release 14, Service Pack 1

[52] McCotheon, A.R.S. (1978): Aerodynamic design and development of a high pressure ratio turbocharger compressor, IME paper C73/7

[53] Neymayer, F. (2001): Time-resolved simulation of the Operational Behaviour of a Test Turbine Facility, 4th European Conference on Turbomachinery, Firenze, Italy, 2001

[54] Neubrand, W. (1999): Modellbildung und Simulation von Elektromembranverfahren, doctoral thesis, Universität Stuttgart, 1999

[55] Pampreen, R.C, (1993): Compressor Surge and Stall, Concepts ETI, Norwich, Vermont, USA, 1993

[56] Pukrushpan J. T. (2002), Stefanopoulou, A.G.: Modeling and Control for PEM Fuel Cell Stack System, Proceedings for the American Control Conference, Anchorage, AK May 8-10, 2002

[57] Pischinger, S. (2001); Schönfelder, C.: Integrated Air Supply and Humidification Concepts for Fuel Cell Systems, 2001-01-0233, Society of Automotive Engineers, 2001

[58] Pischinger, S. (2002); Schönfelder, C.: Development of Fuel Cell System Air Management utilising HIL Tools, 2002-01-0409, Society of Automotive Engineers, 2002

[59] Pischinger, S. (2003); Schönfelder, C.: Verdichter-/Expandereinheiten für mobile Brennstoffzellensysteme mit hohem Systemwirkungsgrad, final report for

the AiF, project no. 067590 (AiF-Nr. 12614N/1), Informationstagung Motoren, Frankfurt, 2003

[60] Pischinger, S. (2004); Severin C.: State Machine-Based Control Strategy for a Gasoline Fueled PEMFC APU System, SAE Paper 2004-01-1475, 2004

[61] Pratt, J. (2003); Brouwer, J.; Samuelsen, G.: Experimental Evaluation and Computer Simulation of an Air-breathing PEM Fuel Cell at Aircraft Flight Altitudes, Proceedings of the 2003 Fuel Cell Seminar, pp. 114ff, Miami, 2003

[62] Rachner, M. (1998): Die Stoffeigenschaften von Kerosin Jet A-1, Köln, Deutsches Zentrum für Luft- und Raumfahrt, 1998

[63] Rake, H. (1998): Regelungstechnik A, Umdruck zur Vorlesung am Institut für Regelungstechnik an der RWTH Aachen, 1998

[64] Rautenberg, M. (1984): Radialverdichter, Vorlesungsskript, Universität Hannover, Germany, 1984

[65] Riekmann, C. (1997): Lösung des Problems der Diffusion und Reaktion in dreidimensionalen Porennetzwerken für allgemeine Kinetiken, doctoral thesis, Technische Universität Hamburg- Harburg, 1997

[66] Ritchey, I. (1997); Stephenson, D.: Parametric study of fuel cell and gas turbine combined cycle performance, 97-GT-340, ASME Turbo Expo, 1997

[67] Rodatz, P. (2003): Dynamics of the polymer electrolyte fuel cell experiments and model-based analysis, doctoral thesis, ETH Nr. 15320, ETH Zürich, 2003

[68] Rodatz, P. (2005): Air supply system of a PEMFC stack dynamic model, Fuel Cells 2005, 5, No. 1

[69] Rodatz, P. (2003): Optimizing air supply control of a PEM fuel cell system, IEEE, Proceedings of the American Control Conference Denver, Colorado June 4-6, 2003

[70] Rodgers, C. (1964): Typical performance characteristics of gas turbine radial compressors. Trans ASME Journal of Engineering for Power 86, p. 161, 1964

[71] Rothammer, W. (2004): Power Optimized Aircraft, H2Expo - International Conference Fuel Cell Systems for Transportation, Hamburg, 2003

[72] Rothammer, W. (2005): Airbus Fuel Cell System Approach, H2Expo – International Conference Fuel Cell Systems for Transportation, Hamburg, 2005

[73] Shaaban, S. (2004): Experimental investigation and extended simulation of turbocharger non-adiabatic performance, doctoral thesis, Hannover, 2004

[74] Schultz, J.M. (1962): The Polytropic Analysis of Centrifugal Compressors, Journal of Engineering for Power,1962

[75] Siebke, A. (2003): Modellierung und numerische Simulation der Direktmethanol-Brennstoffzelle. doctoral thesis, Universität Stuttgart, 2003

[76] Stanitz, J.D. (1952): Some theoretical aerodynamic investigations of impellers in radial and mixed flow centrifugal compressors. Transactions of the ASME, Vol. 74, pp. 473-479, 1952

[77] Stiller C. (2005); Thorud, B.: Safe Dynamic Operation of a Simple SOFC/GT Hybrid System, ASME Turbo Expo, GT2005-68481, Reno-Tahoe, Nevada, USA, 2005

[78] Traupel W. (1962): Die Theorie der Strömung durch Radialmaschinen, Verlag G. Braun, Karlsruhe, 1962

[79] Thirumalai, D. (2000): Steady-state operation of a compressor for a proton exchange membrane fuel cell system Journal of Applied Electrochemistry, 2000

[80] Varigonda, S. (2003); Pukrushpan, J.T.: Challenges in fuel cell power plant control: The role of system level dynamic models, Proceedings of the AIChE Spring Meeting, 2003

[81] VDI Wärmeatlas, 10 Auflage, Springer Verlag, Berlin, 2006

[82] Wiartalla, A. (2000); Pischinger, S.: Compressor Expander Units for Fuel Cell Systems, 2000-01-0380, Society of Automotive Engineers, 2000

[83] Whitfield, A (1990): Design of radial turbomachines, John Wiley & Sons, 1990

[84] Wiesner, F.J. (1967): A review of slip factors for centrifugal impellers. ASME Journal of Engineering for Power, Vol. 89, p. 558-572, 1967

[85] Wöhr, M. (1999): Instationäres, thermodynamisches Verhalten der Polymermembran-Brennstoffzelle. doctoral thesis, Universität Stuttgart, 1999

List of Figures

Fig. 1 Ambient conditions in the stratosphere and troposphere vs. altitude 8
Fig. 2 Operating range of a commercial APU 8
Fig. 3 Flight envelope parameters and boundary conditions 9
Fig. 4 Schematic flow sheet of the PEM-FC 10
Fig. 5 Concept A for the air supply system 14
Fig. 6 Concept B for the air supply system with two turbochargers 14
Fig. 7 Concept C for the air supply system with electric drive for reformer compressor 14
Fig. 8 Performance overview of the total air compressor 16
Fig. 9 Performance overview of the turbine 16
Fig. 10 Energy balance of the air supply system at TIT = 530K 16
Fig. 11 Energy balance of the air supply system at TIT = 1250K 17
Fig. 12 Important temperature values of the air supply system 18
Fig. 13 Constant cathode pressure and mass flow operation in the reduced compressor map 20
Fig. 14 Constant cathode pressure and mass flow operation in the rearranged compress. map 20
Fig. 15 Radial impeller geometries and velocity diagrams 26
Fig. 16 Velocity diagrams at the inlet and outlet of the impeller 26
Fig. 17 Mach number diagrams at the inlet and outlet of the impeller 27
Fig. 18 Design procedure for the single-stage radial compressor 34
Fig. 19 Design procedure for the two-stage radial compressor 35
Fig. 20 Isentropic efficiency and diffusion ratio as a function of the radius ratio 37
Fig. 21 Relative inlet Mach number and power coefficient as a function of the radius ratio 37
Fig. 22 Design plane for maximum efficiencies as a function of the impeller outlet flow angle and the impeller outlet blade angle 37
Fig. 23 4-D matrix visualisation of the optimum efficiency for the single-stage compressor design 38
Fig. 24 Compressor characteristics for different design strategies 39
Fig. 25 Compressor characteristics for different design strategies 39
Fig. 26 Optimum pressure ratio split fort the two-stage compression 40
Fig. 27 Comparison between the single-stage and the two-stage compressor maps 41
Fig. 28 Compressor model according to Greitzer, E.M. (1976) 47
Fig. 29 Downstream pressure modelling strategy for the distributed device volumes 50
Fig. 30 Air supply system parameters as a function of the operating altitude 55
Fig. 31 Operating line in the compressor map as a function of the operating altitude 55
Fig. 32 Power management of the turbocharger 56
Fig. 33 Simple cathode pressure function 57
Fig. 34 Compressor map operating lines for the simple cathode pressure function 58
Fig. 35 TC drive power for the simple cathode pressure function 58
Fig. 36 Advanced cathode pressure function 59
Fig. 37 Compressor map operating lines for the advanced cathode pressure function 60
Fig. 38 TC drive power for the advanced cathode pressure function 60
Fig. 39 TC drive power for the simple pressure function and a varying cathode pressure loss 61
Fig. 40 TC drive power for the advanced pres. function and a varying cathode pressure loss 61
Fig. 41 TC drive power for the single-stage and two-stage compressor 62
Fig. 42 TC drive power for an efficiency improved turbine design 63
Fig. 43 TC drive power with and without additional co-firing 64
Fig. 44 System parameters during co-firing as function of the operating altitude 65

Fig. 45 3D map of the TC drive power as a function of the operating altitude and the mass flow 66
Fig. 46 3D map of the inlet guide vane position as a function of the operating altitude and the mass flow 66
Fig. 47 Normalised cathode mass flow operating range for the base case 67
Fig. 48 Cathode mass flow operating range as a function of the cathode pressure 68
Fig. 49 Cathode mass flow operating range as a function of the cathode pressure loss 69
Fig. 50 Cathode mass flow operating range in dependency of the turbomachinery design 69
Fig. 51 Cathode mass flow operating range in dependency of co-firing 70
Fig. 52 Step response analysis for a cathode mass flow and pressure increase 73
Fig. 53 System response for a cathode mass flow and pressure increase 75
Fig. 54 Cathode mass flow response time of the turbocharger section 75
Fig. 55 Cathode pressure response time of the turbocharger section 75
Fig. 56 RGA for the turbocharger section as a function of the operating altitude 78
Fig. 57 Frequency dependent RGA of the turbocharger section at 6000m 78
Fig. 58 Controller architecture including a simplified decoupler 79
Fig. 59 System response for the independent and decoupled SISO-control during a cathode mass flow and pressure increase 81
Fig. 60 Compressor mass flow and outlet pressure response for a mass flow increase at 6000m 82
Fig. 61 IGV, valve position, and electric power demand during a mass flow increase at 6000m 82
Fig. 62 Compressor mass flow and outlet pressure response for a mass flow increase at different operating altitudes 83
Fig. 63 Comparison of the TC section response for the dynamically decoupled SISO and the LQG control 85
Fig. 64 Comparison of the reformer compres. response for the dynamically decoupled SISO and the LQG control 85
Fig. 65 Comparison of the TC section response for the decoupled SISO and the LQG control 86
Fig. 66 Comparison of the control action for the TC section for the decoupled SISO and the LQG control 86
Fig. 67 Comparison of the reformer compressor response for the decoupled SISO and LQG control 86
Fig. 68 Comparison of the control action for the reformer compressor for the decoupled SISO and the LQG control 86
Fig. 69 State-space controller including a LQG regulator 87
Fig. 70 Comparison of the system response for the simple and the advanced PEM-FC model 88
Fig. 71 Comparison of the system response for the simple and the advanced PEM-FC model applying the decoupled controller 88
Fig. 72 System response as a function of the stack current increase 89
Fig. 73 System response as a function of the stack current and reformer performance increase 90
Fig. 74 System response during an extreme operating scenario with an adjusted turbine design, an advanced cathode pressure function, and the application of a decoupled controller 91
Fig. 75 Load demand, reduced mass flow and operating altitude for the reference flight envelope.... 92
Fig. 76 Load demand, reduced mass flow and operating altitude for the load change at cruising flight conditions 92
Fig. 77 System response during a typical on-board load scenario for the entire envelope 93

Fig. A-1 Performance overview of the reformer compressor 110
Fig. A-2 Compressor map extension by the use of inlet guide vanes 110

Fig. B-1 Influence of the outlet blade angle on the discharge Mach number 111
Fig. B-2 Influence of the discharge flow angle on the discharge Mach number 113
Fig. B-3 Absolute and meridional Mach number vs. non-dimensional speed 114
Fig. B-4 Absolute Mach number vs. non-dimensional speed as a function of the radius ratio 115

Fig. B-5 Diffusion ratio vs. the discharge blade angle β_{2b} as a function of the discharge blade angle and the radius ratio 116
Fig. B-6 Impeller outlet diameter and rotational speed as a function of the radius ratio 116
Fig. B-7 Rotor mass and moment of inertia a function of the radius ratio 117
Fig. B-8 Mean mass flow range a function of the radius ratio 117

Fig. D-1 TC drive power as a function of the operating altitude and mass flow 125
Fig. D-2 Inlet guide vane position as a function of the operating altitude and mass flow 125
Fig. D-3 TC drive power difference for an increased cathode pressure 126
Fig. D-4 TC drive power difference for an increased cathode pressure loss 126
Fig. D-5 TC drive power difference for a decreased turbine design inlet pressure 127
Fig. D-6 Air supply efficiency difference for the co-firing 127

Fig. E-1 Cathode mass flow response for a stack current increase of 20% and 30% 128
Fig. E-2 Compressor outlet pressure response for a stack current increase of 20% and 30% 128
Fig. E-3 Cathode mass flow response for a stack current and reformer output increase of 20% and 30% 129
Fig. E-4 Compressor outlet pressure response for a stack current and reformer output increase of 20% and 30% 129
Fig. E-5 Cathode mass flow response for a cathode air increase of 25% and 50% w/o the decoupled controller and a stack current and reformer output increase of 25% and 30% 130
Fig. E-6 Compressor outlet pressure response for a cathode air increase of 25% and 50% w/o the decoupled controller and a stack current and reformer output increase of 25% and 30% 130

List of Tables

Tab. 1 Design point assumptions for the air supply system components 15
Tab. 2 Extreme scenarios for on-ground operation 17
Tab. 3 Decision matrix for the concept choice 23
Tab. 4 Performance targets of the compression system 33
Tab. 5 Solution space for the single-stage optimisation 36
Tab. 6 Design point assumptions for the main components of the air supply system 74
Tab. A-1 Boundary conditions of the PEM-FC 109
Tab. B-1 Compressor design results for the single-stage and two-stage concept 118
Tab. B-2 Geometric design results for the single-stage and two-stage concept 118

Appendix

A Concept Analysis

Tab. A-1 Boundary conditions of the PEM-FC

parameter	value	unit
FC gross power	80	kW
$T_{cathode,\ inlet}$	70	°C
$T_{cathode,\ outlet}$	80	°C
$p_{cathode,inlet}$	1.33	bar
p_{ATR}	2.2	bar
p_{POX}	2.2	bar
$\dot{m}_{cathode\ inlet}$	0.15	kg/s
$\dot{m}_{ATR+POX,inlet}$	0.03	kg/s
$\dot{m}_{exhaust\ gas}$	0.21	kg/s
relative humidity $_{cathode,\ inlet}$	90	%
relative humidity $_{exhaust\ gas}$	100	%
κ_{air}	1.4	-
R_{air}	287.04	J/(kg K)
$\kappa_{exhaust\ gas}$	1.36	-
$R_{exhaust\ gas}$	312.00	J/(kg K)
$\Delta p_{humidifier}$	5000	Pa
$\Delta p_{cathode}$	25000	Pa
$\Delta p_{post\text{-}combustor}$	5000	Pa

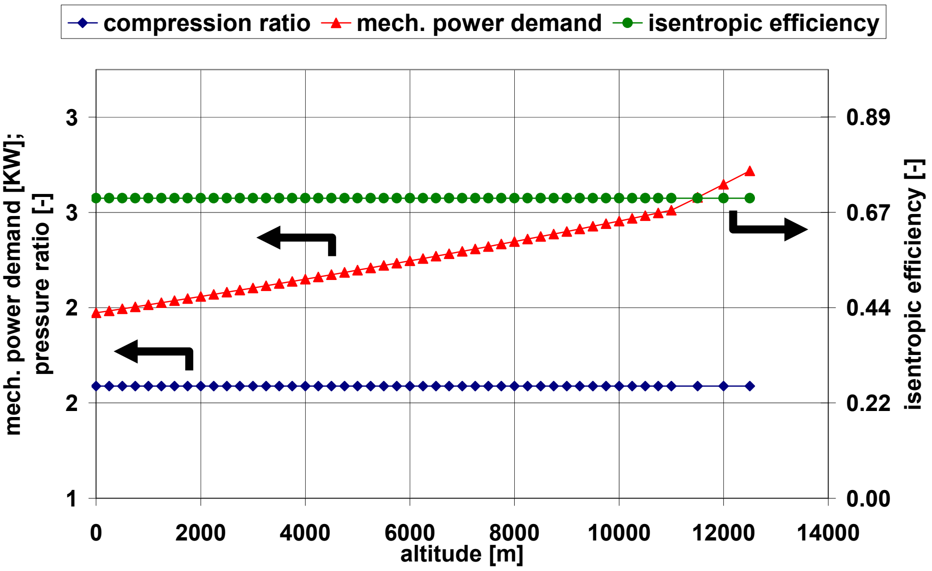

Fig. A-1 Performance overview of the reformer compressor

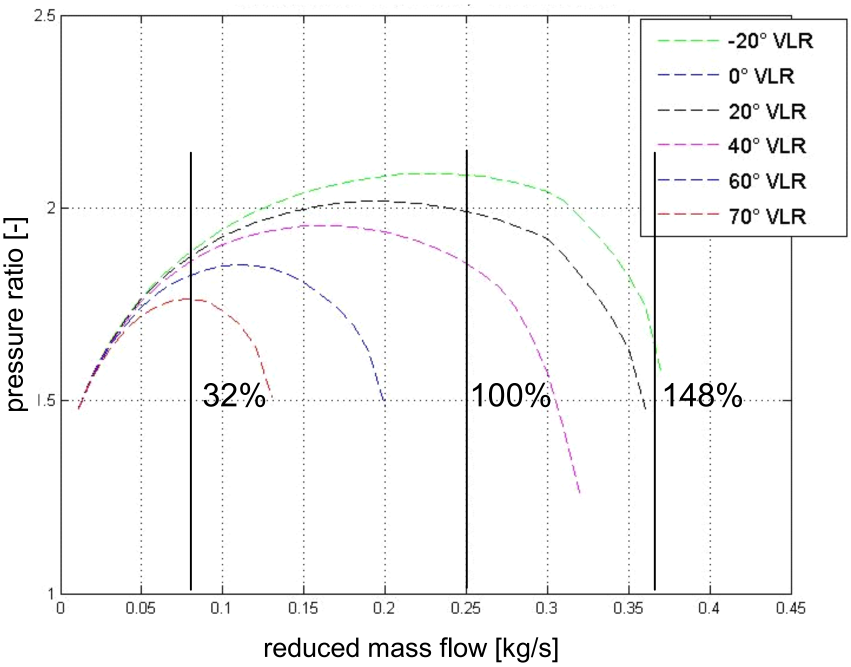

Fig. A-2 Compressor map extension by the use of inlet guide vanes

B Aerodynamic Design of an Radial Compressor Impeller

B.1 Influence of Outlet Blade Angle β_2 on Discharge Conditions

The increasing discharge number under increasing outlet blade angle and constant boundary conditions is shown in Fig. B-1 for different pressure ratios. The outlet blade angle affects only the work number according to Eq. 3-7, p.27. Decreasing the blade backward sweep leads to the reduction in discharge number for any given pressure ratio due to a reduced tangential absolute velocity at impeller exit.

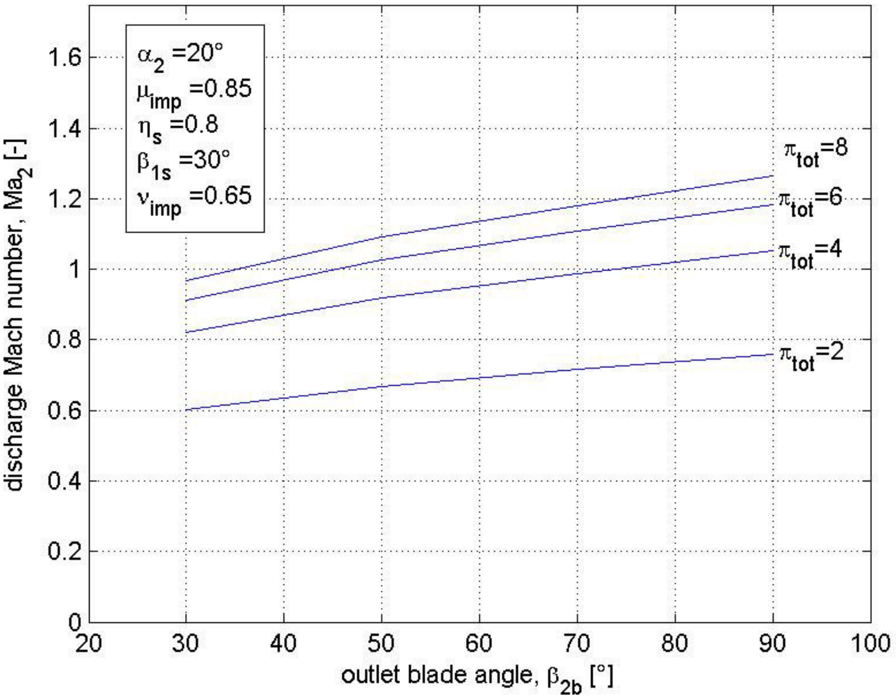

Fig. B-1 Influence of the outlet blade angle on the discharge Mach number

The choice of the appropriate outlet blade angle β_2 offers significant advantages as reported by Came, P.M., McKenzie, I.R.I. (1979). A reduction of the outlet blade angle leads to:

- A reduction of the impeller discharge absolute Mach number reducing the diffusion requirements of the following diffuser system and the risk of separation in case of a vaneless diffuser
- An increased negative gradient of the work input and pressure ratio to mass flow characteristic, which leads to a broader stable operating range

- An increased streamline curvature in the blade to blade plane, which leads to a reduced pressure gradient and thus to a reduction of secondary flows and associated losses

But following McCotheon, A.R.S. (1978), there is no optimum discharge blade angle from an aerodynamic point of view. The backward sweep is rather limited by mechanical and physical aspects which are:

- Increased tip speed, leading to increased disc and blade stresses
- The need to construct blades with non-radial fibres, leading to centrifugal bending stresses
- Increased impeller diameter, which leads to increased inertia and thus slower transient response being important in turbocharger applications

Today, from experimental experience and for most applications, the discharge blade angle may range from 40° to 70° in order to achieve acceptable range and efficiency.

B.2 Influence of Outlet Flow Angle α_2 on Discharge Conditions

Applying and rearranging Eq. 3-5, p.27, for the impeller outlet, Eq. 3-7 and Eq. 3-10, p.27, and the relation from the velocity diagram, the outlet Mach number can be also expressed as

$$\mathrm{Ma}_2 = \frac{\frac{\lambda \cdot \mathrm{Mu}}{\sin\alpha_2}}{1+(\kappa-1)\cdot\lambda\cdot\mathrm{Mu}^2\cdot\left(1-\frac{\lambda}{2\cdot\sin^2\alpha_2}\right)^{0.5}} . \qquad \text{Eq. B-1}$$

The meridional Mach number is then

$$\mathrm{Ma}_{2m} = \mathrm{Ma}_2 \cdot \sin\alpha_2 . \qquad \text{Eq. B-2}$$

Applying Eq. B-1 with varying discharge angles, the influence on the Mach number is depicted in Fig. B-2 for the pressure ratios of 2 and 8. For both pressure ratios, it can be recognised that at low discharge flow angles (α_2<30°) and high backward sweep (β_{2b}<50°), the discharge Mach number increases again but very moderately.

In order to decrease the loading of the subsequent diffuser section, the discharge angle should remain low. This strategy is limited, though, by the increasing friction losses due to the long flow pass through the diffuser. Additionally, Aungier, R. H. (2000) reports the risk of rotating stall, when the flow angle at diffuser inlet falls below 14 degree.

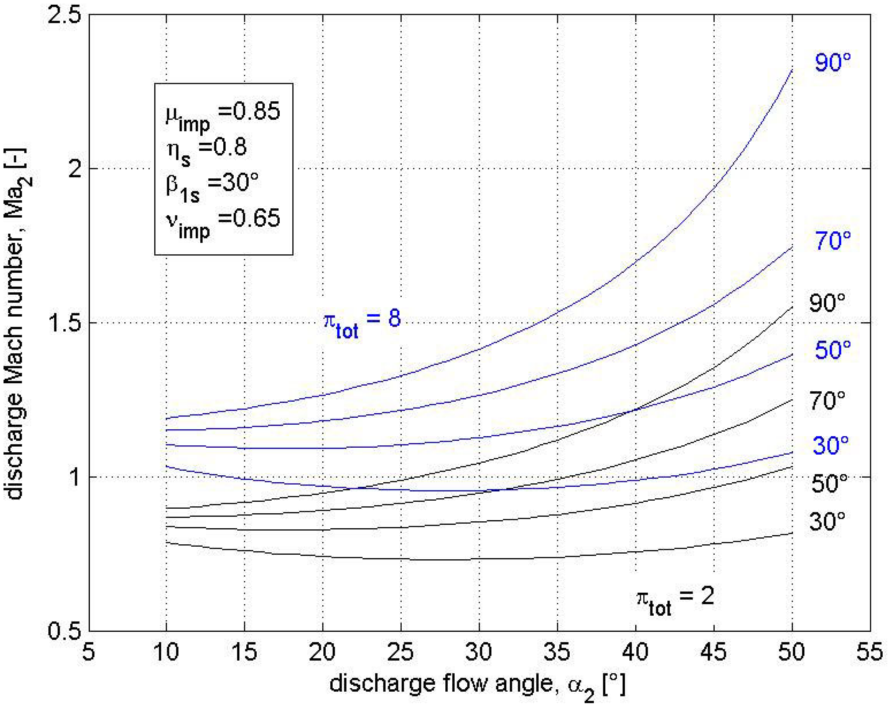

Fig. B-2 Influence of the discharge flow angle on the discharge Mach number

B.3 Interdependency between Discharge Conditions and Inlet Design

A strongly interdependent aerodynamic parameter during design is the relative inlet Mach number, which was stated to be a primary order task for the inducer design. The relative inlet Mach numbers are indicated by the vertical lines for constant Mach number at a given impeller speed (Fig. B-3), which demonstrates that inducer design cannot be considered separately from discharge design but is integrated into the design procedure. The relation can be expressed with

$$\mathrm{Ma}_{w1} = \frac{\dfrac{\mathrm{Mu}\cdot\nu}{\cos\beta_1}}{\left(1-(\kappa-1)\cdot(\mathrm{Mu}\cdot\nu)^2\cdot\tan^2\beta_1\right)^{0.5}} \qquad \text{Eq. B-3}$$

and is derived from Eq. 3-10, p.28, the velocity diagram and the expressions

$$\mathrm{Mu}_1 = \mathrm{Mu}\cdot\nu \qquad \text{Eq. B-4}$$

and

$$\frac{T_{1t}}{T_1} = \left(\frac{\mathrm{Ma}_{u1}}{\mathrm{Mu}_1}\right)^2 . \qquad \text{Eq. B-5}$$

B.4 Integral Illustration of Geometric and Aerodynamic Interdependencies

A good and compact illustration of the interdependency of geometric and aerodynamic parameters is possible when the absolute and meridional Mach number is plotted versus the non-dimensional impeller speed, as seen in Fig. B-3.

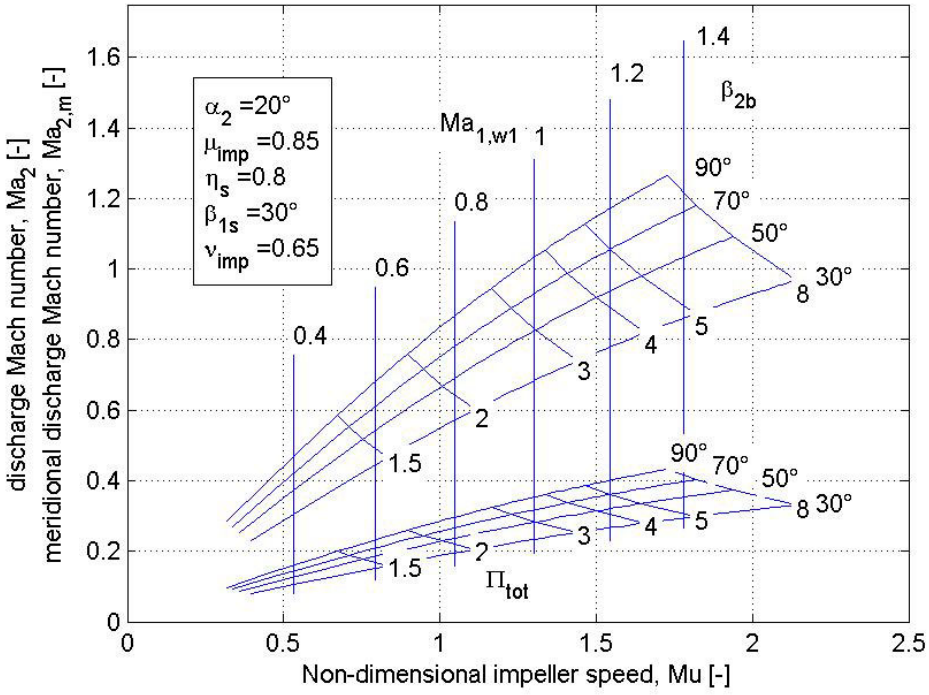

Fig. B-3 Absolute and meridional Mach number vs. non-dimensional speed

With a variation of the outlet angle α_2, it can be stated that a decreasing outlet angle is favourable for lowering the discharge Mach numbers. It has though a negative effect on the diffusion ratio as shown below. As stated in the precedent section, it can be recognised that the back sweep decreases the magnitude of discharge Mach number for any given pressure ratio up to the value of 8, which has to be paid though with a greater impeller speed. In the lower section of Fig. B-3, the meridional component of the discharge Mach number is depicted, which is of great importance for the evaluation of the diffuser loading and shock estimation at the leading edge of the vaneless diffuser. For the given set of boundary values, this number remains always lower than unity but may change significantly with different discharge angles and radius ratios, as will be demonstrated later.

A decreased outlet blade angle and thus increased impeller speed may interfere with the upper stated constraint of a maximum relative inlet Mach number of unity. But this parameter is also dependent on the hub ratio and the inlet blade angle. The outlet Mach number remains unchanged following according to Eq. B-1, p.112. The horizontal lines for constant relative inlet Mach numbers are shifted to lower impeller speeds when the inlet blade angle or the radius ratio is increased.

The influence of the radius ratio, however, is much more significant, which is shown in Fig. B-4 as a function of the relative inlet Mach number and the radius ratio. For high pressure ratios the relative inlet Mach number reaches quickly unity even at low radius ratios which has to be kept in mind for the following optimisation procedure.

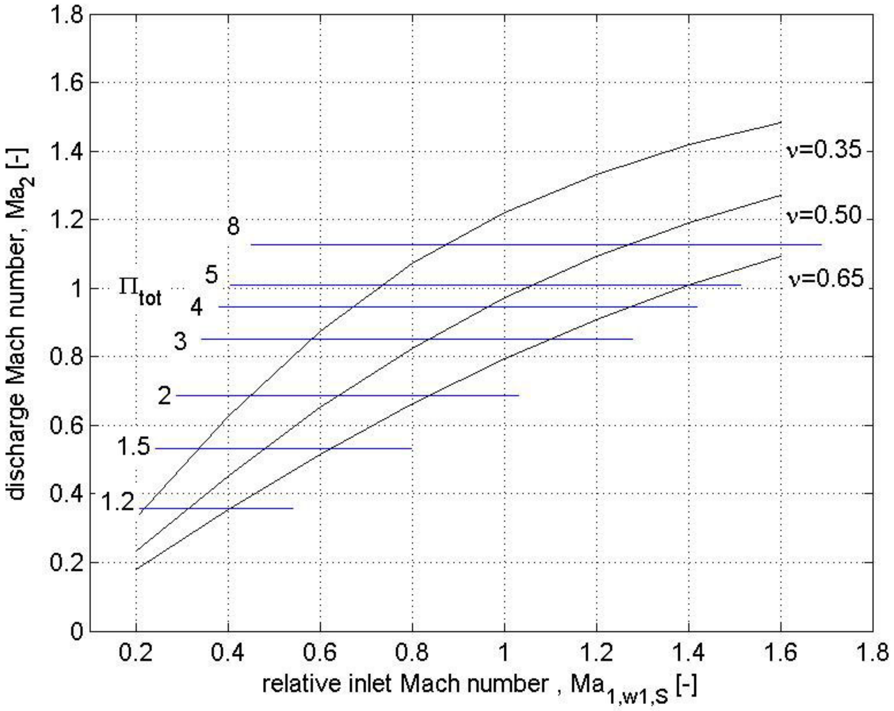

Fig. B-4 Absolute Mach number vs. non-dimensional speed as a function of the radius ratio

A last important relation is the diffusion ratio or the de Haller number, which refers to possible stability constraints in the impeller when a too high deceleration in the impeller passage might lead to boundary flow separation and backward flow causing significant losses or even initialising surge. This represents the operating limit of radial compressors at low mass flows. The diffusion ratio is defined by

$$\mathrm{deH} = \frac{w_2}{w_{1,S}} = \frac{\left(1 - 2 \cdot \lambda + \dfrac{\lambda^2}{\cos^2 \alpha_2}\right)^{0.5} \cdot \cos \beta_{1S}}{\nu} \quad \text{Eq. B-6}$$

Its dependency on geometric discharge parameters is depicted in Fig. B-5.

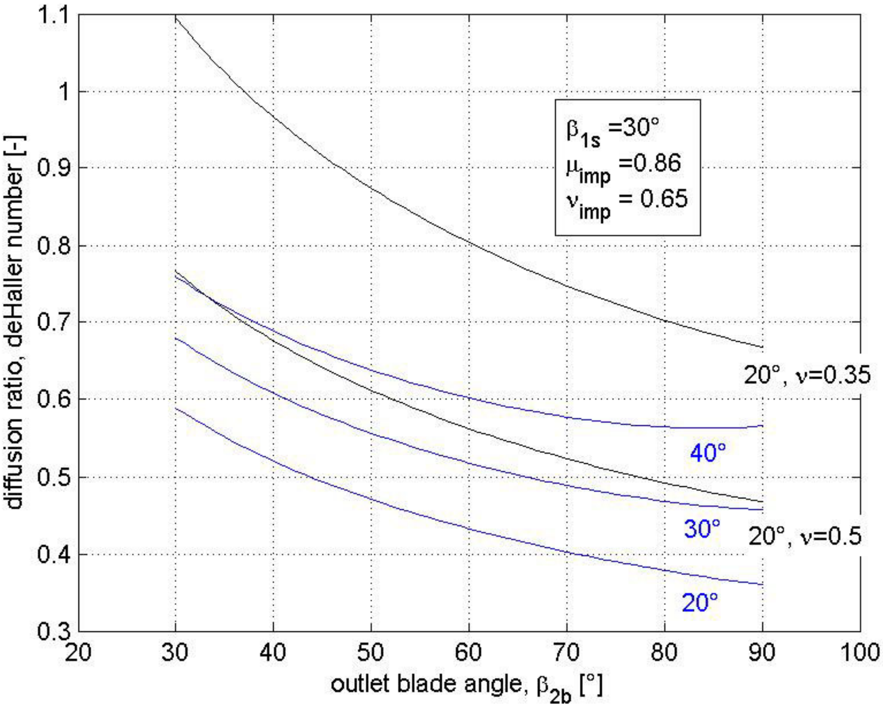

Fig. B-5 Diffusion ratio vs. the discharge blade angle β_{2b} as a function of the discharge blade angle and the radius ratio

It can be stated that the diffusion ratio is decreasing with increasing discharge blade angle and radius ratio, while it has to be kept above 0.62

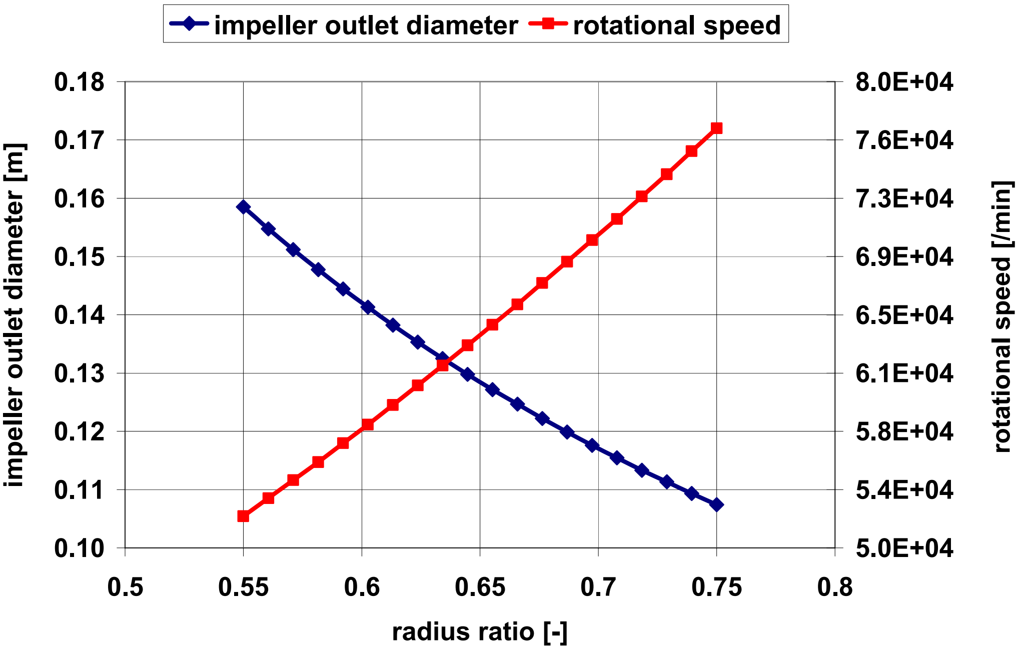

Fig. B-6 Impeller outlet diameter and rotational speed as a function of the radius ratio

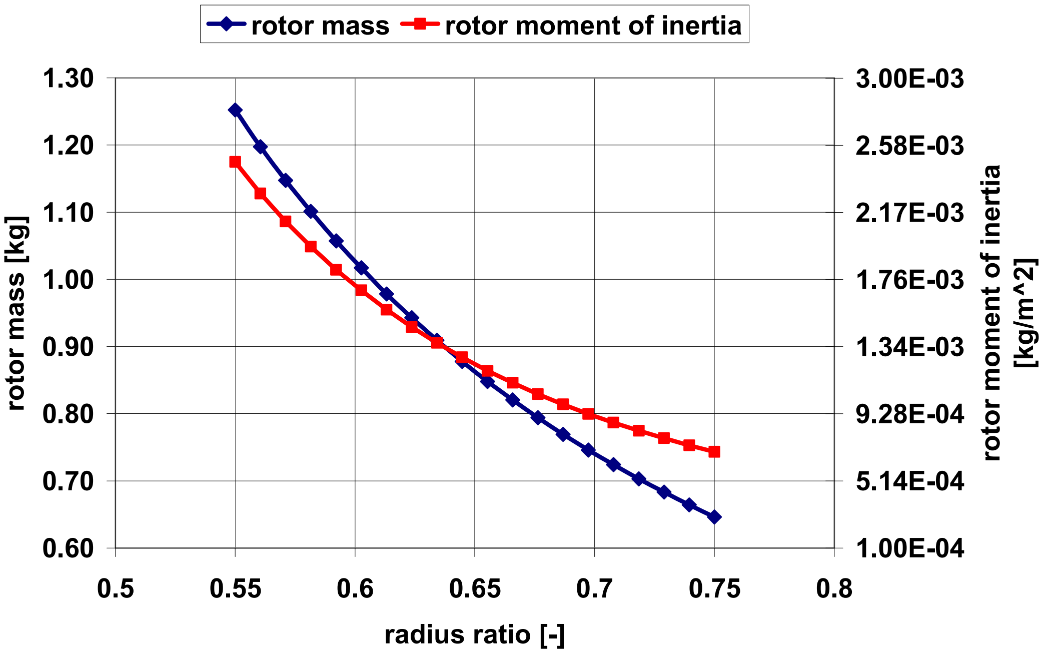

Fig. B-7 Rotor mass and moment of inertia a function of the radius ratio

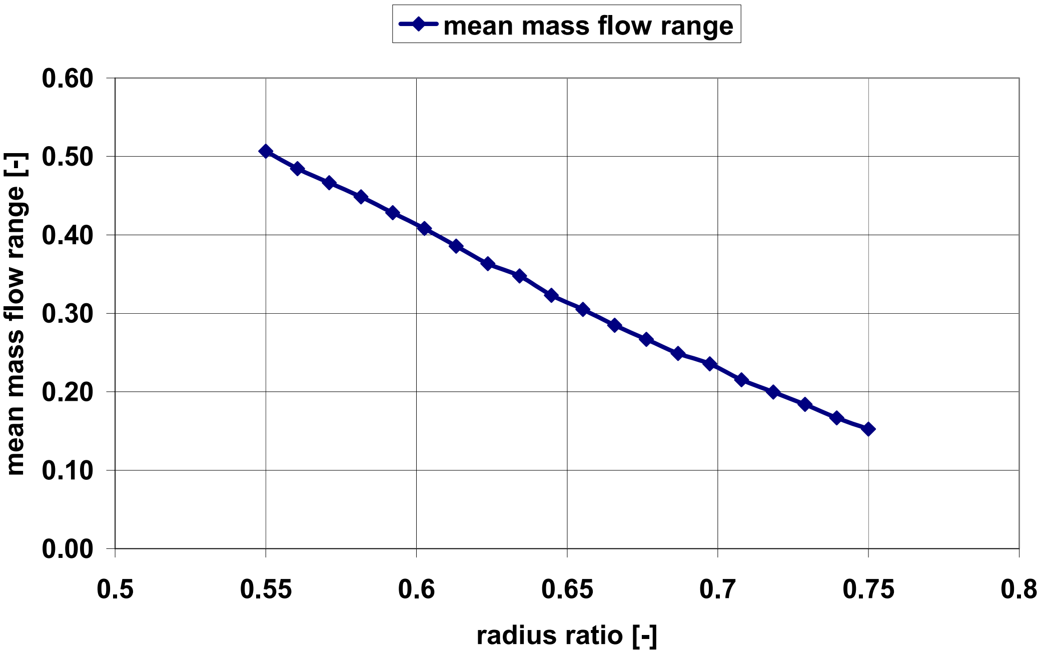

Fig. B-8 Mean mass flow range a function of the radius ratio

Tab. B-1 Compressor design results for the single-stage and two-stage concept

parameter	single-stage compression	two-stage compression			unit
		overall	1st. comp.	2nd comp.	
$\dot{m}_{red}$	0.886	0.886	-	-	kg/s
π_{tot}	7.5	7.5	2.75	2.14	-
η_{is}	0.675	0.743	0.769	0.784	-
deH	0.723	-	0.859	0.897	-
$Ma_{1w1,S}$	1.000	-	0.998	0.904	-
W_{nd}	0.284	-	0.269	0.086	-
m_{rotor}	1.541	-	0.694	0.895	kg
J_{rotor}	$3.523*10^{-3}$	-	$0.916*10^{-3}$	$1.57*10^{-3}$	kg m^2
range	0.235	0.497	-	-	-
mean range	0.549	0.547	-	-	-

Tab. B-2 Geometric design results for the single-stage and two-stage concept

parameter	single-stage compression	two-stage compression		unit
		1st. comp.	2nd comp.	
$\eta_{is,imp}$	0.843	0.877	0.918	-
n_{red}	61111	65272	-	1/s
Φ	0.037	0.1219	0.040	-
Ψ	1.101	0.963	1.013	-
ν	0.43	0.639	0.7	-
α_2	12	25	30	-
$\beta_{1,S}$	30.2	30.2	7.2	°
$\beta_{1,H}$	62.6	62.6	28.0	°
β_{2b}	51	55	55	°
$D_{1,S}$	0.083	0.083	0.105	m
D_2	0.193	0.130	0.150	m
D_3	0.289	0.195	0.226	m
z	12+12	8+8	7+7	-

C Turbomachinery Loss Modelling

C.1 Compressor Impeller

The incidence losses occur from a deviation between the flow angle and blade angle at inlet at off-design operation.

$$W_{inc,loss} = K_{inc} \cdot 0.5 \cdot w_1^2 \cdot \sin^2\left(abs\left(\beta_{1b} - \beta_{1,opt}\right)\right) \text{with } K_{inc} \approx 1 \qquad \text{Eq. C-1}$$

The optimum flow angle at inlet, $\beta_{1,opt}$, can be calculated from the continuity equation at design point operation (Whitfield, A (1990)).

Impeller friction losses are calculated based on the analogous pipe friction model.

$$W_{fri} = \frac{4 \cdot c_f \cdot L_{imp}}{D_{h,imp}} \cdot \frac{w_2^2 + w_1^2}{2} \qquad \text{Eq. C-2}$$

The impeller passage length L_{imp} is assumed to be the mean of two quarter circles representing the blade contour (Baines, N.C. (1998)). The impeller hydraulic parameter $D_{h,imp}$ represents the mean of the hydraulic parameters at the impeller inlet and outlet. The friction coefficient is based on available pipe friction losses with the impeller Reynolds number definition

$$Re_{imp} = \frac{0.5 \cdot \left(w_2 + w_1\right) \cdot D_{h,imp}}{\nu_{air}} . \qquad \text{Eq. C-3}$$

Diffusion losses are assumed to be proportional to the difference between the kinetic energy between the impeller inlet and outlet

$$W_{diff} = K_{diff} \cdot \frac{w_1^2 - w_2^2}{2} \text{ and } K_{diff} = 0.367 \cdot \sqrt{\frac{w_1}{w_2}} . \qquad \text{Eq. C-4}$$

Passage losses are assumed to be proportional to the mean kinetic energy within the impeller

$$W_{pass} = K_{pass} \cdot \frac{w_1^2 + w_2^2}{2} \text{ and } K_{pass} = \frac{9.327}{Re_{imp}^{0.9 \cdot \left(\frac{D_1}{D_2}\right)^{1.2}}} + 0.005 . \qquad \text{Eq. C-5}$$

Clearance losses are assumed to be proportional to the energy carried by the flow through the impeller clearance

$$W_{cl} = K_{cl} \cdot \frac{\dot{m}_{cl}}{\dot{m}} \cdot u_2 \cdot c_{2u} \text{ and } K_{cl} = 0.0524 \quad . \qquad \text{Eq. C-6}$$

The blade loading losses are assumed to be proportional to the square of the impeller blade loading taken from Aungier, R. H. (2000)

$$W_b = K_b \cdot \left(w_{suc} - w_{pre} \right)^2 \text{ and } K_b = 0.002 \qquad \text{Eq. C-7}$$

and

$$w_{suc} - w_{pre} = \frac{2 \cdot \pi \cdot D_2}{z \cdot L_{imp}} \cdot c_{2u} \quad . \qquad \text{Eq. C-8}$$

The correlation for the disk friction losses is taken from Daily, J.W.; Nece, R.E. (1960). The empirical coefficients are obtained from a minimisation procedure based on experimental data presented in Shaaban, S. (2004)

C.2 Compressor Diffuser

The equations applied for the diffuser are the conservation of mass

$$c_m \cdot (br) \cdot d\rho + \rho \cdot (br) \cdot dc_m + \rho \cdot c_m \cdot d(br) = 0 \qquad \text{Eq. C-9}$$

the conservation of mass

$$d(rc_u) = -\frac{c_f \cdot \rho \cdot c_u \cdot \sqrt{c_u^2 + c_m^2}}{\rho_2 \cdot c_{2m} \cdot b_2 \cdot r_2} \cdot r^2 dr \qquad \text{Eq. C-10}$$

and the conservation of energy

$$\frac{dp}{\rho} = -d\left(\frac{c_u^2 + c_m^2}{2} \right) - \frac{c_{dis} \cdot \rho \cdot \left(c_u^2 + c_m^2 \right)^{\frac{3}{2}}}{\rho_2 \cdot c_{2m} \cdot b_2 \cdot r_2} \cdot r\, dr \qquad \text{Eq. C-11}$$

with c_f and c_{dis} the friction and dissipation coefficients, respectively. Rearranging and assuming adiabatic flow, it can be written

$$\frac{d\rho}{\rho} = -\left(\frac{dc_m}{c_m} + \frac{d(br)}{br} \right) , \qquad \text{Eq. C-12}$$

$$\frac{dc_u}{c_u} = -\left(\frac{dr}{r} + \frac{c_f \cdot \rho \cdot \sqrt{c_u^2 + c_m^2}}{\rho_2 \cdot c_{2m} \cdot b_2 \cdot r_2} \cdot r\, dr \right), \qquad \text{Eq. C-13}$$

and

$$\frac{dc_m}{c_m} = \frac{\frac{\rho}{\kappa_{air} p} \cdot \left(c_u dc_u + \frac{\kappa_{air} \cdot c_{dis} \cdot \rho \cdot \left(c_u^2 + c_m^2 \right)^{\frac{3}{2}}}{\rho_2 \cdot c_m \cdot b_2 \cdot r_2} \right) - \frac{d(br)}{br}}{1 - \frac{c_m^2}{\frac{\kappa_{air} \cdot p}{\rho}}}, \qquad \text{Eq. C-14}$$

obtaining non-dimensional relations for the density, the meridional and circumferential velocity and thus defining fully the aerodynamic and thermodynamic condition at any positions within the diffuser. In order to obtain the conditions at the diffuser outlet, the diffuser is divided into a great number of radial segments, at each segment applying and solving equations Eq. C-12 to Eq. C-14. Finally, the diffuser loss coefficient can be defined

$$\xi_{Diff} = \frac{p_{2t} - p_{3t}}{0.5 \cdot \rho_2 \cdot c_2^2} \qquad \text{Eq. C-15}$$

or the more often referred diffuser pressure recovery coefficient

$$c_{p,Diff} = \frac{p_3 - p_2}{0.5 \cdot \rho_2 \cdot c_2^2}. \qquad \text{Eq. C-16}$$

C.3 Compressor Volute

Analogous to the diffuser characteristics, the volute loss coefficient is defined by

$$\xi_{vol} = \frac{p_{3t} - p_{5t}}{0.5 \cdot \rho_3 \cdot c_3^2} \qquad \text{Eq. C-17}$$

and volute pressure recovery coefficient

$$c_{p,vol} = \frac{p_5 - p_3}{0.5 \cdot \rho_3 \cdot c_3^2}. \qquad \text{Eq. C-18}$$

In the volute, friction, exit cone, diffusion losses and dissipation of meridional velocity are considered. The friction losses are calculated with equivalent pipe flow model

$$\xi_{\mathrm{fri,vol}} = \frac{4 \cdot c_f \cdot L_{\mathrm{vol,mean}}}{D_{h,4}} \cdot \frac{\rho_5}{\rho_3} \cdot \left(\frac{c_4}{c_3} \right)^2 . \qquad \text{Eq. C-19}$$

The mean volute length is assumed to be

$$L_{\mathrm{vol,mean}} = \pi \cdot \left(r_3 + r_{\mathrm{cone}} \right) . \qquad \text{Eq. C-20}$$

The mean volute Reynolds number is defined by

$$\mathrm{Re}_{\mathrm{vol,mean}} = \frac{0.5 \cdot \left(c_u + c_{u,\mathrm{vol,mean}} \right) \cdot D_{h,4}}{\nu_4} . \qquad \text{Eq. C-21}$$

where the mean circumferential velocity is

$$c_{u,\mathrm{vol,mean}} = \frac{r_3 \cdot c_{3u}}{0.5 \cdot \left(r_3 + r_{\mathrm{cone}} \right)} . \qquad \text{Eq. C-22}$$

The correlation for the exit cone losses is taken from Aungier, R. H. (2000) and modified in order to account for the density change along the volute to

$$\xi_{\mathrm{vol,cone}} = \frac{\rho_5}{\rho_3} \cdot \frac{\left(c_4 - c_5 \right)^2}{c_3^2} . \qquad \text{Eq. C-23}$$

The meridional flow at the volute inlet is directed into a vortex which is assumed by the authors Aungier, R. H. (2000) and Whitfield, A (1990)) to be completely dissipated along the volute channel. Japikse, D. (1996), on the other hand, reports that a part of the meridional velocity is recovered in the exit cone. Therefore the meridional losses are accounted with

$$\xi_{\mathrm{vol,m}} = K_{\mathrm{vol,m}} \cdot \left(\frac{c_{3m}}{c_3} \right)^2 \text{ and } K_{\mathrm{vol,m}} = 0.43 . \qquad \text{Eq. C-24}$$

The increased absolute velocity caused by the vortex is assumed to increase friction and exit cone losses, which is accounted by the correction factor

$$F_{\mathrm{vol}} = \frac{3.28}{\mathrm{Re}_{\mathrm{vol}}^{0.05}} \cdot \left(\frac{c_{3m}}{0.5 \cdot \left(c_{u,\mathrm{vol,mean}} + c_4 \right)} \right)^{0.04} . \qquad \text{Eq. C-25}$$

The volute diffusion losses are assumed to occur when the mean dynamic pressure is greater then the dynamic pressure is at the inlet of the exit cone, which are expressed by

$$\xi_{vol,diff} = K_{vol,diff} \cdot \left(\frac{\rho_3 \cdot c_{u,vol,mean}^2 - \rho_4 \cdot c_4^2}{\rho_3 \cdot c_3^2} \right) \text{and}\, K_{vol,diff} = 0.54 .$$ Eq. C-26

The overall volute loss coefficient can be formulated with

$$\xi_{vol} = \left(\xi_{vol,fri} + \xi_{vol,cone} \right) \cdot F_{vol} + \xi_{vol,m} + \xi_{vol,diff} .$$ Eq. C-27

The empirical coefficients are again obtained from a minimisation procedure based on experimental data (see Shaaban, S. (2004)).

C.4 Turbine

The turbine mass flow is modelled by an expansion through a nozzle with an effective total-to-static pressure ratio taking into account the centrifugal force on the turbine mass flow. The effective pressure ratio is reduced by the radial outward pressure caused by the rotating turbine channel. The effective pressure ratio is then

$$\pi_{6t8s,eff} = \frac{p_{6t} - 0.5 \cdot \rho_6 \cdot \left(r_{rot} \cdot \omega \right)^2}{p_8} .$$ Eq. C-28

For low design shaft speeds the influence of the centrifugal forces is neglected. The mass flow rate can be then expressed as

$$\dot{m}_t = c_{d,T} \cdot A_T \cdot \frac{p_{6t,eff}}{\sqrt{R_{exh} \cdot T_{6,t}}} \cdot \Phi_{T,eff} .$$ Eq. C-29

with the discharge coefficient, $c_{d,T}$, which is dependent on the inlet guide vane position and the Reynolds number. The coefficient is obtained from experimental results. The effective flow coefficient is calculated by

$$\Phi_{T,eff} = \sqrt{\frac{2 \cdot \kappa_{exh}}{\kappa_{exh} - 1} \cdot \left(\pi_{6t,6s}^{\left(\frac{-2}{\kappa_{exh}} \right)} - \pi_{6t,6s}^{\left(\frac{-(\kappa_{exh}+1)}{\kappa_{exh}} \right)} \right)}$$ Eq. C-30

for

$$1 \le \pi_{6t,6s,eff} < \left(\frac{\kappa_{exh} + 1}{2} \right)^{\left(\frac{\kappa_{exh}}{\kappa_{exh} - 1} \right)}$$ Eq. C-31

and for choked flow by

$$\Phi_{T,eff} = \sqrt{\frac{\kappa_{exh}}{2} \cdot \left(\frac{2}{\kappa_{exh} + 1} \right)^{\left(\frac{\kappa_{exh}+1}{\kappa_{exh}-1} \right)}} \qquad \text{Eq. C-32}$$

while

$$\pi_{6t,6s,eff} > \left(\frac{\kappa_{exh} + 1}{2} \right)^{\left(\frac{\kappa_{exh}}{\kappa_{exh}-1} \right)} . \qquad \text{Eq. C-33}$$

The calculation of the isentropic efficiency is based on the relative blade speed parameter

$$\left(\frac{u}{c_s} \right)_{rel} = \frac{\left(\frac{u}{c_s} \right)}{\left(\frac{u}{c_s} \right)_{\eta_{T,\max}}} \qquad \text{Eq. C-34}$$

with c_s, the spouting velocity

$$c_s = \sqrt{2 \cdot c_{p,exh} \cdot T_{6,t} \cdot \left(1 - \pi_{6t,8s}^{\left(\frac{-(\kappa_{exh}-1)}{\kappa_{exh}} \right)} \right)} . \qquad \text{Eq. C-35}$$

Based on the assumption that the relative isentropic turbine efficiency is symmetric around the best efficiency point of the turbine, turbine isentropic efficiency is calculated with

$$\eta_{is,T} = \eta_{is,T,\max} \cdot \left(a \left(\frac{u}{c_s} \right)_{rel} - b \left(\frac{u}{c_s} \right)_{rel}^{2} \right) , \qquad \text{Eq. C-36}$$

where the coefficients a and b as well as the best efficiency point are obtained from experimental data and are valid for a wide range of radial turbines found in turbochargers. The design velocity ratio is obtained from the turbine design procedure determining the maximum turbine efficiency from a correlation for attainable radial turbine efficiency which is similar to the Smith diagram for axial turbines.

D Steady-state System Analysis

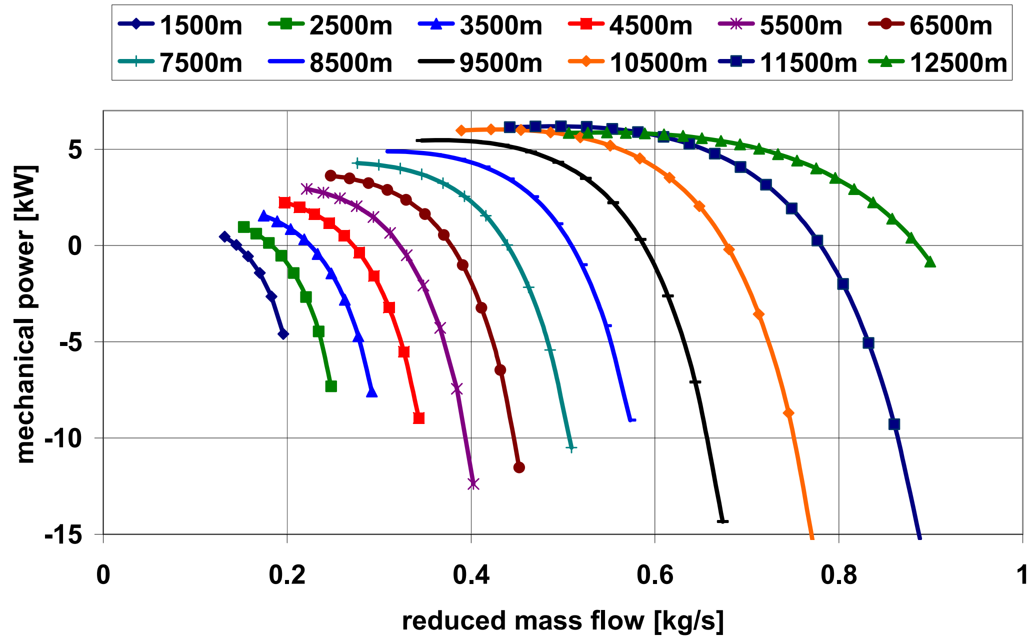

Fig. D-1 TC drive power as a function of the operating altitude and mass flow

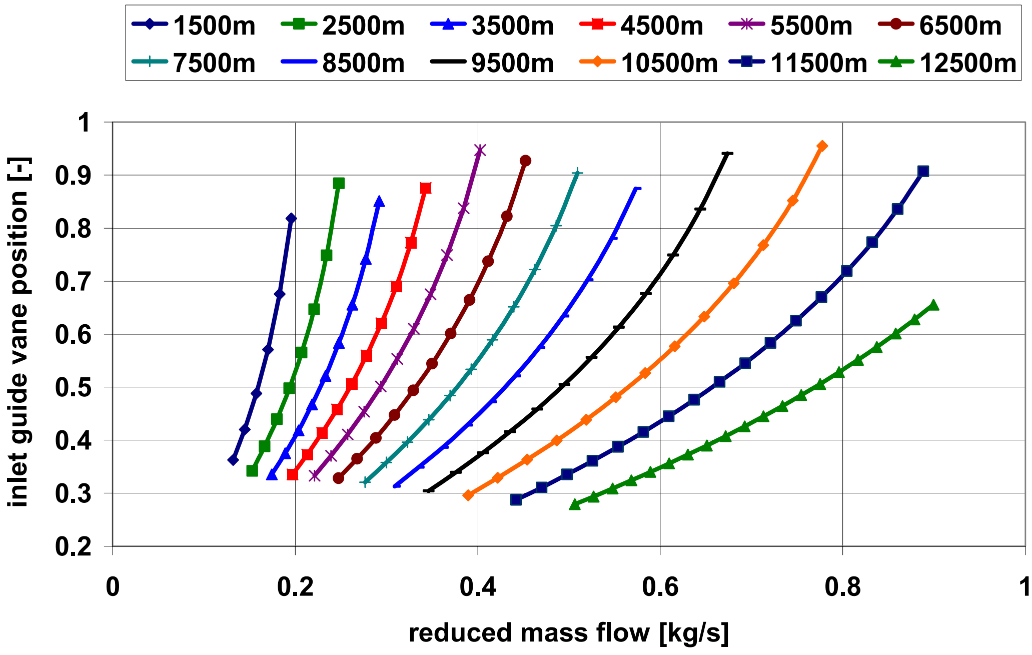

Fig. D-2 Inlet guide vane position as a function of the operating altitude and mass flow

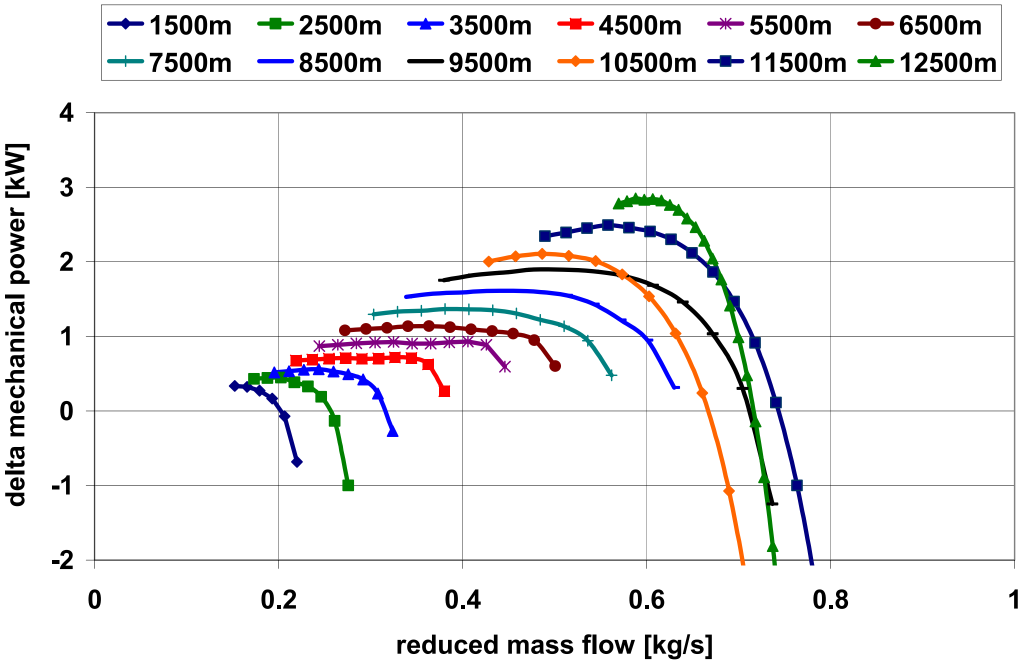

Fig. D-3 TC drive power difference for an increased cathode pressure

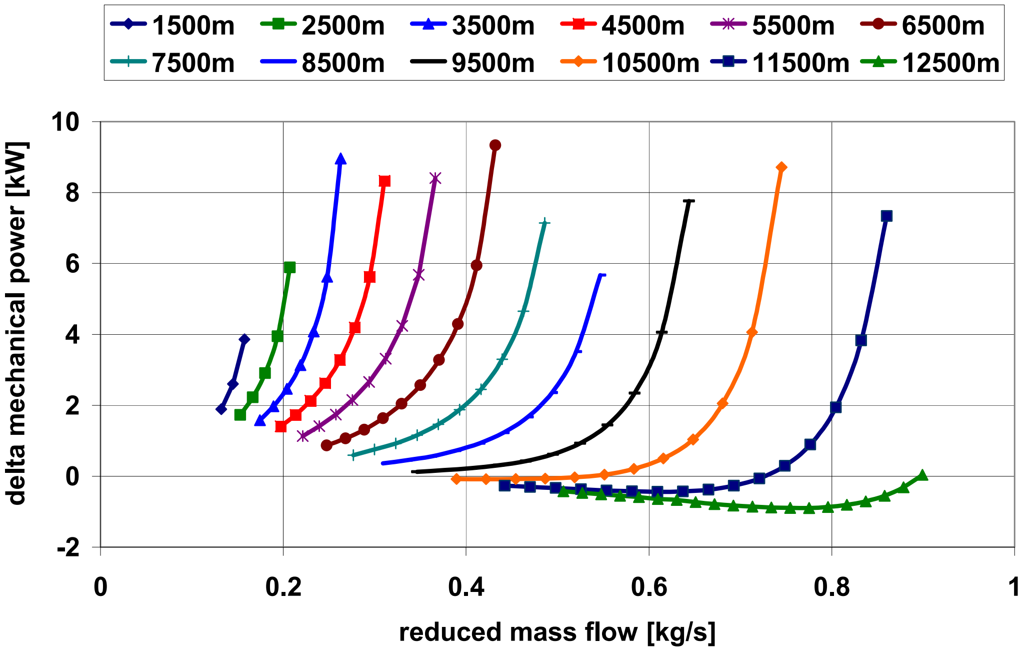

Fig. D-4 TC drive power difference for an increased cathode pressure loss

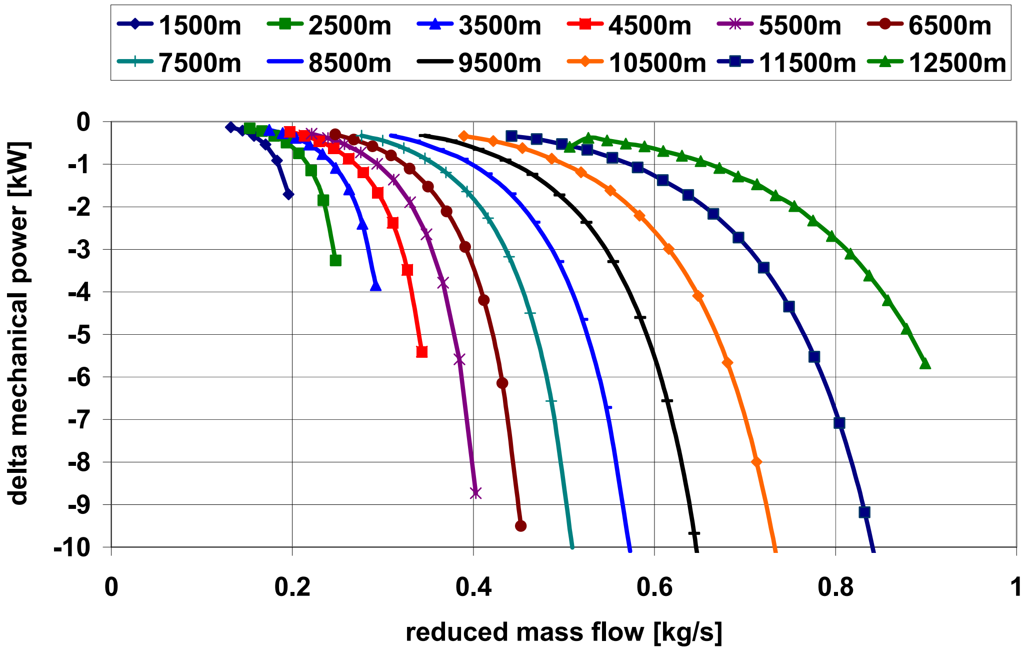

Fig. D-5 TC drive power difference for a decreased turbine design inlet pressure

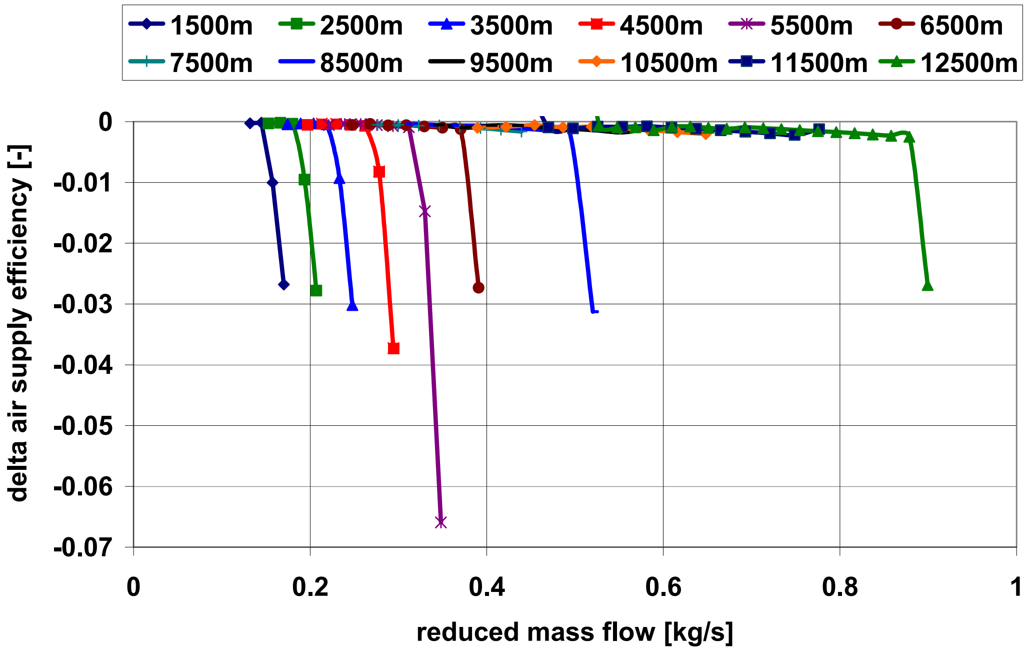

Fig. D-6 Air supply efficiency difference for the co-firing

E Transient System Analysis with an Advanced PEM-FC model

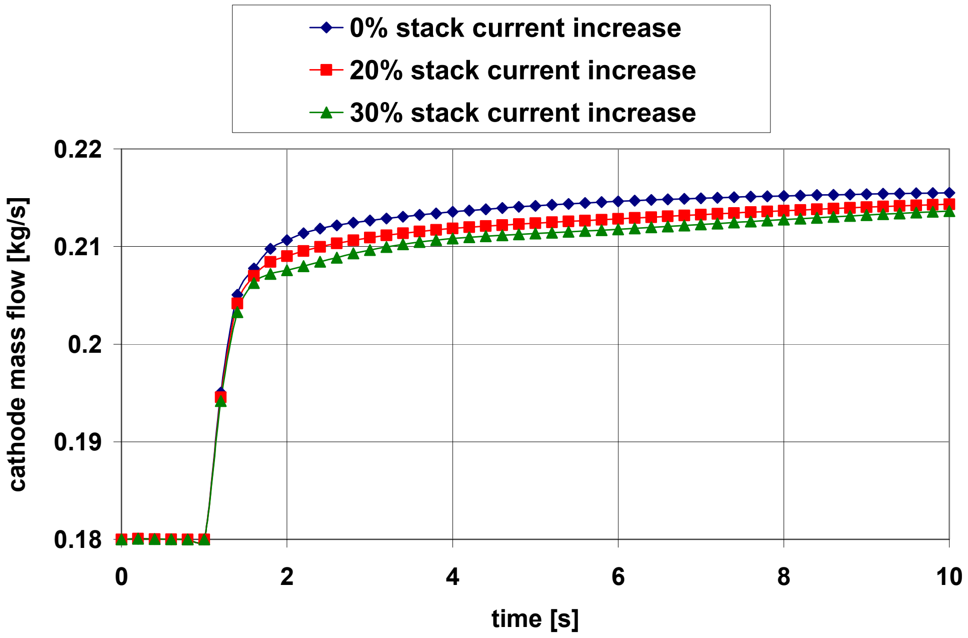

Fig. E-1 Cathode mass flow response for a stack current increase of 20% and 30%

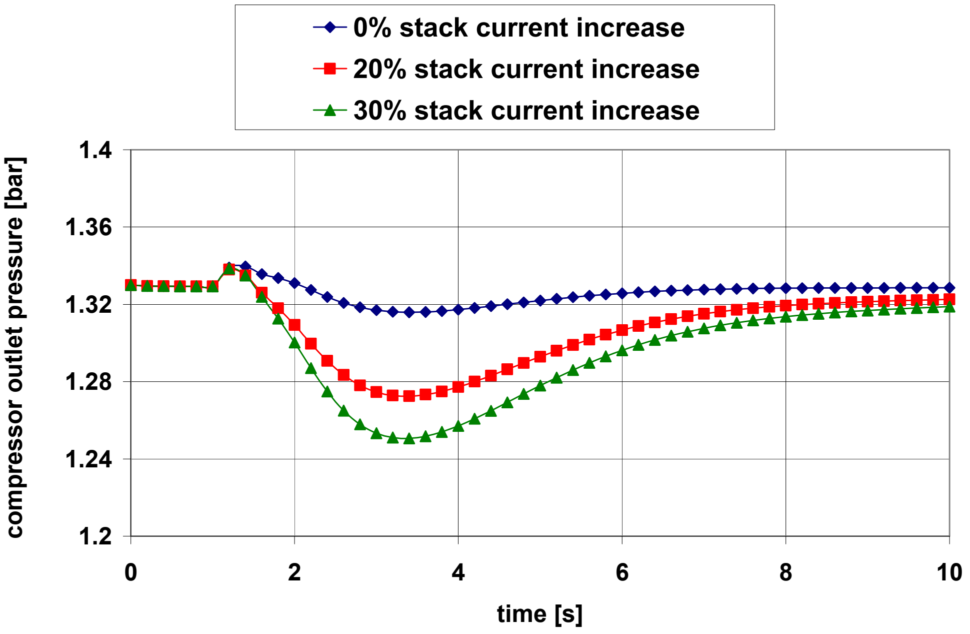

Fig. E-2 Compressor outlet pressure response for a stack current increase of 20% and 30%

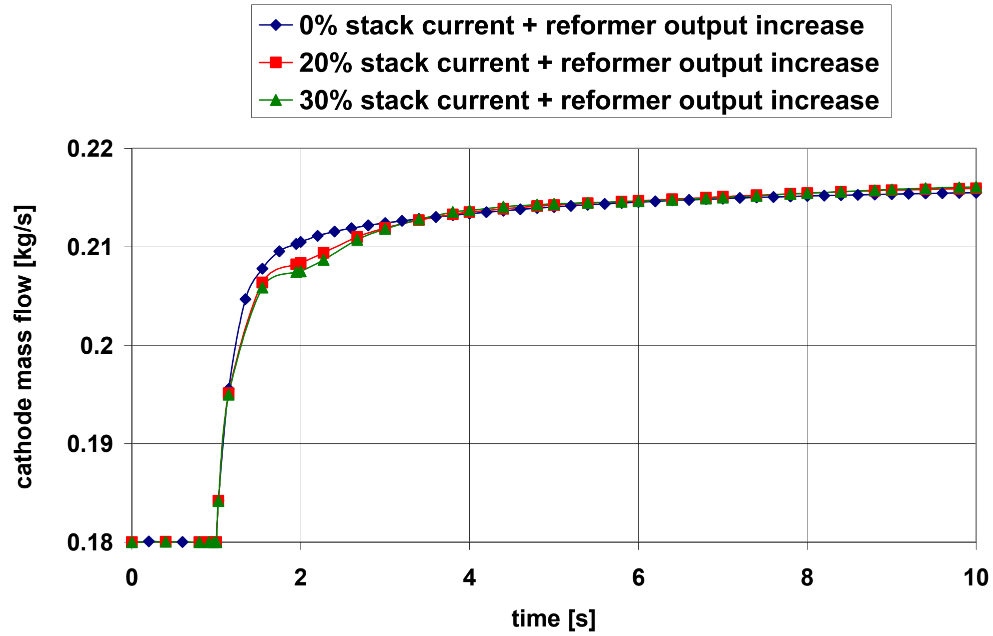

Fig. E-3 Cathode mass flow response for a stack current and reformer output increase of 20% and 30%

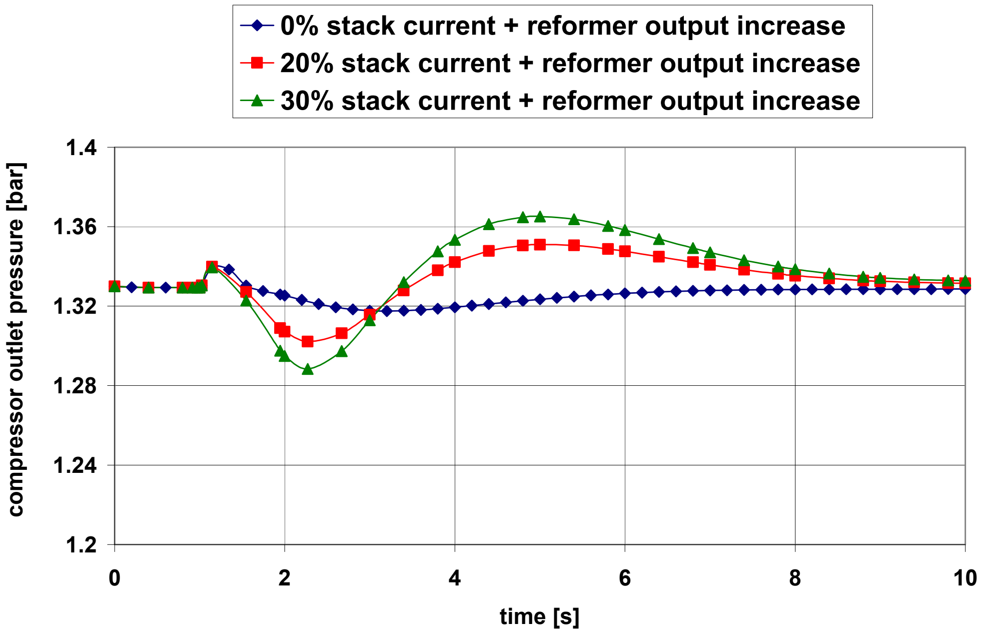

Fig. E-4 Compressor outlet pressure response for a stack current and reformer output increase of 20% and 30%

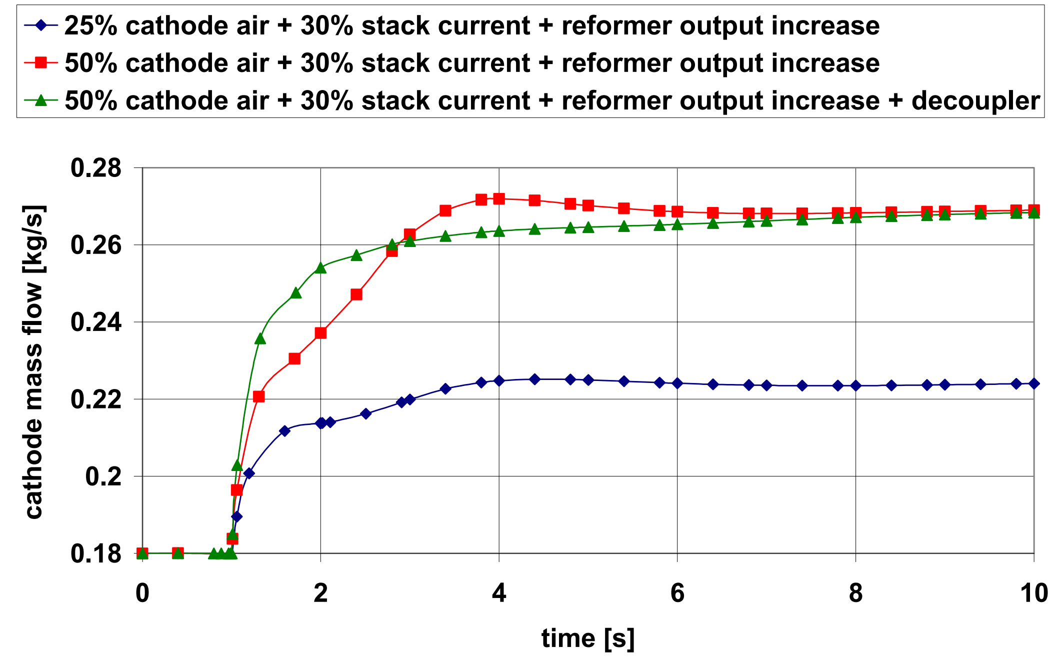

Fig. E-5 Cathode mass flow response for a cathode air increase of 25% and 50% w/o the decoupled controller and a stack current and reformer output increase of 25% and 30%

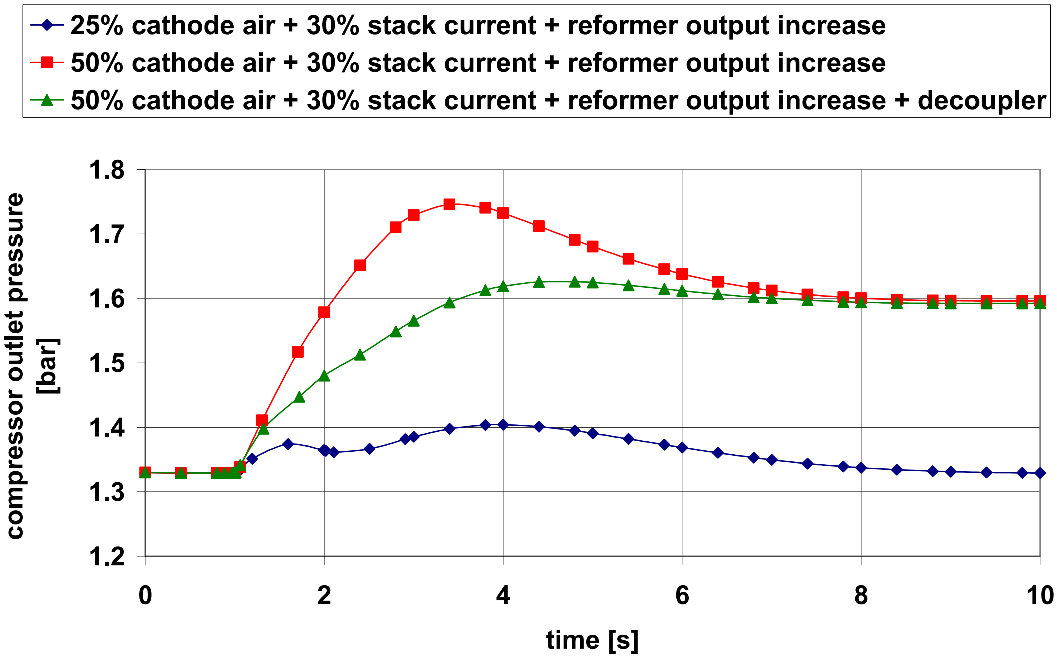

Fig. E-6 Compressor outlet pressure response for a cathode air increase of 25% and 50% w/o the decoupled controller and a stack current and reformer output increase of 25% and 30%

Curriculum Vitae

Name:	Lukas Barchewitz
Date of Birth:	9th of October, 1975

Education and academic degrees:

1995	Abitur, Städtisches Gymnasium Petershagen, Germany
2001	Diplom-Ingenieur, University of Hannover, Germany Main courses: turbomachinery and energy systems Thesis: Theoretische Untersuchung des instationären Betriebsverhaltens eines Kleingasturbinen-Hochtemperatur-brennstoffzellen-Systems

Stay abroad

08/1999 - 04/2000
Studies, Lunds tekniska högskola, Lund University, Sweden

10/2000 - 02/2001
Internship, Electricité de France, Paris, France

Work experience

08/2001– 06/2007
Research assistant, Institute for Turbomachinery and Fluid Dynamics, University of Hannover, Germany

07/2007
E.ON Kernkraft GmbH, Germany, mechanical department